A SIMULATION APPROACH TO THERMODYNAMICS IN INTERFACIAL PHENOMENA

A Dissertation

Presented to

the Faculty of the Department of Chemical and Biomolecular Engineering

University of Houston

In Partial Fulfillment

of the Requirements for the Degree

Doctor of Philosophy

in Chemical Engineering

by

Yogendra Narayan Pandey

May 2013

A SIMULATION APPROACH TO THERMODYNAMICS IN INTERFACIAL PHENOMENA

Yogendra Narayan Pandey

Approved:

Chair of the Committee
Manolis Doxastakis, Assistant Professor,
Chemical and Biomolecular Engineering

Committee Members:

Ramanan Krishnamoorti, Professor,
Chemical and Biomolecular Engineering

Gila Stein, Assistant Professor,
Chemical and Biomolecular Engineering

Haleh Ardebili, Assistant Professor,
Mechanical Engineering

Yashashree Kulkarni, Assistant Professor,
Mechanical Engineering

Suresh K. Khator, Associate Dean,
Cullen College of Engineering

Michael P. Harold,
Professor and Chairman,
Chemical and Biomolecular Engineering

Dedication

Tvadīyaṃ vastu Govind, tubhyamev samarpaye.

(Oh Supreme being! this is yours, this is dedicated to you.)

Acknowledgements

I would like to take this opportunity to express my deep sense of gratitude to my advisor, Prof. Manolis Doxastakis. His constant push and guidance has enabled me to walk beyond the boundaries of my comfort zone in the quest for knowledge. He has been the best mentor that one can ask for. Dr. Manolis, thank you for your constant guidance, encouragement, and support. The lessons that I have learned as a graduate student under your supervision will help me throughout my life.

I want to express my sincere gratitude to my committee members, Professors Ramanan Krishnamoorti, Gila Stein, Haleh Ardebili, and Yashashree Kulkarni for their valuable suggestions and insight about my research. I am also thankful to Prof. Jeffrey Rimer for his valuable insight and useful discussions about zeolites.

I am thankful to the Semiconductor Research Corporation and Goodyear Corporation for providing the financial support for my graduate research. I would also like to thank my industrial collaborators, Dr. Craig Burkhart, and Dr. George Papakonstantopoulos (Goodyear Corporation) for providing their valuable insight about my research work on polymers.

My sincere thanks to my colleagues, Dr. Lorant Jánósi, Dr. Anupam Prakash, Dr. Ginusha Perera, Abhijit Patil, Alexandra Lupulescu, Wei Dai, and Alexander Brayton for their help and useful discussions. Also, sincere thanks to system administrators, Mr. Bryan Bales and Mr. Jeffrey Sarlo, for keeping our clusters running and taking care of the hardware/software issues.

I want to thank Dr. Srimoyee Bhattacharya for always being a great supporter and extending all the help in the times of need. I extend my deepest thanks to Dr. Manoj Yadav, Dr. Sameer Israni, Dr. Pratik Bhagunde, Dr. Ajay Pratap Singh, Dr. Pranit Metkar, Aditya Kumar, Arun Kota, and Priyank Maheshwari for their

friendship, support, and encouragement.

To my family, Dr. Shyam Krishna Pandey (Father), Mrs. Lata Pandey (Mother), Jitendra Narayan Pandey (Brother), and Ruchi Mishra (Sister-in-law), without your blessings, encouragement, love and care I would not have completed this dissertation. I am blessed to be a part of such a loving and caring family. I believe that the completion of my doctoral studies will fill you all with great joy.

A SIMULATION APPROACH TO THERMODYNAMICS IN INTERFACIAL PHENOMENA

An Abstract

of a

Dissertation

Presented to

the Faculty of the Department of Chemical and Biomolecular Engineering

University of Houston

In Partial Fulfillment

of the Requirements for the Degree

Doctor of Philosophy

in Chemical Engineering

by

Yogendra Narayan Pandey

May 2013

Abstract

Industrial applications such as production of high performance polymer-nanocomposites, semiconductor fabrication, and catalysis involve molecular level phenomena governed by interfacial interactions. Precise control of these interactions will leverage the performance of materials in these applications. However, the ability to tailor the molecular characteristics is hindered by incomplete understanding of the controlling factors. This dissertation is broadly divided in three parts discussing the development and application of modern computational methods to elucidate such characteristics.

In the first part, detailed atomistic simulations of polymer-nanoparticle systems are performed by coupling preferential sampling techniques with connectivity-altering Monte Carlo algorithms to address the challenges in modeling polymer melts in proximity to a solid. The results reveal that polymer architecture holds a prominent role in systems with nanoscopic particles. Furthermore, a scheme for developing coarse-grained models of polymers with specific chemistry in contact with the solid surface is presented and quantitatively evaluated. These models are necessary to address the larger length scales required for study of polymer-particle mixtures.

Interfaces and substrate interactions play an important role for increasingly thinner polymer films employed in the semiconductor industry. There is a clear need to develop predictive models capable of describing reaction-diffusion phenomena in chemically-amplified resists and analyze their performance as a function of film thickness. In this dissertation, using mesoscopic models it is found that a central aspect governing reactions is the anomalous diffusion of the photogenerated acid. The anomalous diffusion coupled with a simple second-order acid

annihilation scheme quantitatively captures experimental data for all practical conditions - with only two adjustable parameters. The need to combine the developed scheme with substrate interactions is demonstrated.

Finally, the mechanism of zeolite crystal growth in solutions in the presence of growth modifiers is probed by employing atomistic simulations. It is hypothesized that molecules preferentially bind to specific crystal surfaces, which alters the crystal morphology. Using free energy calculations, the affinity of these molecules to interact with model zeolite surfaces is estimated. Distinct free energy minima and orientations of the inhibitor molecule in these minima are characterized and quantified providing a unique molecular understanding of the phenomena.

Table of Contents

List of Figures

List of Tables

Chapter 1 Introduction

The interfacial boundary separating the two phases, e.g., melt and solid, has distinct characteristics [3, 11, 12] which can be at the origin of unique chemical and physical material properties. One of the examples containing such boundaries are polymer-particle mixtures, which are essential for designing materials with improved mechanical, electrical, barrier and fire retardant properties [13,14]. In these materials, interfacial layers often termed as “bound polymer layers” can provide steric stabilization and hinder aggregation of nanoparticles [11]. Such stabilization can address the challenge of dispersing nanoparticles in a polymer matrix [15,16]. Good dispersion of nanoparticles facilitates interfacial contact with the polymer and is critical in achieving desired properties [17,18]. In addition, bound layers formed around the individual nanoparticles can form a percolating network (Figure 1.1), which can provide superior mechanical properties to the nanocomposite [19, 20]. For getting appropriate nanocomposite properties, various interactions in the immobilized layer must be fine-tuned [21].

In polymer bound layers, interactions of the polymer and nanoparticle at the interface are a key parameter [15, 22–24] and are determined by both enthalpic and entropic contributions. Despite extensive studies [20, 25–30], quantitative measures of the interactions between nanoparticles and polymers remain challenging and several studies have aimed at providing significant insight into such phenomena [3, 20, 29–36]. A broad set of techniques ranging from self-consistent field theory [18, 37–41], lattice models, molecular simulations (Monte Carlo and molecular dynamics) and properly designed experiments have been employed. It

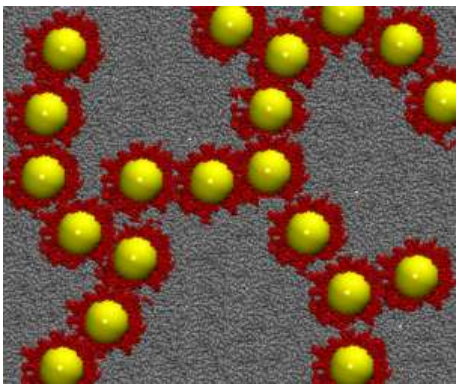

Figure 1.1: Schematic representing percolating network formed by interacting polymer bound layers. Yellow spheres depict nanoparticles and red beads represent polymer bound layers.

is established that nanoparticles impose significant structural changes to a polymer melt leading to stark differences in properties such as the glass transition temperature [42] and average shear and Young's modulus [13]. Enthalpic and entropic contributions coupled with polymer-mediated inter-particle interactions (for any finite concentration of nanoparticles) [11, 20, 43, 44] also affect the mechanical strength of these materials. In addition, nanoparticle curvature [6, 45–48] significantly alters the properties and conformation at polymer-nanoparticle interface. The local stiffness of polymer [6, 49] has also been shown to play crucial role in properties of polymer-nanoparticle interface. Chapter 3 of this dissertation discusses such effects with the help of atomistic simulations.

Another interesting application of the interfacial phenomena is realized in the semiconductor fabrication, where polymer films are deposited on a substrate. Fabrication of next-generation microelectronics devices at sub-22 nm resolution with minimal line-edge roughness (LER) require materials, which are highly sensitive to radiation. Chemically-amplified (CA) resists can meet the requirement of sensitivity to radiation, however mechanically unstable features due to high aspect ratio pose a significant challenge. Ultrathin films can be instrumental in addressing

such issues, but quantitative understanding of chemical and physical parameters that control image formation in ultrathin films still lacks. Furthermore, interfacial effects near the substrate and the free surface (Figure 1.2) become important in ultrathin films [50, 51] and affect image formation [52]. Dimensional control in thin film resists is mediated by the diffusion and reaction of photogenerated acid within a polymer resist matrix [53]. A coupled reaction-diffusion process has been described by a number of studies in past [4, 51, 54–57], which include continuum models for predicting temporal evolution of reaction-diffusion front by numerical simulations [4, 51, 54] and mesoscale 2D Kinetic Monte Carlo simulations [58, 59]. In spite of these efforts, the quantitative prediction of the image formation process in high spatial resolution remains an aim for industrial applications. Efforts for quantitative estimation of physical parameters by 3D simulations incorporating existing knowledge of interfacial phenomena in thin films [60, 61] are discussed in a section of this dissertation.

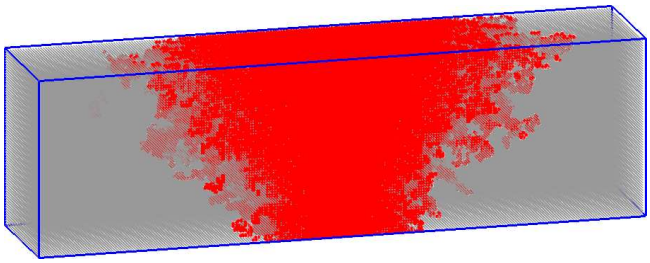

Figure 1.2: Snapshot depicting interfacial effects in chemically amplified resists. A broadening of deprotected feature shape due to higher mobility near the free surface and narrowing near the substrate due to slower diffusion is illustrated.

Zeolites e.g. ZSM-5 have extensive applications in catalysis [62] owing to the large interfacial area they offer for the reactants. In addition, shape selectivity of zeolites plays a pivotal role in their application as molecular sieves [63]. It is desired to precisely control zeolite morphology to overcome severe mass transport limitations and inferior shape selectivity. Morphology control is often directed at

minimizing the diffusion path length and reducing the tortuosity of channels. In a bio-inspired approach, Lupulescu and Rimer [1] employed zeolite growth modifiers (ZGMs) in combination with structure directing agents (SGA) showing a promise to control the zeolite crystal growth. The mechanism of growth control is hypothesized as preferential binding of ZGMs at the zeolite-solvent interface to the specific crystal surface [1]. As demonstrated in Figure 1.3, ZGMs attach on a preferred crystal surface and hinder the crystal growth. This leads to non-preferred crystal surface grow faster. In this dissertation, free energy simulations of ZGMs and model zeolite surfaces are employed to validate the hypothesis of preferential adsorption. The results from these simulations attempt to explain the thermodynamic origin of growth inhibition phenomena.

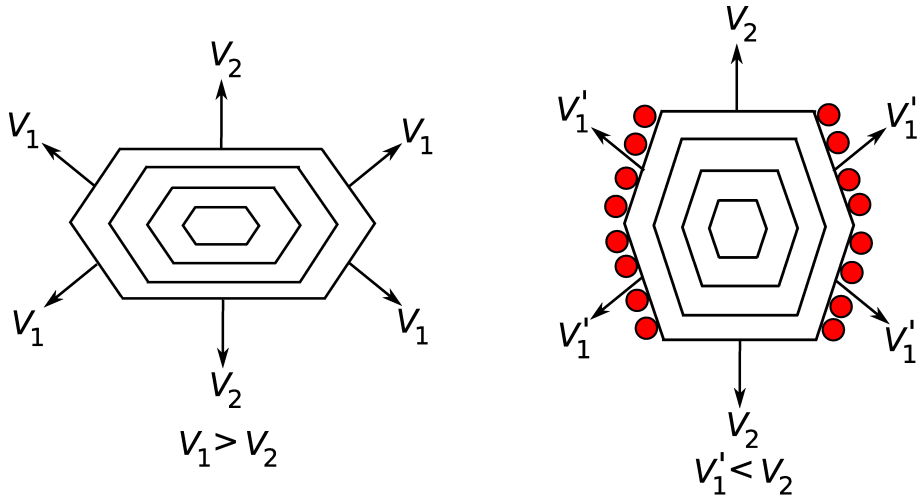

Figure 1.3: Growth inhibitor molecules (depicted by filled red circles) are hypothesized to alter the natural growth (left) of the zeolite crystals to provide thinner crystal along specific crystal dimension by preferential binding (right). Adapted from Lupulescu and Rimer [1].

1.1 Outline

Chapter 2 provides background of the simulation problems discussed in this dissertation. Chapter 3 presents simulation methods developed for the atomistic simulations of the polymer in proximity of the surface. Results from these simulations for characterizing the polymer bound layers are discussed in detail. Furthermore, a methodology for developing coarse-grained models for polymer-nanoparticle interactions is provided in Chapter 4. Chapter 5 outlines simulations of chemically amplified resists and provides a discussion on the quantitative insight gained from the results. Chapter 6 presents molecular simulations of the zeolite growth modifiers and details the findings of free energy calculations. Finally, Chapter 7 summarizes the results and provides a brief discussion on the future research directions.

Chapter 2 Background

2.1 Molecular Simulations of Polymers-Nanoparticle Systems

2.1.1 Simulations of Polymer Melts

Molecular Dynamics (MD) and Monte Carlo (MC) simulation methods are widely used for studying polymer melts and nanocomposites. One of the biggest challenges in simulation of polymer melts is sufficient sampling of uncorrelated and drastically different polymer configurations that are part of the studied ensemble. The relaxation times (τ) scale with polymer molecular weight (M) as $\tau \propto M^{3.4}$ [64]. Therefore, relaxation and conformational sampling of higher molecular weight polymers by MD simulations becomes infeasible due to inaccessible computational times. To address these issues and overcome the limitations on sampling the polymer configurations, previous studies [2, 65–69] have proposed connectivity altering moves for sampling polymer configurations more efficiently in less computational time than MD and classical MC simulations. In addition to the classical MC moves at local length scales, connectivity altering MC moves (Figure 2.1 and Figure 2.2A) are also incorporated in the simulations of polymer-nanoparticle systems. Some of such MC moves used in simulations are 1) volume fluctuation, 2) random monomer displacement, 3) reptation, 4) configurational bias of heads and tails, 5) rebridging configurational bias (RCB) of inner sections [66], and 6) configurational bias double bridging (DB) [2, 69].

Some of these moves propose unphysical changes in the polymer conformation. Volume fluctuation and random monomer displacement moves change the

structure at local length scales and are important for equilibrating the polymer melt and getting polymer properties in agreement with the experimental measurements. Other moves, namely reptation, configurational bias of heads and tails, rebridging configurational bias of inner sections and configurational bias double bridging change the chain conformation at higher length scales. Configurational bias of heads and tails and rebridging configurational bias of inner sections involve one chain whereas configurational bias double bridging involves two polymer chains.

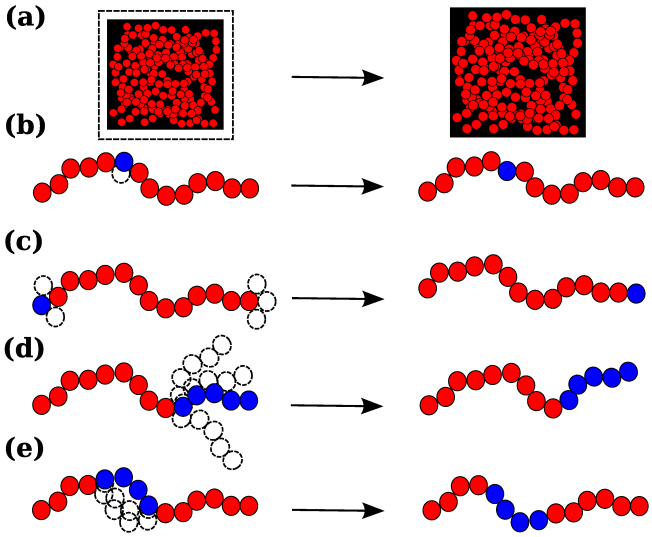

Figure 2.1: Moves incorporated in polymer melt simulations (a) volume fluctuation, (b) random monomer displacement, (c) reptation, (d) configurational bias of heads and tails, and (e) rebridging configurational bias of inner sections. Beads in blue color on the left side of arrow show the chain segment selected for the move. Dotted beads show the proposed trial positions and beads in blue color on the right side of arrow show new position of selected segment after the move.

In configurational bias of heads and tails, head or tail of a polymer chain is selected and a selected number (randomly chosen) of monomers adjacent to the head or tail are cut and regrown. Similarly, in configurational bias intra bridging, a selected number of monomers excluding the monomers adjacent to head and tail are cut and regrown within the chain. In these moves, a number of trial directions are selected in order to find an appropriate bridging position. Often, a large number

of trial directions (up to 64) are attempted for each move in order to find a suitable bridging position. These moves change chain conformation much rapidly than the classical MC moves.

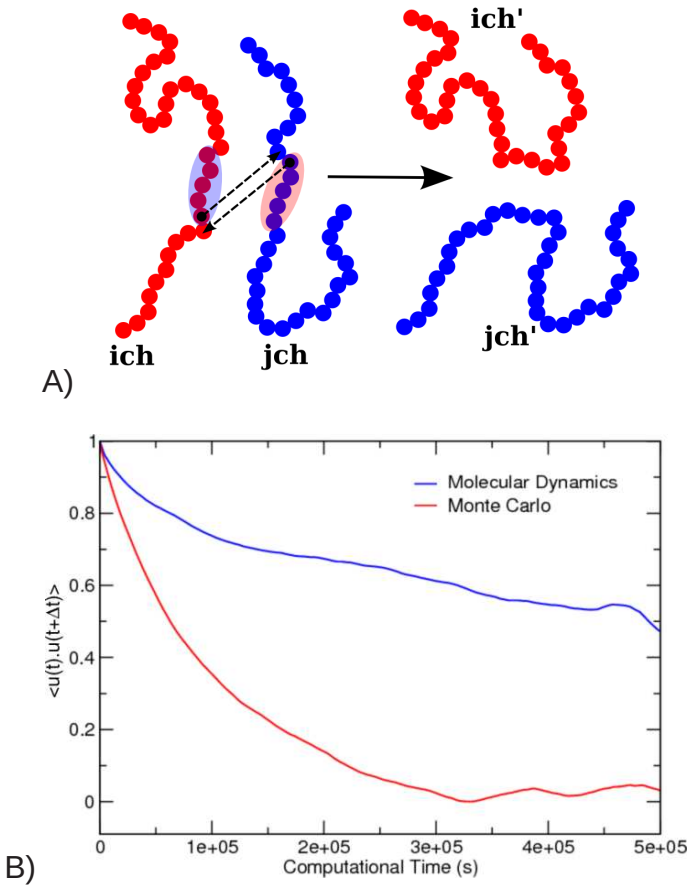

Figure 2.2: A) Figure illustrating configurational bias double bridging move. The sections to be excised from the two chains are highlighted. Arrows show the position, where excised parts connect on the other chain. B) End-to-end autocorrelation function for polyethylene chains with 1000 monomeric units at 600 K. MC simulations [2] with connectivity altering moves provide rapid relaxation.

The most important and radical move is the configurational bias double bridging of chains. Figure 2.2A shows local configurations of two chains before configurational bias double bridging move. In this move, a bridge containing a selected number of atoms on two chains is excised from the chains participating in double bridging. Then, end of the bridge on the first chain (ich) is connected to the site

created due to excising the bridge on the second chain (jch). Similarly the end of the bridge on the second chain is joined to the vacancy created on the first chain. This move creates chain configurations (ich' and jch') which are radically different than the initial chain configurations. This drastic change in chain structure leads to faster diffusion of chain center of masses and enables better sampling of chain conformations. Figure 2.2B shows the end-to-end vector autocorrelation function for polyethylene melt containing 1000 monomers at 600 K temperatures. A decay of this function to zero is an indicator of polymer relaxation. The connectivity altering MC algorithms facilitate rapid equilibration of the conformations, which is not attainable by MD simulations within accessible computational times.

Another possible way of achieving enhanced sampling of polymer conformations involves coarse-grained (CG) representation of polymers. Use of CG models to represent polymer and particle comes from the motivation of reducing the number of energy calculation to be performed in the simulations. During the coarse-graining process, chemical structure of monomers is suppressed [70] and a number of atomic monomeric units are bundled into a CG bead. It is imperative to choose CG bead mapping so that the number of potential terms used in defining the polymer structure are reduced without compromising with the predicted structural properties.

A number of coarse-graining approaches are mentioned in literature [7, 71, 72]. Automatic simplex optimization method [71] optimizes nonbonded and bonded interaction parameters for CG mapping of atomistic models. The simplex optimization targets at matching the structural properties such as radial distribution functions (RDF) obtained from CG and atomistic models. The objective function in this method is a least squares difference of the CG system RDF $g_{\mathrm{CG}}(r)$ and target RDF from atomistic simulations $g_{\mathrm{t}}(r)$.

Iterative Boltzmann Inversion (IBI) method [7] uses a simple Boltzmann inverse of RDF $g(r)$, which leads to free energy

$$F(r) = -k_{\mathrm{B}}T \ln g(r). \tag{2.1}$$

This free energy can be used as an initial guess of potential $V_0(r)$. The initial guess is then corrected by a correction term $-k_{\mathrm{B}}T\ln[g_0(r)/g(r)]$. In an iterative scheme, corrected potential can be calculated by

$$V_{i+1} = V_i(r) - k_{\mathrm{B}}T \ln\left(\frac{g_i(r)}{g(r)}\right). \tag{2.2}$$

The potential convergence is tested by calculating least squares difference of $g_{\mathrm{CG}}(r)$ and $g_{\mathrm{t}}(r)$. [73] The convergence of this iterative process indicates a valid unique solution for the potential $V(r)$, which will reproduce the RDF $g(r)$.

Harmandaris et al. [72] prescribed a hierarchical modeling approach for coarse-graining of polystyrene (PS). A similar procedure was used in a previous study for coarse-graining of flexible polymer chains consisting of CH_2 units [74]. In this approach probability distribution function P^{CG} for bonded interactions, which in general are unknown functions of the CG bond lengths r, bending angles θ and dihedral angles ϕ can be factorized as [75]

$$P^{\mathrm{CG}}(r,\theta,\phi,T) = P^{\mathrm{CG}}(r,T)P^{\mathrm{CG}}(r,\theta)P^{\mathrm{CG}}(r,\phi). \tag{2.3}$$

The independent probability distribution function can then be used for calculating CG potentials by inverse Boltzmann relations

$$U^{\mathrm{CG}}(r,T) = -k_{\mathrm{B}}T \ln P^{\mathrm{CG}}(r,T) + C_r, \tag{2.4}$$

$$U^{\mathrm{CG}}(\theta,T) = -k_{\mathrm{B}}T \ln P^{\mathrm{CG}}(\theta,T) + C_\theta, \tag{2.5}$$

$$U^{\mathrm{CG}}(\phi,T) = -k_{\mathrm{B}}T \ln P^{\mathrm{CG}}(\phi,T) + C_\phi, \tag{2.6}$$

where C_r, C_θ and C_ϕ are constants for setting minimum potential to zero. Non-bonded interaction potentials are given by potential of mean force (PMF) between

atomistic units representing CG beads at different separations of center of mass. This approach requires rigorous sampling of configurational space for obtaining the PMFs representative of nonbonded interactions at a given separation.

In case of polymer-particle systems, it is essential to have good estimation of polymer-particle interaction potential parameters for predictive simulations. Such potential parameters can be calculated by rigorous density functional calculations [76] accounting for many body interactions [77–79]. Alternatively, analytical expressions providing the basis for calculation of interaction potentials [80–83] in systems with polymer in contact with a surfaces are also available. Another approach [84] incorporates IBI method to derive effective potentials for CG representation of polymer and nanoparticle. Following section provides details of the studies focusing on polymer-particle systems employing the interaction potentials derived using some of approaches mentioned here.

2.1.2 Simulations of Polymers at Interfaces

Atomistic models of polymers and nanoparticles are predominately used for simulating single particle in the matrix of polymer chains or two particles in solvent [85]. Atomistic simulations of a single particle immersed in the polymer matrix are described in literature for studying polymer properties in the vicinity of graphite sheets [30, 31, 86] and silica nanoparticles [6, 33, 36, 87, 88].

Early studies of atactic polypropylene on graphite surface [31] using Monte Carlo (MC) simulation method showed that a region of 1 nm from the surface exhibits significantly different properties than bulk polymer. In these simulations, graphite interaction with polymer were modeled by “soft-wall” potentials. It was shown that polymer chains orient with their longest dimension along the graphite plane, while backbone bonds try to orient themselves parallel to the graphite plane.

MD simulation studies [86] showed that dynamics properties vary over a layer of 1.5 nm or almost twice the thickness over which density profile varies. Almost similar findings were reported in another fully atomistic MD study of poly(ethylene oxide) (PEO) oligomers and silica nanoparticles, [87] where flattened PEO backbone and a dynamic layer extending over twice the width of density fluctuation layer was observed. While these studies considered oligomers or relatively shorter chains, Brown et al. [33] used united atom (UA) polyethylene chains up to degree of polymerization of n = 1000 with atomistic silica nanoparticles of radius up to 6.0 nm. Interactions between polymer and particles were considered to be purely repulsive in nature. These systems contained more than 700,000 atoms. The MD simulations of 1500 ps were used for providing estimated properties of these systems. It was observed that irrespective of polymer molecular weight and particle radius, perturbations in polymer density were observed up to 2 nm from the particle surface.

In another atomistic MC simulation study of polyethylene on graphite surface [30], the interactions of graphite surface and polymer were defined as a combination of 10-4 and 9-3 potentials. Such kind of potentials for modeling substrate were mentioned in previous work [70]. This study followed Scheutjens-Fleer theory [27, 89] to characterize the polymer conformation in the vicinity of graphite surface. The polymer chains adsorbed on the graphite surface were subdivided into train, tail and loop segments. It was observed that limiting length of train segments was 2.5 times the Kuhn segment length of polymer. Also, train segments showed a tendency of forming all-trans sequence on the graphite surface. This is similar to the observations of flattened backbone [86, 87] in previous studies. The probability distribution of train segment lengths showed a sharp minima at train lengths of 4-5 bonds. A maximum probability for train segment length of 7 bonds was followed by a subsequent monotonic decay for longer train segments.

One interesting finding of these distributions was an extremely high probability of train segments equal to chain length in case of shorter ($\sim$ 40 monomers) chains, however for long enough chains this probability drops to zero. Entropic penalty for having whole chain adsorbed is compensated by enthalpic interactions with the graphite for short chains, whereas effective interactions of longer chains are dominated by the entropic losses and longer train segments are not favored.

Recent MD studies [36, 88] used atomistic models of 20 monomer atactic PS chains and silica nanoparticles to study the interface between silica nanoparticles and PS melt. Both bare and grafted nanoparticles were studied. It was observed that perturbations in density diminish at a distance beyond $\sim$ 2 nm from the silica surface. Furthermore, for grafted particles an increase in grafted chain density lead to reduced interpenetration between grafted chains and free chains. This reduction becomes unfavorable for the mechanical stability of silica nanoparticles in PS matrix, which is undesirable for well-reinforced composite material.

Experimental studies using silica filled elastomers [42] have shown a gradient in glass transition temperature (T_{g}) near the particle surface. This gradient in T_{g} was attributed to a glassy layer of polymer formed around the nanoparticles. All of the above atomistic simulation studies have observed higher polymer density near the particle surface. In fact, presence of dense polymer in near surface regions supports the formation of a glassy layer, which is attributed to enhanced mechanical properties of filled polymers in previous simulations studies [13, 90]. The extent of this glassy layer or immobilized bound layer also depends upon the size and curvature of the nanoparticle. Harton et al. [3] employing a suite of experimental techniques measured the thickness of these layers. For poly(2-vinylpyridine) around 15 nm silica nanoparticle, the bound layer thickness was found to be $\sim$ 1 nm, which was significantly lower than 4-5 nm thick layer in the proximity of flat

silica surface. These effects observed by experiments make the study of interface of polymer melt and particle surface even more intriguing. In addition, lattice simulations based upon self-consistent mean-field theory [26, 27] revealed $\approx 50\%$ decrease in the root-mean-squared bound layer thickness (δ_{RMS})for particles of the size comparable to polymer Kuhn length as compared to δ_{RMS} at a flat surface (Figure 2.3).

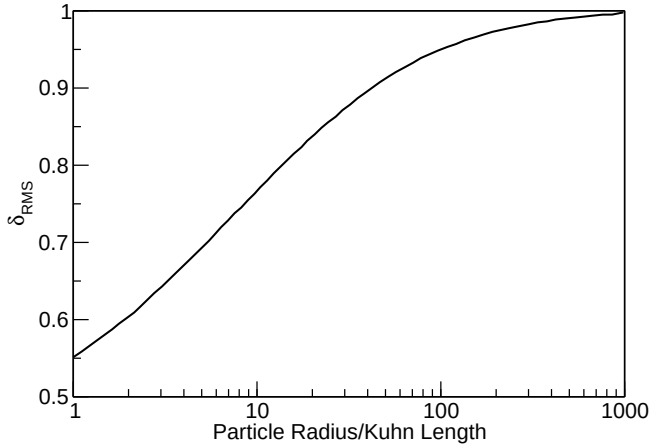

Figure 2.3: Predictions based upon self-consistent mean-field theory showing particle size dependence of polymer bound layer thickness. Adapted from Harton et al. [3].

While above mentioned atomistic simulation studies provide a good insight on polymer conformation in the limit of very dilute dispersion of particles, the more interesting scenario of a finite concentration still remains to be investigated. To the author's best knowledge, there are no fully atomistic simulations of "long" polymer with multiple particles. However few studies have tried to study oligomer grafted nanoparticles in solvents [85]. As mentioned previously, the large system size requirement of fully atomistic models [6, 33] renders simulating finite concentration of particles in explicit polymer matrix in atomistic details infeasible. Approaches for addressing such limitations in the computational studies of more than one nanoparticles in the polymer matrix become essential for elucidating the complex interactions at the contact of polymer and nanoparticles. One way of addressing these

challenges is use of CG description of polymers and nanoparticle.

A number of studies have used CG representations of different polymers in contact with the particles to investigate the polymer-particle interface. Some of these studies focused on studying the structure and properties of bare and grafted single particle immersed in polymer matrix [32, 35, 46, 84, 91–93]. Doxastakis et al. [32] used a bead-spring model of polymer to study depletion layer near the single nanoparticle. It was observed that the thickness of depletion layer was roughly of the order of R_{g}. Furthermore, the polymer segments close to the nanoparticle were found to align themselves parallel to the surface. The polymer chains in the proximity of the particle assumed a structure of flattened ellipsoid. Beyond the structure of polymer chains, CG models have also been used for understanding effects of polymer-particle interactions upon polymer dynamics.

A MD simulation study [91] using Kremer-Grest bead-spring model of polymer and variable strength of nanoparticle-polymer interactions discussed the polymer transport in nanocomposites. The interactions were defines as “repulsive,” “attractive” and “strongly attractive.” Potential terms for polymer-particle interactions were obtained by integrating the Lennard-Jones (LJ) interactions potentials. The results showed that chain diffusivity is increased by 15%-20% near the repulsive surface, whereas a reduction of 40%-50% is observed near the strongly attractive surface. While the strength of interactions is the only parameter considered in polymer dynamics near bare particles, the entanglements between grafted particles and surrounding polymer melt can influence polymer dynamics. Employing bead-spring model of polymer and grafted nanoparticles, effects of grafting density on entanglements were investigated [46]. The nanoparticles were composed of particles of monomer diameter σ and density ρ_{NP} distributed uniformly over the sphere of radius R. Effective potential between polymer and particle was obtained by integrating truncated and shifted LJ potential. Following the MD simulations,

primitive path analysis [94] (PPA) was performed to study entanglements between the grafts and polymer matrix. It was observed that maximum entanglement density coincided with the monomer density peak and scaled with grafting density (Σ) as $\Sigma^{1.4}$. Also, the fractions of graft-melt entanglements were found to scale with product of graft and melt monomer densities and indicated "binary" entanglements.

The above mentioned studies used simplistic CG representation of a polymer molecule, but during the recent years focus has shifted towards using polymer and particle models, which account for the chemistry of polymer and particle surface. Ghanbari et al. [84] used CG representations of bare and grafted silica particles and atactic PS melt obtained from IBI method. In order to verify the transferability of these CG potential, the polymer density distribution functions obtained from CG simulation was compared to the atomistic density distributions. Both CG and atomistic simulations showed that the perturbations in polymer density and preferred orientation of monomers persist within $\sim$ 2 nm distance from the surface. The matrix chains shorter than grafts penetrated the brush, whereas longer matrix chains were expelled. This wet-to-dry brush transition was found to be less pronounced upon reducing the grafting density.

The results from the single nanoparticle simulations show that the effects of nanoparticle immersion in polymer matrix such as density perturbations, preferred orientation, polymer entanglements can be described by using CG representations. Still, understanding the effects on the stability of dispersion and mechanical reinforcement needs further investigation of interactions between multiple nanoparticles.

The studies involving multiple nanoparticles in explicit polymer in CG representation [83, 95–106] have focused on addressing a number of topics of interest. These topics include calculation of PMF between two particles as a function of

their separation [98, 106], polymer entanglements [102], steric stabilization [100] and self assembly of grafted nanoparticles [99, 103–105].

Earlier studies by Vacatello [95–97] used 12-6 LJ potentials to describe the polymer-polymer, polymer-particle and particle-particle interactions potentials. These studies employed MC simulations to understand arrangement in polymer nanocomposites. Chains were found to be interacting with multiple particles causing "bridging" interactions between multiple nanoparticles. The polymer chain in nanocomposite was pictured as a sequence of interface, loops and bridges between particles. It was hypothesized that average length of these polymer segments depends upon the polymer stiffness, a result that has been recently emphasized by detailed atomistic simulations [6].

In fact, polymer rigidity is a very important factor that affects the interactions of polymer with particles and should be accounted for in CG models of polymer at the particle interface. Polymer density at the surface of particles is significantly affected by local stiffness of polymer chains [6] although the effects of polymer chain length upon the density are not as profound [83]. The structure and density of polymer at the interface has shown to have effects on the effective forces between two nanoparticles [98]. A higher polymer density in interface region (for strong polymer-particle interactions) provides a stable bulk phase in inter-particle region. Strong polymer-particle interactions make aggregation of nanoparticles entropically unfavorable.

Similar effects of changes in strength of polymer-particle interaction (ϵ_{mp}) on the stability of dispersion demonstrated that weak interactions allow particles to form a cluster whereas strong interactions lead to well dispersed arrangement of particles in polymer matrix. Crossover from clustered arrangement to dispersed state is marked by a sharp maxima in specific heat capacity of the system per

nanoparticle [100]. These findings suggest that tuning polymer-particle interactions can be one possible way of controlling the arrangement of nanoparticles in polymer matrix. Another way of nanocomposite morphology control is grafting the particles with polymer chains and fine tuning the length of these grafts relative to matrix polymer chain length. Increasing bulk polymer chain length for a constant length of grafted chain has shown a change in PMF between grafted nanoparticles to go from purely repulsive to attractive [106]. Such effects of grafted chain lengths can have significant impact upon self assembly of grafted nanoparticles.

Akcora et al. [103] studied the self assembly of grafted nanoparticles in implicit polymer. In this study, grafted chains were modeled as bead necklace chains. Interactions between polymer-polymer and polymer-nanoparticle were modeled by hard-sphere potential, whereas interactions between two nanoparticles were modeled by square-well attractive potential. It was shown that variation in the number of grafted chains and graft length significantly alters the morphology of the self-assembled structures. It should be noted that grafted chain induced forces between surfaces become significant only for for high grafting density, which lead to extended conformation of grafts [101]. Both experiments and simulations illustrate that polymer grafts can be used for manipulating interactions between nanoparticles and hence tuning the mechanical reinforcement and morphology in polymer nanocomposite melts [103, 104].

The particles can serve as polymer entanglement attractors upon deformation [102, 107]. Using CReTA algorithm [108], Riggleman et al. [102] showed that under normal condition, polymer entanglements near particles are reduced. But, as the deformation of the matrix proceeds, particles trap the polymer primitive path and cause increased number of entanglements. This increase however does not alter the response of system to deformation.

The CG studies listed above have used homopolymer models, where chemical structure of polymer was captured by a single bead substituting certain number of atomistic units. The situation becomes more involved in case of copolymers, where it becomes inevitable to use different kind of beads to depict chemistry of different blocks of copolymer. Copolymer functionalized nanoparticles [105] using AB copolymers with alternating or block sequences illustrate that variations in interactions between copolymer monomers can direct the self assembly of particles. Such findings emphasize the need of including chemical details of monomers in modeling the polymer and their interactions with particle surface, which is a topic discussed in detail in Chapter 4 of this dissertation.

2.2 Simulations of Projection Lithography

Projection lithography has emerged as an effective technique for fabrication of microelectronic devices. Efforts to model the lithography processes as mathematical equations have paved the way for evolution of lithography as a science rather than treating it as an art [109]. The first account of such mathematical foundation of lithography was published by Dill [110] in 1975, which provided the accurate description of semiconductor optical lithography [109]. It is noted that the development of automated thin-film measurement equipments was a trigger event behind the first quantitative expression in lithography commonly known as Dill's model [111]. The simulations employed in lithography have matured significantly over past three decades. Earlier in 1985, two dimensional simulations were used for modeling conventional resists. These simulations were scalar and absolute accuracy of results was not expected. During recent years, simulations are capable of modeling lithography processes in three dimensional details and implement vector calculations [109].

Following the Moore's law, microelectronic devices are accommodating more and more components per unit area. A direct implication of such growth is reduced size of the features and patterns engraved on the microelectronic devices. Non-photo technologies such as extreme UV (13.4 nm) and projection electron beams are conceived as the next generation lithography technologies. These technologies require high resist sensitivity for wafer throughput. Development of chemically amplified resists (CA) resists, which meet the expectations of such sensitivity have accelerated the growth of microelectronics industry, but resolution limit of chemically amplified resists due to acid diffusion or resolution limit of polymeric resist remains a challenge [112].

One of the biggest challenge in modeling of CA resists is limited availability of predictive modeling techniques. Experiments have shown a very strong front propagation behavior in resists during post-exposure bake (PEB) [113,114]. Quantitative description of such behavior requires simulations with uncertainty in the limit of $\sim$1nm. Such kind of stringent requirements make modeling of PEB more challenging than modeling of point defects and concentration dependent diffusion in silica [111]. Numerous studies in the past [4, 54–59, 113, 115–138] have attempted to focus on modeling and simulation of different aspects of lithography processes. These efforts range from modeling the whole lithography process [129] to latest efforts for understanding the basic phenomena behind image formation during PEB [54, 55, 59, 134, 138]. Following sections attempt to summarize the modeling and simulation efforts to understand reaction-diffusion phenomena that describes front propagation during PEB.

A variety of models have been implemented for studying the coupled reaction-diffusion phenomena during PEB. Most prominently continuum models [4,55,113, 115,117–122,124,125,127,128,133,137,138] and mesoscale models [58,59,131,

134, 135] have been employed to develop quantitative understanding of front propagation. Salient features and formulations for such models are discussed briefly in the following sections.

The above mentioned models have been implemented in a numerous studies. Most commonly studies using continuum model relied upon numerical solution of differential equations representing acid diffusion, polymer deprotection and acid-trapping [4, 54, 55, 138]. Mesoscale models employ stochastic simulations such as kinetic Monte Carlo (KMC) method to obtain stochastic evolution of front propagation [58, 59, 116, 134]. A good description of KMC methodology can be found in a comprehensive review by Chatterjee and Vlachos [139]. Some findings from the numerical and stochastic simulations are discussed briefly in the following sections.

2.2.1 Continuum Models and Numerical Simulations

Continuum models represent reaction-diffusion phenomena as a set of coupled differential equations. Earlier models to study the front propagation [4, 54, 55, 57, 121, 123] have focused on developing a quantitative understanding of the physical and chemical processes occurring in CA resists. Previous studies [123, 126] modeled the PEB process using fully coupled reaction-diffusion kinetics. Some continuum models described the diffusion of a photoacid generator (PAG) as Fickian diffusion [121, 122, 127] and solved the standard diffusion equation coupled with reaction kinetics to estimate quantitative parameters for reaction-diffusion phenomena. It has been acknowledged that non constant diffusion coefficients can be a possible avenue to be followed for improved resist modeling [127] and it has shown significant effect on image quality in 22 nm fabrication [56]. Estimation of an appropriate diffusion coefficient is a challenging task. A diffusion coefficient appropriate for describing short time behavior may not be able to describe long

time behavior observed in reaction-diffusion process. Unfortunately concentration dependence of diffusion coefficient is not fully understood and several functional forms are mentioned in literature [124]. Furthermore, extraction of realistic diffusion coefficients by using any model should incorporate essential chemistry to establish proper balance between reaction and diffusion. An incorrect estimation of chemical deprotection rate may lead to overestimation of diffusion rate [57].

Zuniga and Neureuther [117] proposed a coupled reaction-diffusion model implementing non constant diffusivity. This model used following differential equations to describe PEB process

$$P + H \xrightarrow{k_r} A,$$

$$\frac{\partial A}{\partial t} = -k_r(P_0 - A)H^m, \tag{2.7}$$

$$\frac{\partial H}{\partial t} = \nabla(D\nabla H) - k_l H, \tag{2.8}$$

$$D = D_0 \exp(\omega A), \tag{2.9}$$

where m is reaction order, k_l is acid loss rate and ω and D_0 are constants describing non constant diffusion rate. This formulation reduces to a reaction kinetics coupled with Fickian diffusion for ω = 0.

Beyond reaction kinetics coupled with Fickian diffusion, moving boundary acid transport model considering generation of free volume in resist polymer are also available in literature [119, 120]. It is hypothesized that thermal deprotection catalyzed by the PAG leads to production of volatile products. These volatile reaction products lead to generation of free volume, which enhances the local diffusivity of the acid. Relaxation following the creation of free volume densifies the polymer

and inhibits diffusion by trapping the acid present at deprotected site [119]. Furthermore, the time evolution of reaction-diffusion front in CA resists is self-limiting and can not be reproduced by Fickian diffusion alone [113,117]. These arguments lead to the concept of acid trapping mechanism.

A number of recent studies [4,54,55,137,138] have described the front propagation as a combination of reaction, non-Fickian diffusion and trapping process. The set of equations used in these models is expressed as

$$H_0 = [PAG](1 - e^{-CE}), \tag{2.10}$$

$$\frac{d\phi(x,t)}{dt} = k_P H(1 - \phi(x,t)), \tag{2.11}$$

$$\frac{\partial H(x,t)}{\partial t} = D_H \frac{d^2 H(x,t)}{dt^2} - k_T H(x,t)\phi(x,t), \tag{2.12}$$

where $\phi(x,t)$ and $H(x,t)$ are the deprotection level and acid concentration respectively. D denotes acid diffusion rate and k_P and k_T are reaction and acid trapping rate constants. [PAG] is initial PAG loading and H is acid concentration after exposure. E represents UV exposure dose and C is Dill's constant. For a high enough UV dose, initial acid concentration H_0 is simply equal to the PAG concentration [54]. Eqn. 2.11 shows first order dependence of deprotection rate upon acid concentration and protected polymer fraction. Moreover, Eqn. 2.12 describes rate of change of acid concentration with Fickian diffusion of acid combined with acid loss attributed to trapping of acid molecules in deprotected polymer sites. The results obtained from such models by numerical simulations are discussed in later sections.

Vogt et al. [4] used numerical solution of acid diffusion, deprotection reaction and trapping (Eqn. 2.11 and Eqn. 2.12) to model time evolution of deprotection profiles during post-exposure bake (PEB) of poly(methyladamantyl methacrylate) (PMAdMA) films with di(*tert* - butylphenyl) iodonium perfluorooctanesulfonate (DTBPI-PFOS) photo acid generator (PAG) at 130^{o}C. The coupled differential equations were shown to reproduce the self limiting behavior of reaction-diffusion front (Figure 2.4). The values of parameters defining front propagation were found to be k_{P} = 30 nm^3/s, k_{T} = 0.4 s^{-1} and D = 1 $\times$ 10^{-12} cm^2/s. In addition, it was mentioned that such parameters are reasonable for a slow, strong photoacid such as PFOS.

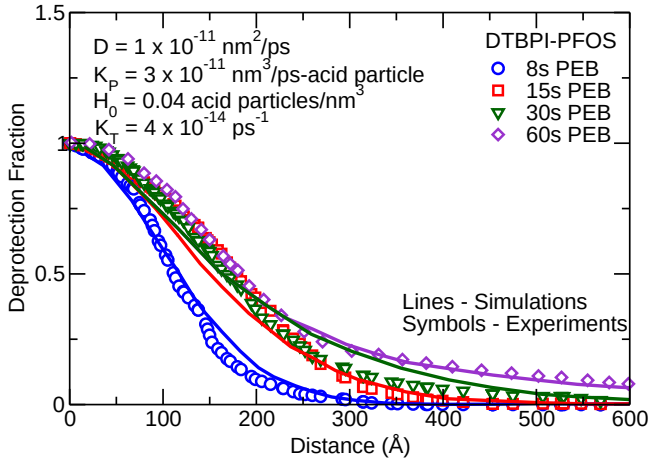

Figure 2.4: Deprotection profiles at different post-exposure bake times from experiments (symbols) and from numerical simulations (solid lines). Adapted from Vogt et al. [4].

Kang et al. [54] studied poly(hydroxystyrene-co-$tert$-butyl acrylate) or P(HOSt-co-tBA) resist with triphenylsulfoniumperfluorobutanesulfonate(TPS-PFBS) PAG. In their work, they used data from single layer and bilayer experiments to obtain the diffusion, reaction and trapping rates. Uniformly loaded single layer deprotection data was used for fitting k_{P} and k_{T} values by using Eqn. 2.11 and Eqn. 2.12 without considering the diffusion term. These k_{P} and k_{T} values were then used for evaluating D by fitting the front propagation data

obtained from bilayer experiments. This study provided k_{P} = 0.51 $\pm$ 0.06 nm^3/s, k_{T} = 0.028 $\pm$ 0.002 s^{-1} and D = 4.2 $\pm$ 0.3 nm^2/s for bake temperature of 90^{o}C. In addition Arrhenius prefactor (A) and activation energy (E_{a}) were also calculated for establishing the temperature dependence of k_{P}, k_{T} and D. Such information is helpful in understanding average deprotection at different distances along the reaction-diffusion front and in estimating the effective feature width, but little information can be obtained about phenomena e.g., LER and photoacid aggregation effects during PEB process. Such issues can be addressed by mesoscale models and stochastic simulations as discussed in the following section.

2.2.2 Mesoscale Simulations of Projection Lithography

Continuum models are used as a tool for fast simulation of resist performance and predicting global inhomogeneities [59]. Also, such models consider average quantities and assume homogeneous distribution of reacting species and products at smaller length scales. While informative in nature, such type of models have limited resolution and unable to probe spatial details of inhomogeneous distribution of species at fine resolution. Due to rapid advances in technology, the length scales of interest are approaching the size of individual resist molecule. Moreover, stochastic effects that govern development of images in resist film require models, which can probe molecular length scales and allow introduction of stochastic effects. Mesoscale models have been discussed in a number of studies [58, 59, 109, 131, 134, 135] and aim at capturing 2D [58, 59, 131] or 3D [134] details of resist feature shapes.

In mesoscale models, a 2D or 3D lattice is used for depicting the resist film. Each lattice cell depicts specified volume of protected polymer resist (e.g., 1 nm

$\times$ 1 nm $\times$ 1 nm). Distribution of the protecting groups in the resist is assumed to be uniform across the lattice [134]. Other additives, such as PAG, quencher base etc. are generated following specific distributions. Specifically, for generating PAG distribution inside the resist film, a Gaussian probability distribution is used [56, 130, 136]. More details about such distributions are discussed in a later section. Mesoscale models are often coupled with stochastic simulation methods e.g., kinetic Monte Carlo methods [134]. Simulations employing mesoscale models are capable of providing information about line edge roughness (LER), PAG aggregation and stochastic behavior of events such as acid diffusion inside resist film [59].

Studies with mesoscale models [58, 59, 131, 134, 135] target to provide high resolution description of image formation. Mesoscale simulations for development and rinse process using coarse-grained polymer models employing dissipative particle dynamics (DPD) were used to understand the origin of LER. In such simulations, it was observed that soluble polymer diffuses into the solvent phase, which leads to roughened line-edge constituted by residual polymer [135].

Recent simulation study by Lawson and Henderson [58] used a 2D mesoscale model and the KMC method to probe the effects of photoacid aggregation upon the LER. It was demonstrated that the larger size of aggregates leads to an increased shape asymmetry of the resolved pattern, where as the smaller aggregate size results in a reduction in LER. Furthermore, this study revealed that higher photoacid diffusion lengths smooth out initial photoacid distribution inhomogeneity.

Another study [134] using 3D mesoscale lattice model and KMC simulations probed the relationship between gradient in polymer deprotection and LER. The study concluded that gradient in polymer deprotection is a good indicator of LER

in some cases, but in certain condition LER can be attributed to other effects such as photoacid aggregation. These results indicate that 3D mesoscale simulations can provide information beyond the average quantities during the reaction diffusion front propagation.

2.2.3 Role of Acid Distribution

An important detail in modeling reaction-diffusion during PEB is generating adequate initial photoacid distribution. With the objective of studying resolution blur in resist films, Gaussian probability distribution functions were used in previous works [56, 130, 136]. Inhomogeneous distribution of PAG becomes a concern with reducing the feature size as it has significant impact upon LER. In CA resists, discrepancy between the ionization point and acid generation along with acid diffusion point contributes to resolution blur. Furthermore, it was noted that even if acid diffusion is suppressed, a resolution blur intrinsic to acid generation mechanism is still observed [130]. These observations emphasize the need of incorporating microfluctuations in acid concentration in modeling of PEB an CA resists. The microfluctuations are generated by multiplying the acid concentration by Gaussian function $f_{\text{mod}}(x, y)$ given by

$$f_{\text{mod}}(x, y) = \frac{I_c}{2\pi {\sigma_s}^2} \exp\left(-\frac{x^2 + y^2}{2{\sigma_s}^2}\right), \tag{2.13}$$

$$C'_{\text{acid}}(x, y) = C_{\text{acid}}(x, y) \times \prod_{i=0}^{n} \left(1 + (-1)^m f_{\text{mod}}(x - x_i, y - y_i)\right), \tag{2.14}$$

where m is a random number that generates 0 or 1, C'_{acid}, I_c and σ_s are modulated acid distribution, intensity of microfluctuations and size of microfluctuations respectively. It is noted that effects of acid diffusion lead to smoothing of the effects generated by microfluctuations [136].

These models and methods available for studying the reaction-diffusion phenomena in thin film CA resists have provided insight about qualitative and quantitative aspects of front propagation, but more progress is needed in order to match the growth driven by Moore's law. Rapid advances in the technology and further reduction of feature size demands the simulations at very fine resolution with uncertainty in the range of $\sim$1 nm. Furthermore, mechanical instability issues at nanosized features require ultrathin film resists, which have significant interfacial effects at substrate and free surface. Previous studies [50, 140–145] have discussed the interfacial effects on mobility in polymer thin films. It has been mentioned that polymer mobility is reduced close to the substrate [60, 61, 145], whereas enhanced polymer mobility is observed near free surface. Interfacial effects in thin films were not considered in previous works. These effects must be accounted for making the models of front propagation more quantitative and predictive in nature.

2.3 Molecular Simulations of Zeolites

Zeolites have garnered significant interest in simulation studies. Both MD simulations [146–151] and MC simulations [152–159] have been employed to study diffusion and adsorption phenomena in zeolites. While adsorption and diffusion of the alkanes and alcohols inside the zeolite channels was studies by a number of studies, some studies have also focused on the adsorption on the external surfaces of the zeolites [151, 160–165]. Framework flexibility [147, 149, 151, 152, 166–168] and a surface representative of zeolites [160, 161, 169] are among the important considerations in preparing model systems. For the framework flexibility, some studies have demonstrated that a flexible framework is imperative for predicting adsorption and diffusion in zeolites in agreement with the experiments [168]. On the other hand, a number of studies have claimed that framework flexibility does

not alter adsorption and diffusion estimates in zeolite channels significantly [147, 166, 167].

The issue of a representative model zeolite surface is of greater importance in the study of zeolite growth. Among the studies evaluating the model surfaces, Slater et al. [160] performed atomistic simulation of LTA zeolite surfaces. It was demonstrated that the surface shows three stable terminations, but the relative stability of these surfaces varies with the composition. Also, cations were found to cause extensive framework distortion. Another study [161] showed that the nanoscopic surface structures in zeolites do not arise simply from optimal packing of silicate tetrahedra, but the complex reactions of siliceous oligomers with the zeolite surface play a role in the determination of surface structure. Díaz et al. [169] probed surface structure of the MFI zeolites. It was found that different structure directing agents (SDAs) facilitate growth of different crystal morphologies. Tetrapropylammonium (TPA) cation was found to produce a hexagonal prismatic crystal morphology, whereas a trimer of TPA favored the growth of leaf-shaped platelike crystals. The differences in the morphologies in presence of different SDAs were attributed to capability of SDA to fit in the zeolite crystal structure and adsorption kinetics of SDAs on the external surface of growing crystals. It should be noted that during the synthesis of zeolites, intermediate crystal surfaces different than the most stable crystal surface may be formed [169]. However, consideration of all intermediate morphologies in simulation studies may not be feasible. A number of simulation studies [149, 151, 166, 167] have employed the most stable morphology as the model zeolite surface.

There are no previous molecular simulation studies probing the growth inhibition phenomena in the zeolite synthesis. Although, recently Salvalaglio et al. [170] have studied a similar phenomena during urea crystallization. This study employed well-tempered metadynamics [171] to investigate effect of additives such as biuret

and acetone on urea crystal growth. The free energy profiles from these simulations were shown to quantify the surface selectivity of the additive molecules. The simulations revealed that a higher selectivity of biuret molecule provides effective growth inhibition for [0 0 1] crystal surface. Similar free energy simulation methodologies can be employed for elucidating the mechanism of growth control realized by zeolite growth inhibitor molecules. A quantitative insight of growth inhibition mechanism will help in predicting inhibitor efficacy and achieving optimal growth control.

Chapter 3 Polymer Bound Layers and Nanoparticles

3.1 Introduction

The properties of interface between a polymer melt and a solid surface are at the heart of emerging technological applications, e.g., the design of nanocomposites with improved mechanical, electrical, barrier, and fire retardant properties. To a large extent, the polymer-nanoparticle interactions are considered an important parameter [15, 22, 23] in determination of the region within which perturbations to polymer structure are observed, which is often termed as “bound polymer layer” [11] or “immobilized layer” [3]. The thermodynamically stable bound layers are instrumental in providing steric stabilization and hinder aggregation of nanoparticles [11]. Furthermore, significant impact on the barrier properties of the resulting material is attributed to the interfacial layers [14]. During the past decades extensive number of studies have focused on quantitative measures of the polymer-nanoparticle interactions, but gaining quantitative insight remains challenging in spite of the broad set of techniques e.g. self-consistent field theory, lattice and molecular simulations (Monte Carlo and molecular dynamics) employed to study such phenomena [3, 20, 29–36, 172].

In particular, Monte Carlo (MC) algorithms are very efficient when employed moves drastically sample the configurational space of the system [173]. It was recognized in the early lattice simulations that in polymer melts, altering polymer connectivity can facilitate such sampling [174]. The approach of altering connectivity has been applied to study a wide range of polymer melts in atomistic detail, e.g., polyethylene [65, 175, 176], polyisoprene [67, 177, 178], polybutadiene [68],

polyethylene oxide [179] and more recently non-linear polymers [180, 181].

Despite the proven ability for the polymer melt simulations, connectivity-altering MC faces several challenges for the study of polymers in presence of interfaces. One of such challenges is manifested during the application of powerful end-bridging algorithm, which introduces polydispersity. Addressing the issue of polydispersity requires careful tuning of the spectrum of chemical potentials corresponding to chain lengths [182]. Alternatively, double-bridging technique can be used to accomplish the goal of drastic sampling, which allows consideration of strictly monodisperse systems [2, 69]. Unfortunately, double-bridging displays an exceedingly low acceptance rate in atomistic simulations (1 in 10^5 at 450K for polyethylene), which prohibits consideration of large systems that are often required to study interfaces between polymers and solid surfaces. Furthermore, the efficiency of the move in proximity of a surface is decreased compared to bulk. This decrease is due to reduction in free-volume and interaction of polymer with the surface.

Daoulas et al. [30] employed double-bridging moves to avoid polydispersity for study of polyethylene (PE) at a graphite surface (systems $\approx$ 20,000 atoms) and noted the difficulty in sampling tail, train and loop segments of the polymer in contact with surface as defined by the pioneering work of Scheutjens and Fleer [26, 27, 89]. Furthermore, system sizes required to avoid finite-size effects exceed multiple times the root-mean-square of the polymer radius of gyration R_g^0 of the bulk unconstrained melt [145], these challenges are exacerbated when long macromolecules (where connectivity-altering MC is advantageous [65]) are considered.

In recent studies, free-energy simulations employing preferential sampling

schemes [183] were designed for the systems where solvent contributions are critical to the phenomena studied [184, 185]. For small molecular solvents where simple molecular displacements are applicable, such techniques are clearly beneficial, nevertheless it is unclear whether a similar approach can be employed for long chain polymer molecules having substantial conformational degrees of freedom. In this chapter, we discuss the development and application of connectivity-altering Monte Carlo moves as local updates for polymer in proximity to a surface, coupled with global hybrid molecular dynamics (MD). The main subject of this study is a PE melt on a silica surface or around a nanoparticle and the changes induced by high-curvature of nanoparticles for the case where particle radius is comparable to the polymer Kuhn segment length.

The dispersion of nanoparticles is known to be significantly affected by the size of nanoparticles [24] and recent studies [45, 46] examined the curvature induced effects at the polymer-nanoparticle interface. Hone and Pincus [47] stated that entropic contributions have a critical role in preferential adsorption of polymer at the surfaces with low curvature. It should be noted that simple geometric arguments [186–188] can provide an interpretation of reduction in the thickness of adsorbed polymer layer upon decreasing the particle size up-to the Kuhn length [3, 13, 186–189].

An assumption that the polymer mass adsorbed per unit area is independent of particle size was made by Garvey et al. [187] Considering this assumption to be true, the effective layer thickness δ_{eff} defined as the ratio of total volume of adsorbed polymer layer on a particle to surface area should be reduced upon decreasing particle size or increasing curvature. However Baker et al. [188] questioned the extent of this reduction due to solely geometric arguments. In a recent study by Harton et al. [3], the self-consistent mean-field theory of Scheutjens and Fleer and experiments were employed for particles larger than the polymer Kuhn-length. It

was shown that thickness of the polymer bound layer for the particles of radius equivalent to the polymer Kuhn-length decreases by approximately a factor of 2 relative to planar surfaces. Such findings unquestionably establish a decrease of the adsorbed layer. Still the scaling law for these effects, specifically for the particle sizes smaller than the polymer Kuhn segment length, is unclear as intrinsic polymer stiffness becomes important at such length scales.

Daoulas et al. employed self-consistent-field calculations for the worm-like chain models incorporating local stiffness to provide a better description of adsorption of PE molecules [190]. For particles in solutions, Ganesan et al. demonstrated the dependence of equilibrium characteristics on persistence length and correlation length both, provided the second is comparable to the first [191]. It was noted that scaling laws governing the concentration and radii dependence of the depletion layer thicknesses are nontrivial in nature. The worm-like chain model supports the effects of changes in rigidity upon interfacial layers and resulting barrier properties of the nanocomposites material [14]. Polymers with higher rigidity showed dominant interfacial effect leading to an enhancement in free volume, which resulted in increased penetrant diffusivities for all filler concentrations.

Linse and Kallrot have shown the effect of polymer flexibility on the adsorption of homopolymers from a solution onto a flat surface [192]. It was demonstrated that rod-like polymers ehxibit single adsorbed layer, whereas flexible polymers adsorb in two layers. An increase in the polymer-surface attraction lead to flatter polymer conformation with increased number of adsorbed beads. In this chapter, such phenomena in polymer melts are probed with the help of simulations. New MC methods capable of addressing conformational characteristics of long macromolecules in atomistic detail are designed and applied. It is shown that due to intrinsic stiffness at local length-scales, decreasing the particle size has a profound impact as polymer chains form an increased number of shorter contacts that

favor planar configurations of train segments. The findings in this chapter highlight the role of local rigidity on the scaling of bound layer with the particle size with implications on the properties of polymer-particle mixtures.

3.2 Models and Systems

3.2.1 Polyethylene Melt

Polyethylene is modeled as a sequence of CH_2 united atoms (UA) with terminal CH_3 beads. Non-bonded interactions between pairs of CH_2 or CH_3 are described by a pairwise-additive Lennard-Jones 12-6 potential computed as

$$u(r_{ij}) = 4\epsilon_{ij}\left[\left(\frac{\sigma_{ij}}{r_{ij}}\right)^{12} - \left(\frac{\sigma_{ij}}{r_{ij}}\right)^{6}\right], \tag{3.1}$$

where r_{ij} is separation and ϵ_{ij} and σ_{ij} are interaction parameters provided by the Transferable Potential for Phase Equilibria (TraPPE) force field given by Martin and Siepmann [193]. For CH_2, σ = 0.395 nm, ϵ = 0.382 kJ/mol and for CH_3, σ = 0.375 nm and ϵ = 0.815 kJ/mol.

Interactions between unlike atoms are calculated by Lorentz-Berthelot combination rules

$$\sigma_{ij} = \left(\frac{\sigma_{ii} + \sigma_{jj}}{2}\right), \tag{3.2}$$

$$\epsilon_{ij} = \sqrt{\epsilon_{ii}\epsilon_{jj}}. \tag{3.3}$$

Polymer intra-molecular interactions (harmonic bond, bond angle bending and torsional potential) are implemented following Nath et al. [194]. The harmonic bond potential is given by

$$\frac{V(r)}{k_{\mathsf{B}}} = \frac{K_r}{2}(r - b_{\mathsf{eq}})^2, \tag{3.4}$$

where K_r = 80,235 kJ mol^{-1} nm^{-2} and b_{eq} = 0.154 nm. The bond angle bending potential is given by

$$\frac{V(\theta)}{k_B} = \frac{K_\theta}{2}(\theta - \theta_{eq})^2, \tag{3.5}$$

where K_θ = 519.66 kJ mol^{-1} rad^{-2} and θ_{eq} = 114.0°. The torsional potential is of the form

$$\frac{V(\phi)}{k_B} = V_0 + V_1(1 + \cos\phi) + V_2(1 - \cos 2\phi) + V_3(1 + \cos 3\phi), \tag{3.6}$$

where V_0 = 0, V_1 = 355.04 K, V_2 = -68.19 K and V_3 = 701.32 K.

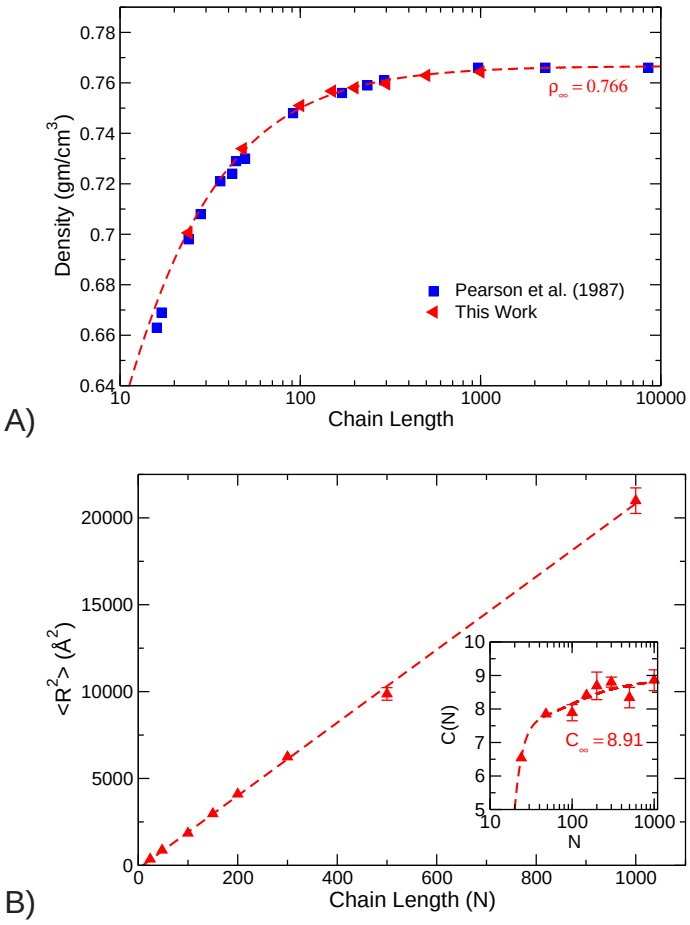

Figure 3.1: A) Comparison of predicted densities for PE melts at 450 K and 1 bar to experimental data available in literature [5]. B) End-to-end distance and characteristic ratio (inset) as a function of chain length (N, number of UA beads).

We found that incorporation of CH_3 terminal beads and flexible bond-stretching potential terms leads to excellent agreement with the thermodynamic and conformational properties mentioned in literature. For example, Figure 3.1A, presents the density as a function of chain length at 450 K temperature and 1 bar pressure which is in quantitative agreement to experimental data [5]. A hyperbolic fit,

$$\rho(N,T) = \frac{\rho_\infty(T)}{1 + \frac{a_0(T)}{N}}, \tag{3.7}$$

results to ρ_∞ = 0.766 g/cm^3 at the limit of infinite molecular weight. Figure 3.1B shows characteristic ratios calculated from average squared end-to-end distances using the equation

$$C(N) = \frac{< R^2 >}{(N-1)l^2}, \tag{3.8}$$

where l = 0.154 nm is mean CH_2-CH_x (x = 2, 3) bond length. Using the expression [195]

$$C(N) = C_\infty + \frac{a_1}{(N-1)} + \frac{a_2}{(N-2)} + \frac{a_3}{(N-3)}, \tag{3.9}$$

a value C_∞ = 8.91 is obtained, which is in the range 8.7 to 10.5 determined by experiments [196] at 400 K.

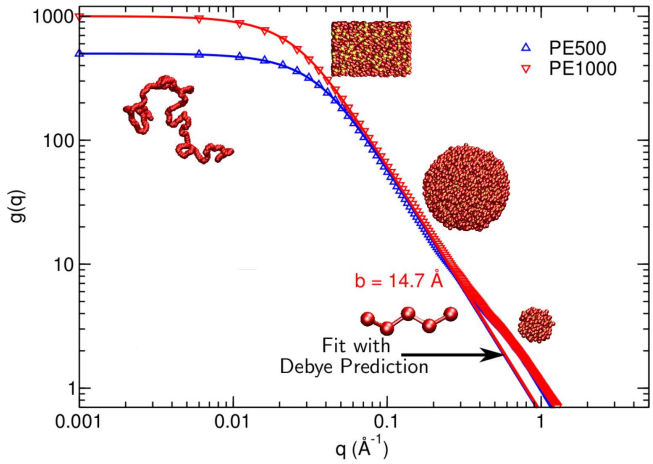

Figure 3.2: Static single chain structure factor for PE500 and PE1000 (symbols) and fit with Debye function (solid lines) with an estimate of the Kuhn length.

Finally, results for the static single chain (intra-molecular) structure factor were obtained as described in the literature [197]. For a polymer chain consisting of N diffraction centers located at the backbone carbon positions, the static single chain structure factor is given by

$$g(q) = \frac{1}{N} \sum_{i=1}^{N} \sum_{j=1}^{N} \frac{\sin qr_{ij}}{qr_{ij}}, \tag{3.10}$$

where q is the scattering vector. Figure 3.2 provides this property for polyethylene (PE) chains of N = 500 (PE500) and N = 1000 (PE1000) at 450K and 1 atm. The chain form factor $P(q) = g(q)/g_0$ can be fitted using the Debye function [198], which describes the polymer chains as a sequence of independent Gaussian segments up to vanishing length scales. A fit using the Debye function

$$P(q) = \frac{2}{x^2}(x - 1 + \exp(-x)), \tag{3.11}$$

with

$$x = q^2 R_g^{0\,2} = q^2 \frac{bL}{6}, \tag{3.12}$$

where R_g^0 is polymer radius of gyration, L is polymer contour length and b is the Kuhn length, leads to an estimate of b = 1.47 nm with R_g^0 = 5.62 nm for PE1000 chains. It is important to note that for small values of the scattering vector q (larger length scales) the Gaussian coil provides a satisfactory description, but this is not true for length scales ($\approx b$) where local stiffness plays a significant role.

3.2.2 Fullerenes

For fullerene, Lennard-Jones interactions are used as σ_C = 0.347 nm and ϵ_C = 0.275 kJ/mol [199]. As in all our models, Lennard-Jones interactions are excluded between atoms interacting through intra-molecular terms. For fullerene,

Table 3.1: Force field parameters for silica according to the BKS force field [9].

i-j	A_{ij} (kJ/mol)	b_{ij} (nm^{-1})	c_{ij} (kJ mol^{-1} nm^6)	Atomic Charges
O-O	133,996	27.6000	0.016885	q_O = -1.2
Si-O	1,737,099	48.7318	0.012884	q_{Si} = 2.4

a Morse bond potential, a harmonic cosine of the bending angle, and a 2-fold torsion potential were used, which have a functional form of

$$U(r_{ij}, \theta_{ijk}, \phi_{ijkl}) = K_{Cr}(\xi_{ij} - 1)^2 + \frac{1}{2}K_{C\theta}(\cos\theta_{ijk} - \cos\theta_C)^2 + \frac{1}{2}K_{C\phi}(1 - \cos 2\phi_{ijkl}), \tag{3.13}$$

where

$$\xi_{ij} = e^{-\gamma(r_{ij} - r_C)}. \tag{3.14}$$

Here r_{ij}, θ_{ijk} and ϕ_{ijkl} represent distance, bond angles and torsion angles between bonded atoms. K_{Cr} = 478.9 kJ/mol, r_C = 0.1418 nm , γ = 21.867 nm^{-1}, $K_{C\theta}$ = 562.2 kJ/mol, θ_C = 120° are taken from the work of Guo et al. [200]. and $K_{C\phi}$ = 25.12 kJ/mol following Walther et al. [201].

3.2.3 Silica Nanoparticles

Silica nanoparticles are represented using fully flexible atomistic models. van Beest et al. [9] proposed the BKS model for interatomic potential of the form

$$\phi_{ij} = \frac{q_i q_j}{r_{ij}} + A_{ij}\exp(-b_{ij}r_{ij}) - \frac{c_{ij}}{r_{ij}^6}, \tag{3.15}$$

which involves a coulomb term and a covalent contribution in the usual Buckingham form. Parameters proposed in the BKS model are listed in Table 3.1.

The BKS potential suffers with unphysical behavior of divergence to -∞ for very small separation of Si-O atoms. In order to reach these small separations,

Table 3.2: Parameters for correcting unphysical behavior of BKS force field [10]

.

i-j	σ_{ij} (nm)	ϵ_{ij} (kJ/mol)
Si-Si	0.0	0.0
Si-O	0.1313635	0.299
O-O	0.1779239	0.101

Si-O atom pairs need to overcome a potential barrier, which is of the order of 5000 K [202]. Thus simulations at high temperature can lead to algorithmic problems. To overcome this limitation when performing simulations at high temperature, a correction term is introduced in the BKS potential as described in the literature [10]. The corrected potential includes a 30-6 term and is formulated as

$$\phi_{ij} = \phi_{ij}^{\text{BKS}} + 4\epsilon_{ij}\left[\left(\frac{\sigma_{ij}}{r_{ij}}\right)^{30} - \left(\frac{\sigma_{ij}}{r_{ij}}\right)^{6}\right], \tag{3.16}$$

where ϕ_{ij}^{BKS} is the original BKS potential given by Eq. 3.15. Parameters used in correction term are listed in Table 3.2.

This modified BKS potential was used for creating structures of amorphous silica by simulated annealing. For our main MC simulations at low temperature (450K), the BKS was replaced by Lennard-Jones interactions together with bond and angle potentials between neighboring Si and O atoms (as in the literature [33]). We derived a set of parameters k_b and k_θ, which gives a distribution of bond lengths and angles very close to that obtained from modified BKS potential (Figure 3.3).

The harmonic bond potential for Si-O bonds is given by

$$\phi_r(r_{ij}) = \frac{k_\ell}{2}(r_{ij} - r_{\text{o}})^2, \tag{3.17}$$

where k_ℓ=242,000 kJ/mol-nm^2 and r_{o}=0.1608 nm. The angle bending potential is

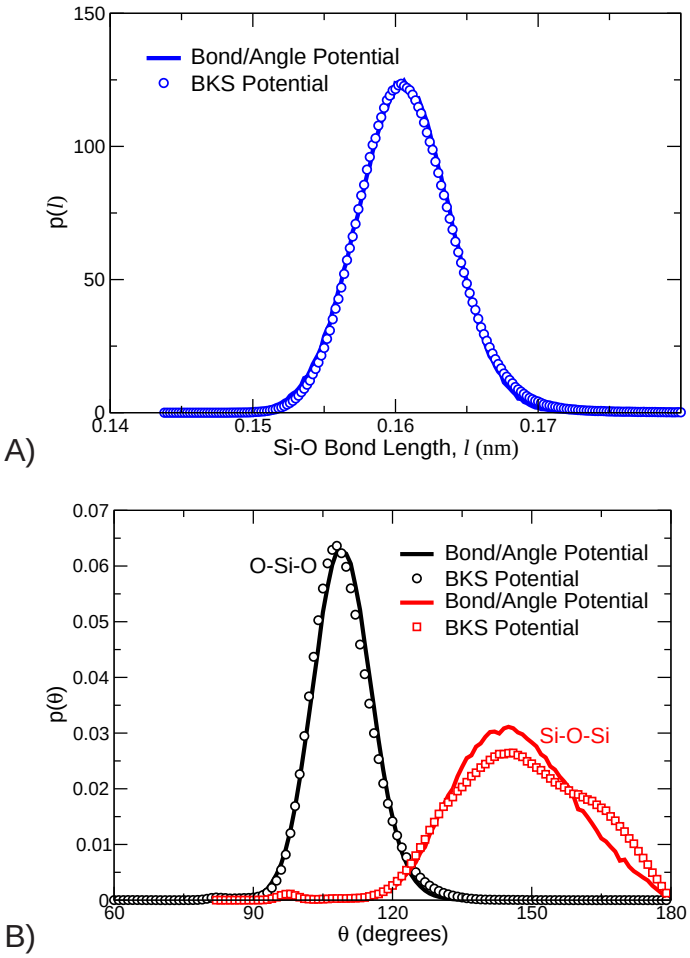

Figure 3.3: Comparison of A) Si-O bond lengths distribution and B) Si-O-Si and O-Si-O angles distributions as obtained from the BKS model and bond-angle potentials.

formulated as

$$\phi_\theta(\theta) = \frac{k_\theta}{2}(\cos(\theta) - \cos(\theta_o))^2, \tag{3.18}$$

where k_θ = 140.0 kJ/mol and θ_o = 167.5° for Si-O-Si angle and k_θ = 235.0 kJ/mol and θ_o = 109.3° for O-Si-O angle. For Lennard-Jones interactions, Si atoms are omitted owing to their small size and polarizability (σ_{Si} = ϵ_{Si}/k_B = 0.0). For O atoms a σ_O = 0.27 nm and ϵ_O/k_B = 1.913 kJ/mol was used [203].

Preparation of Silica Nanoparticles

A methodology involving a melt-quenching process for preparing amorphous silica given by Vollmayr et al. [202] is used as a precursor to nanoparticle preparation. In this method, the α-quartz unit cell was taken as initial structure. A super cell of 5 $\times$ 5 $\times$ 5 unit cells containing 1125 atoms was equilibrated at 300K temperature and 1 bar pressure for 200 ps with a time step of 1 fs using the molecular dynamics (MD) program Gromacs [204]. For the MD equilibration, the modified BKS potential (Eq. 3.16) was used. The cut-off distance was 0.9 nm for Lennard Jones interactions and 0.8 nm for electrostatic interactions. The Particle Mesh Ewald (PME) method of order 4 was applied for calculating electrostatic contributions. Long range corrections for energy and pressure were also taken into account. The temperature was successively increased to 1000 K, 2000 K, 3000K and 4000 K. At each temperature, an equilibrated structure was obtained, which served as initial structure for successive equilibration at a higher temperature. The equilibrated molten silica at 4000 K temperature and 1 bar pressure was then quenched by using the simulated annealing protocol of Gromacs [204] to 100 K at a rate of -10 K ps^{-1} to obtain solid amorphous silica. This amorphous silica structure was replicated for constructing a 3 $\times$ 3 $\times$ 3 super cell containing 30375 atoms. Atomistic configurations and topologies of silica nanoparticles of 1.0 nm, 1.5 nm, 2.0 nm, 2.5 nm and 3.0 nm radius and slabs of approximately 3.2 nm width were prepared by following a process similar to Brown et al. [33]. Preparation of a silica nanoparticle with nominal radius R_n or a slab with half-width W_h involves the following steps:

1. Read the bulk configuration of amorphous silica obtained from the melt-quench process.

2. Define the point of intersection of diagonals of super cell as the center of cell. For nanoparticle, discard all Si atoms at a distance beyond R_n and all O

atoms beyond R_n + 0.2 nm from the center. For slab, discard all Si atoms at a distance (along z-axis) beyond $W_h/2$ and all O atoms beyond ($W_h/2$) + 0.2 nm from the center of cell.

3. Define all atoms at a distance more than r_n from the center of cell as surface layer atoms for nanoparticle. For slab, define all atoms with distance (along z-axis) from the center of cell more than r_n as surface layer atoms. In previous studies, [33] a value r_n = 0.9 nm was used.

4. Define all O atoms within 0.19 nm from Si atoms as neighboring oxygens. Minimum image convention is used while calculating the distances for slab in order to maintain continuity of structure in x-y plane. Discard all Si atoms in the surface layer with less than 4 neighboring oxygens.

5. Find out Si atoms within 0.19 nm from O atoms as neighboring silicons.

6. Discard all O atoms in surface layer without neighboring silicons.

7. Label O atoms with just one neighboring silicon as nonbridging oxygen. Update connectivity table by adding a bond for both atoms.

8. Label Si atoms with a nonbridging oxygen neighbor as surface silicon.

9. Visit all surface silicons and change neighboring oxygens labeled as nonbridging oxygens to bridging oxygens. Update connectivity table by adding a bond between surface silicons and neighboring bridging oxygens.

10. Loop over all the bridging oxygens and find all neighboring nonsurface silicons with a distance (actual distance for nanoparticles and distance along z-axis for slab) more than r_n distance from the center of cell. Label the silicons as surface silicons. Update the connectivity table.

11. If number of nonbridging oxygens added at Step 8 or number of surface silicons added at Step 9 is nonzero, go to Step 8.

12. Label bridging oxygens with less than two neighboring surface silicons as regular core oxygen. Keep the connectivity table unchanged.

13. Update the connectivity tables by indicating bonds between the core silicons and their neighboring oxygen atoms (within a distance of 0.19 nm).

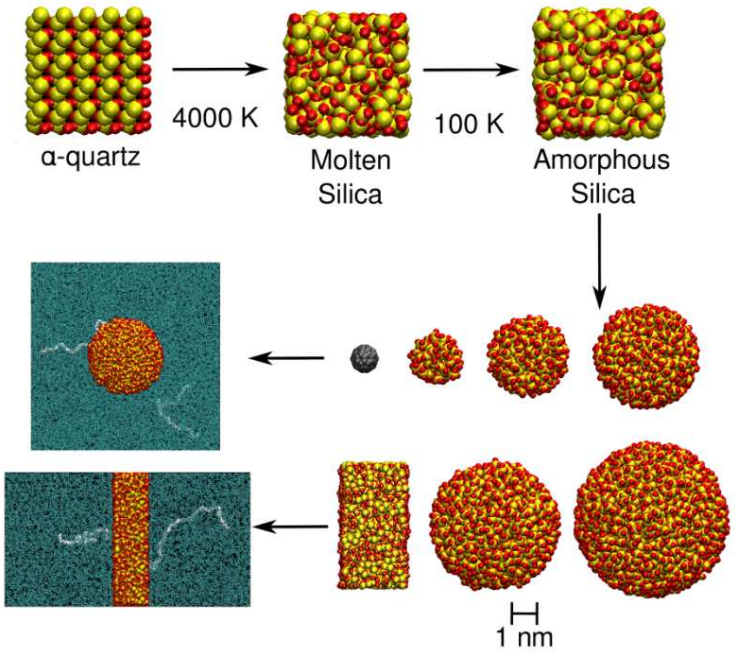

Figure 3.4: Schematics illustrating the construction of silica nanoparticles and their insertion into polymer matrix.

The use of the above method for constructing nanoparticles results to highly asymmetric non-spherical shapes for particles with a radius less than 1 nm which provided a motivation to include fullerenes (C_{60}) as nearly spherical nanoparticles at sub-nanometer size for this study. Figure 3.4 represents the schematics of the preparation of nanoparticles and their subsequent insertion into a polymer matrix. It should be noted that certain surface roughness exists in these models of nanoparticles as expected in any chemically synthesized nanoparticle. Keeping

this in mind, an explicit determination of size and area was performed for each of the constructed nanoparticle.

Assessment of surface area and volume of silica nanoparticles

A method for determining the surface area and volume of molecular assemblies provided by Eisenhaber et al. [205] as implemented in the Gromacs [204] tool g_sas was used. In Gromacs parameter files, the radii of Si, O and C atoms were set to half of the collision diameters (σ), which is equivalent to 0.0 nm for Si, 0.135 nm for O atoms and 0.1735 nm for C atoms. Using a probe of radius 0.1975 nm (half of the σ for CH_2 UA) polymer accessible surface areas and volumes were calculated as listed in Table 3.3. It is emphasized that small fluctuations are expected due to flexibility of particle models. Effective radii of nanoparticles (R_{eff}) were calculated as the radius of sphere with volume equal to polymer accessible volume of nanoparticle, further corrected by half of the σ for CH_2 UA (Table 3.3).

Table 3.3: Abbreviations and calculated polymer accessible surface areas (A), volumes (V), effective radii of nanoparticles (R_{eff}), ratio of R_{eff} to bulk polymer Kuhn segment length b and enthalpic interactions with a single CH_2 probe (well depth, ε_0). Reproduced from Ref. 6, Copyright 2012, American Institute of Physics.

Particle (Abbrev.)	A(nm^2)	V(nm^3)	R_{eff}(nm)	R_{eff}/b	ε_0 (kJ/mol)
C_{60}	7.12	1.66	0.54	0.37	-2.40
Silica (SIL-1.0)	25.71	8.66	1.08	0.73	-0.85
Silica (SIL-1.5)	53.43	24.71	1.61	1.09	-0.55
Silica (SIL-2.0)	89.79	51.91	2.12	1.44	-0.72
Silica (SIL-2.5)	130.95	92.62	2.61	1.77	-1.09
Silica (SIL-3.0)	184.30	152.51	3.12	2.12	-0.99
Silica (Slab)					-0.92

Enthalpic Interactions of Nanoparticles with Polymer Probe Particle

It is important to characterize the strength of enthalpic interactions between the polymer and different nanoparticles. A method implementing random probe insertion technique, which is a modification of the method used by Brown et al. [33] for calculating polymer accessible volume was used for this purpose. A probe of size equivalent to CH_2 was placed at large number of random trial positions and the potential energy of the probe particle was calculated with all the nanoparticle atoms as per Eq. 3.1 to construct smooth potential curves. The well depth ϵ_0 obtained from these plots is listed in Table 3.3. It can be observed that the silica slab and nanoparticles with larger radii (R_n = 2.5 nm and 3.0 nm) have almost similar enthalpic interactions with the probe. The smaller nanoparticles present a slight decrease in the well depth. An increase for R_n = 1.0 nm is due to somewhat larger surface density of interaction sites (O atoms). The fullerene C_{60} shows significantly stronger enthalpic interactions as compared to any of the silica nanoparticles due to the larger density of interaction sites on the surface of this nanoparticle.

3.2.4 Systems Studied

Particles were inserted into equilibrated polymer melt configurations by first introducing a cavity using a repulsive potential. To avoid finite-size effects the edge-length of each simulation cell was on average $\sim$ 6.5 $\times R_g^0$ of bulk polymer plus the diameter of respective nanoparticle. For slabs, dimensions along the normal to the surface were $\sim$ 8 $\times R_g^0$. These requirements lead to very large system sizes (Table 3.4). Keeping the computational feasibility in mind, flat surfaces with polymer chain lengths up to N = 500 were considered, whereas particles were studied for lengths $N \leq$ 200. C_{60} was the only particle studied with N = 300.

Table 3.4: Systems studied, ratio of $R_{\text{eff}}/R_{\text{g}}^0$, number of chains ($n_{\text{chains}}$), total number of atoms (n_{atoms}) and average dimensions of the simulation box. Reproduced from Ref. 6, Copyright 2012, American Institute of Physics.

System	N	$R_{\text{eff}}/R_{\text{g}}^0$	n_{chains}	n_{atoms}	L (nm)		
PE48-C60	48	0.49	300	14,460	7.71		
PE100-C60	100	0.32	492	49,260	11.52		
PE150-C60	150	0.25	746	111,960	15.11		
PE200-C60	200	0.21	906	181,260	17.75		
PE300-C60	300	0.17	1080	324,060	21.49		
PE48-SIL-1.0	48	0.99	532	25,876	9.36		
PE100-SIL-1.0	100	0.64	734	73,740	13.19		
PE150-SIL-1.0	150	0.50	1020	153,340	16.79		
PE200-SIL-1.0	200	0.43	1184	237,140	19.40		
PE48-SIL-1.5	48	1.48	726	36,005	10.41		
PE100-SIL-1.5	100	0.96	922	93,357	14.23		
PE150-SIL-1.5	150	0.74	1224	184,757	17.85		
PE200-SIL-1.5	200	0.64	1390	279,157	20.46		
PE48-SIL-2.0	48	1.94	944	47,966	11.40		
PE100-SIL-2.0	100	1.26	1128	115,454	15.25		
PE150-SIL-2.0	150	0.98	1440	218,654	18.87		
PE200-SIL-2.0	200	0.85	1602	323,054	21.48		
PE48-SIL-2.5	48	2.39	1196	62,479	12.38		
PE100-SIL-2.5	100	1.55	1354	140,471	16.24		
PE150-SIL-2.5	150	1.20	1674	256,171	19.87		
PE48-SIL-3.0	48	2.86	1488	80,105	13.39		
PE100-SIL-3.0	100	1.86	1610	169,681	17.25		
PE150-SIL-3.0	150	1.44	1934	298,781	20.87		
					l_z	l_x	l_y
PE48-Slab	48		122	10,982	12.23	4.42	4.68
PE100-Slab	100		152	23,896	16.68	5.90	5.96
PE150-Slab	150		250	53,217	21.37	7.86	8.08
PE200-Slab	200		220	59,717	25.19	7.86	8.08
PE300-Slab	300		234	90,600	29.17	8.84	9.36
PE500-Slab	500		302	185,653	36.07	11.79	11.91

3.2.5 Initial Configurations

Equilibrated polymer melt configurations were used as the initial configuration with particular attention towards avoiding finite-system size effects. Insertion of

nanoparticles was performed by placing a fictitious interaction site at the center of the box with a very high repulsive potential to create a cavity:

$$V(r) = V_o \left[1 - \tanh\left(\frac{r - R_c}{\delta}\right)\right], \tag{3.19}$$

where V_o is strength of the potential, R_c is the radius of the cavity and δ is the layer width, over which the repulsive potential drops to zero. In this work, these parameters were set to V_o = 50000 kJ/mol and δ = 0.1 nm. Values of R_c were gradually increased from zero to a value slightly greater than the nanoparticle radius so that the cavity created could accommodate the nanoparticle without creating overlaps with the surrounding polymer.

A different method was applied for preparing polymer-silica slab systems. Cubic simulation boxes with edge-lengths fitting with the $x - y$ surface of slab were prepared. These boxes were replicated along the z-axis in order to obtain a simulation box of desired length along z-axis. The slab was then introduced at one end of the simulation box and box length along z-axis was adjusted in order to remove the overlaps between the polymer and silica atoms. Coordinates of atoms in the simulation box were translated along z-axis in order to place slab at the center of the box. The systems containing silica nanoparticles and fullerene and Slabs in polymer matrix were further equilibrated by performing MD NPT simulations at 1 bar pressure and 450 K temperature and subsequent long MC simulations with our algorithms.

3.3 Simulation Methodology

For all the systems listed in Table 3.4, NPT MC simulations were performed at 450K temperature and 1 bar pressure. Interatomic potentials were smoothly

switched to zero between 1.2 nm and 1.3 nm by using a switch function as in the free simulation software Gromacs [204]. Two snapshots in the Figure 3.5 represent two systems studied (PE500-Slab and PE200-SIL-2.0) and demonstrate the challenges encountered during modeling such systems. Polymer molecules in contact with the surface are identified using a 0.6 Å distance criterion from any atom of the nanoparticle or surface [182]. These systems are highly heterogeneous, which can be readily observed. As discussed in later sections in more detail, the first layer consists of loop and train segments followed by a second regime dominated by tail segments interacting with the bulk polymer melt. In order to achieve reasonable equilibration, adequate sampling in both of the aforementioned domains is essential.

The simulations included global update moves such as standard hybrid NVE molecular dynamics (MD) and volume fluctuations (implemented only along z-axis for the slab systems). Due to the large system sizes, maintaining finite acceptance of the hybrid NVE MD move (acceptance criteria considering change of the total Hamiltonian) requires small timesteps (500 steps of $\approx$ 0.5 fs each for each hybrid NVE MD move, $\approx$ 30,000 moves accepted for each simulation). The hybrid NVE MD moves account for significant computational cost, nevertheless the moves were kept in the mix of MC moves to facilitate adequately sampling of the fluctuations of atoms of the solid surface or the nanoparticle (along with other moves e.g. a simple MC displacement for the center of mass, COM, of the slab or particle). 0.01% for hybrid NVE MD moves and 0.1% attempts for volume changes were allocated in the mix of moves.

MC moves extensively applied in past studies e.g. configurational bias (CB) reptation, CB rearrangement of chain ends and rebridging CB of inner sections [66, 69] formed the second set of moves. These moves first select a chain and then an inner segment or end of this polymer chain to rebuild. For the large systems

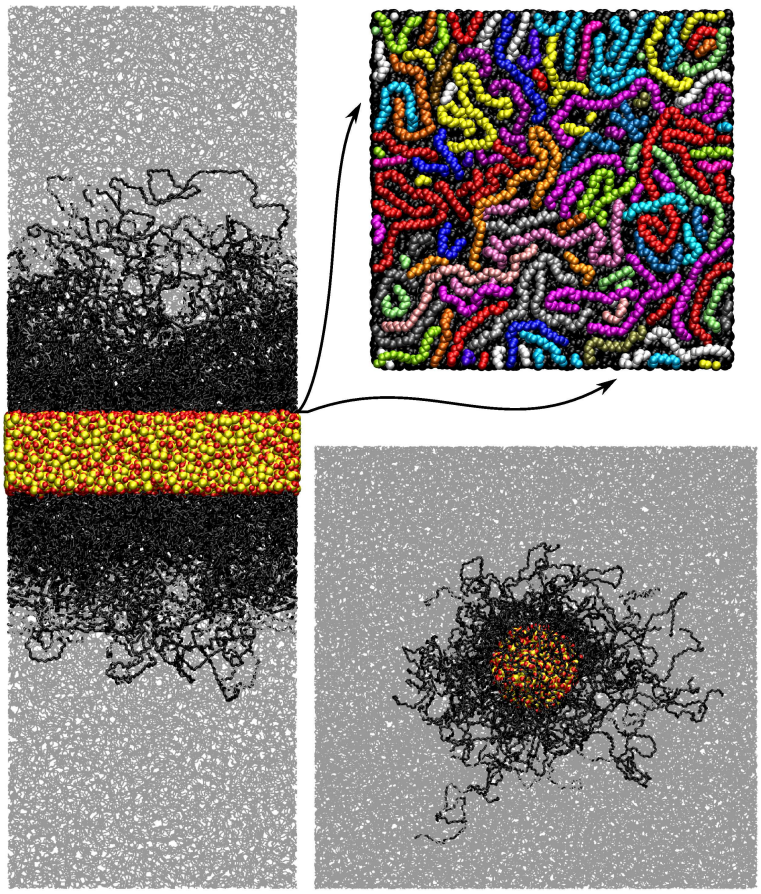

Figure 3.5: Snapshots of systems showing polymer molecules in contact with the surface explicitly in black. The train segments belonging to different chains are depicted for a flat surface in the right upper snapshot. Reproduced from Ref. 6, Copyright 2012, American Institute of Physics.

considered, chains in contact with the surface are only a fraction of the polymer melt. For example, the PE500-Slab system has approximately 23% of the chain molecules in contact with the surface, whereas for the PE200-SIL-2.0 system this population drops to just 3.5% of the total polymer chains ($\approx$ 54 out of 1602 chains). These numbers indicate the need to enhance sampling in proximity of the surface by selecting chain molecules more often. This was accomplished for the second set of moves by selecting polymer chains based on the distance R_{CM}(chain) of the

chain COM from the surface of the slab or the nanoparticle according to

$$\mathcal{P}^{\text{sel}}(\text{chain}) = \frac{1}{2}A_0\left(1 - \tanh\left(\frac{R_{\text{CM}}(\text{chain}) - R_g^0}{R_g^0}\right)\right) + (1 - A_0), \tag{3.20}$$

where the constant A_0 was set to 0.75. R_{g}^0 is the average radius of gyration of the polymer in the bulk. For selecting a chain molecule, normalization of the calculated $\mathcal{P}^{\text{sel}}$(chain) with the sum of similar probabilities for all the chains leads to $\mathcal{P}_{\text{norm}}^{\text{sel}}$(chain). A prefactor to the regular acceptance criterion of the move, equal to the ratio of $\mathcal{P}_{\text{norm}}^{\text{sel, new}}(\text{chain})/\mathcal{P}_{\text{norm}}^{\text{sel, old}}(\text{chain})$ was introduced to maintain detail balance. A power-law prefactor of $1/R_{\text{COM-COM}}^2$ using the separation of chain COM to particle COM to account for the three-dimensional increase in the number of chains was introduced for the nanoparticles. In principle, any functional from can be used for preferential sampling, however it was shown in previous works [184, 206] that a rapidly decaying power law is not necessarily the most efficient. Furthermore, in current study the layer was scaled with R_{g}^0 due to the increased polymer size of longer chain molecules. Maintaining an unnormalized probability for each chain and the sum of these probabilities for all chains, followed by updating them upon acceptance of any MC move obviously does not add any significant computational cost.

Sampling of the spatial extent of loops and tails is accomplished by the connectivity-altering double-bridging moves with an implementation following the algorithm of Banaszak and de Pablo [69]. The double-bridging technique allows construction of bridges of variable number of bonds (from 4-6 bonds or 3-5 atoms), which increases candidate pairs and reduces the shuttling effect. A biased selection of two pairs (i.e. (i, j) and (i + 6, j - 6) for bridges of 5 atoms) along two chains

$ichain$ and $jchain$ respectively is performed as:

$$\mathcal{P}(\text{pairs}) = \frac{P_1(i \xrightarrow{\text{bridge to}} j) \times P_2(i+6 \xrightarrow{\text{bridge to}} j-6)}{Z}, \tag{3.21}$$

where i and j are selected appropriately to maintain monodispersity (Z is a normalization constant). The intra-molecular probabilities denoted by $P()$'s are either pre-computed or calculated "on-the-fly" [66, 207]. In the systems studied, a large number of bridging pairs with significant probability exist, but only a few out of these pairs are in proximity to the surface. For example, in the PE200-SIL-2.0 system representative numbers are found to be $\approx$ 6,500 for bridging with 4 bonds, $\approx$ 17,500 for 5 bonds and $\approx$ 30,000 for 6 bonds. Eq. 3.21 coupled with Eq. 3.20 maximizes sampling in the vicinity of the surface and renders a $\mathcal{P}^{\text{sel}}(\text{pairs})$ based on the COM of the four beads serving as starting and ending points of bridges (shown in Figure 3.6A). While these beads at start and end points are not displaced by the construction of new bridges, still probabilities have to be recalculated for the proposed move and introduced in the acceptance criterion considering the fact that normalization factor is altered due to new positions of the bridging atoms.

It was found that with the moves described up to this point, it remains challenging to sample distributions of number of beads participating in formation of tail, train and loop segments. Therefore a new reptate move was designed with the motivation of transferring beads directly from/to within any part of the chain by taking advantage of the increased free volume at the chain ends [208]. Specifically, CB growing/shrinking of inner segments was coupled with a parallel shrinking/growing of a selected chain end to maintain the total chain length constant. Conceptually this move is simple, but in practice, for any model with stiffness the acceptance rate by random selection of the inner segment remains exceedingly small. In order to overcome this limitation, the pairs that bound the inner segment

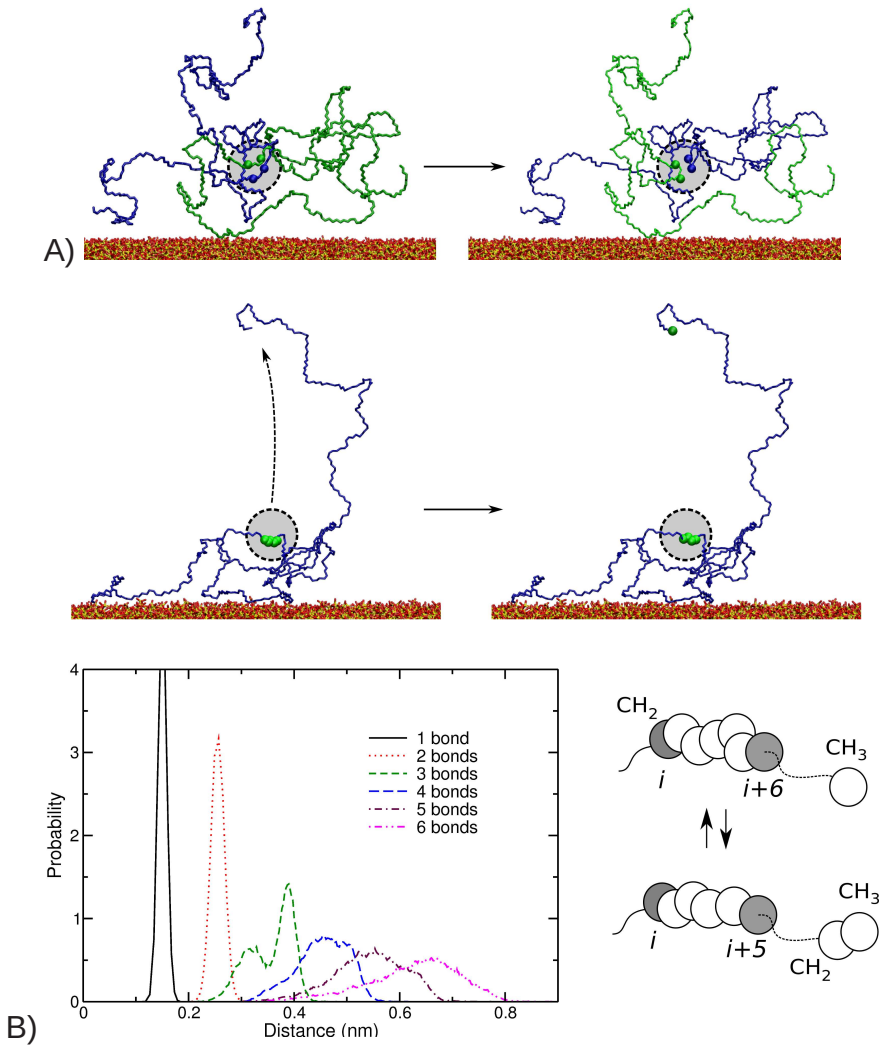

Figure 3.6: A) Double-bridging pairs are preferentially selected based on the COM of four atoms serving as start and end points. B) Schematics of shrinking/growing of inner segment coupled with a growing/shrinking of randomly selected end. Within a pre-selected chain, the probability to select a pair that bounds the segment to be regrown depends on the separation between these atoms (shaded) that remain at the same position during this move. Reproduced from Ref. 6, Copyright 2012, American Institute of Physics.

to be regrown/shrunken were selected in a bias scheme using the intra-molecular probabilities [66, 69] employed in Eq. 3.21 in addition to the bias introduced for the selection of a chain (according to Eq. 3.20). According to this algorithm, shrinking of an inner segment was biased between a pair of atoms located at positions

i and i + 6 along the chain provided their separation has a significant probability P(5 bonds) as compared to all potential pairs available within the same chain. Following a similar scheme, growing a segment of 6 bonds between two atoms previously separated by 5 bonds was biased towards the pairs that had a significant probability P(6 bonds). This move was restricted to regrowing/shrinking of 5→6 (or 6→5) bonds which requires rebuilding of 5 (4) inner atoms and 1 (2) randomly selected tail atom(s). An attempt to rebuild larger segments reduces the probability of acceptance originating from the unfavorable interactions with intermolecular neighbors. On the other hand for smaller segments, separations between bounding pairs fail to simultaneously satisfy the intramolecular structure as shown by the probabilities $P()$'s [66] depicted in Figure 3.6B, which requires significant overlap between $P()$'s for both the initial and proposed configuration.

For maintaining detail balance, normalization with the sum of probabilities over all potential pairs within the same chain for the forward move, calculation of the normalized probability to select the pair for the reverse move and introduction of the corresponding fraction as a prefactor to the overall acceptance criterion is required. Despite these efforts, the acceptance rate remained as low as 0.85%, however several advantages were observed even at such low acceptance. First, the sampling of distribution of beads in tail, train and loop segments was enhanced significantly; i.e., stretched train segments of 5 bonds are often replaced with longer segments of 6 bonds that can form loop segments. Second, a refreshment of the double-bridging lists (due to changes of indexes within a chain) enhanced the connectivity-altering simulations [67, 176, 177]. Third, this move enabled transfer of segments directly from the surface to the tails extending towards bulk polymer (Figure 3.6B) that can be subsequently subjected to double-bridging with the bulk polymer chains providing means to adsorb-desorb atoms without the limitations imposed by polymer connectivity.

3.4 Results and Discussion

3.4.1 Equilibration and Sampling

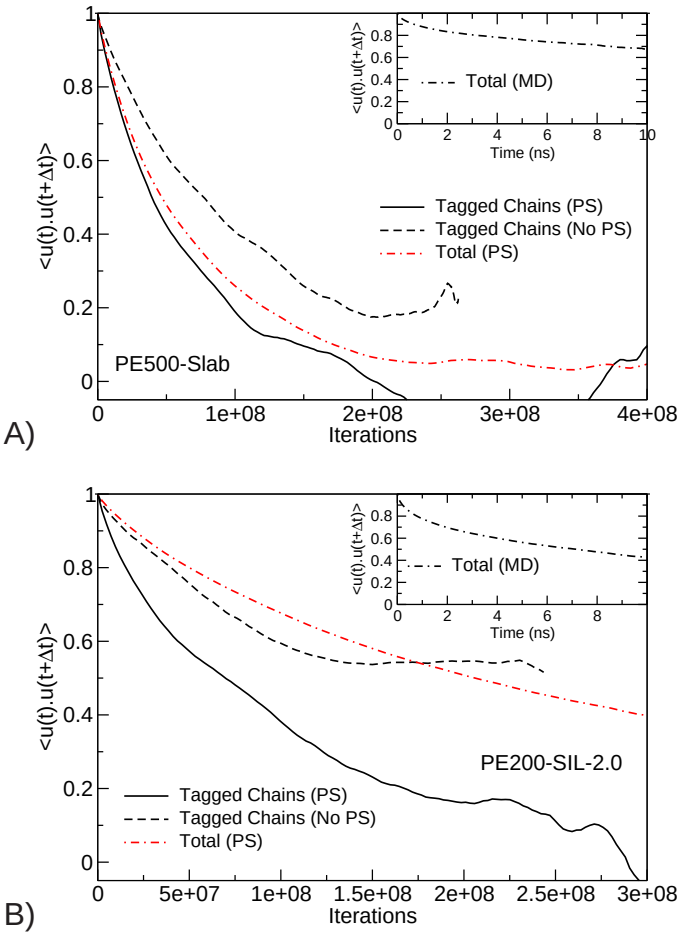

Figure 3.7: Orientation autocorrelation function of unit vector along the chain end-to-end vector shown for the selected systems, A) PE500-Slab and B) PE200-SIL-2.0, for all chains and the molecules that remain in contact with the surface ("tagged chains"). Reproduced from Ref. 6, Copyright 2012, American Institute of Physics.

The equilibration of the systems can quantitatively be examined by the decay of the autocorrelation function of a unit vector along the chain end-to-end vector. This approach alone can suffice for analyzing the equilibration of the bulk polymer systems. However to gain more insight into equilibration and conformational

sampling of chains on the surface, these molecules were “tagged” and their reorientation was calculated only while they maintain at least a single bead in contact (at the expense of further decrease in statistics for long intervals since chains can desorb by exchanging segments with bulk molecules).

Figure 3.7A presents the computed autocorrelation function for all chains (total) as well as for the tagged chains for the PE500-Slab system. In absence of preferential sampling, even after more than two months of simulation time on 8 processing cores, decorrelation of tagged chains was not complete. Introduction of preferential selection as described earlier, enabled satisfactory sampling of both total and tagged molecules. For the long chains, e.g., N = 500, standard MD does not provide sufficient equilibration as shown in the inset for a simulation of 10 ns (1 fs timestep, total 1 month on 8 cores) with the highly efficient parallel software Gromacs [204]. It should be noted that for shorter chains, connectivity-altering MC is not as efficient [65] and solely MD, in principle, could be preferable. Additionally, a 10 ns simulation with the extremely large systems (PE-200-SIL-2.0 $\approx$ 323,000 atoms) considered in the study required more than 1 month simulation time and even then complete decorrelation was not achieved (inset of Figure 3.7B). In contrast focusing on the chains in proximity of surface which are a very small fraction ($\approx$ 3.5%), drastic sampling of conformations with the MC method resulted in reasonable evolution of autocorrelation function for the bulk polymer (main Figure 3.7B).

The connectivity altering moves assist in sampling of disparate orientations along the end-to-end vector, but the actual algorithm translates only a few atoms belonging to the bridges built (6-10 atoms) and hence remaining moves are required to efficiently displace monomers in the system. The translation of the actual polymer monomers (irrespective of parent chains) is examined by the mean-square displacement of initially tagged segments along the normal to the surface for the

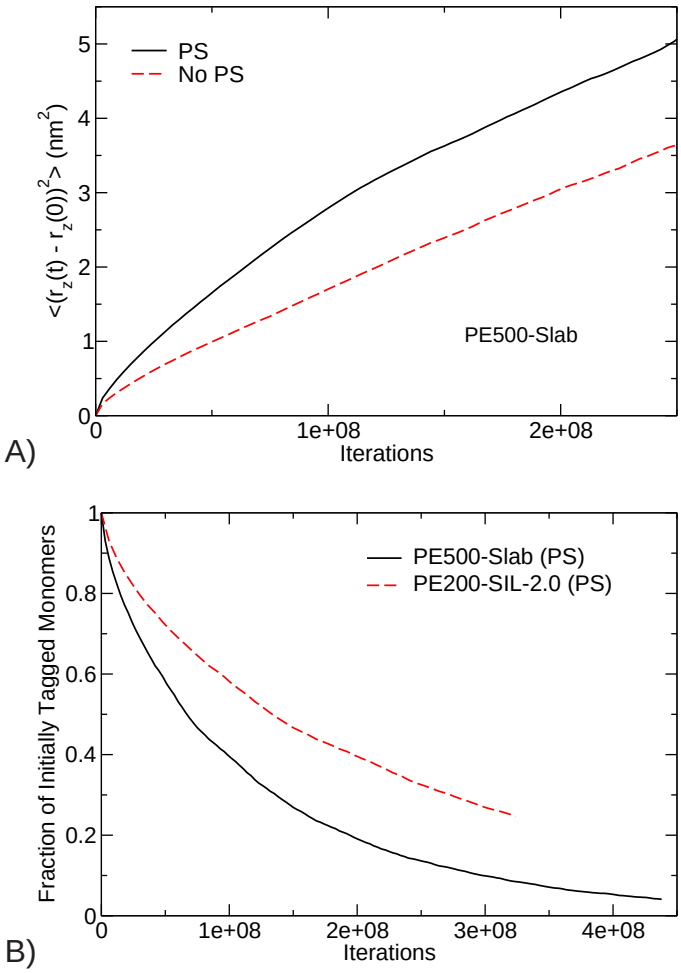

Figure 3.8: A) Mean-square displacement (MSD) normal to the surface, B) fraction of tagged monomers remaining on the surface. Reproduced from Ref. 6, Copyright 2012, American Institute of Physics.

PE500-Slab system (Figure 3.8A). It can be observed from the slope that preferential sampling induces an initial acceleration, but at the later stages the slope decreases because a large fraction of the tagged monomers will be transferred far away from the surface by then. To further expand on this and establish the efficiency of the technique to sample the phase space Figure 3.8B presents the fraction of monomers initially in contact with the surface or nanoparticle that remain tagged throughout the simulation. While some of these monomers remain in contact with the surface, they still diffuse extensively parallel to the surface as can

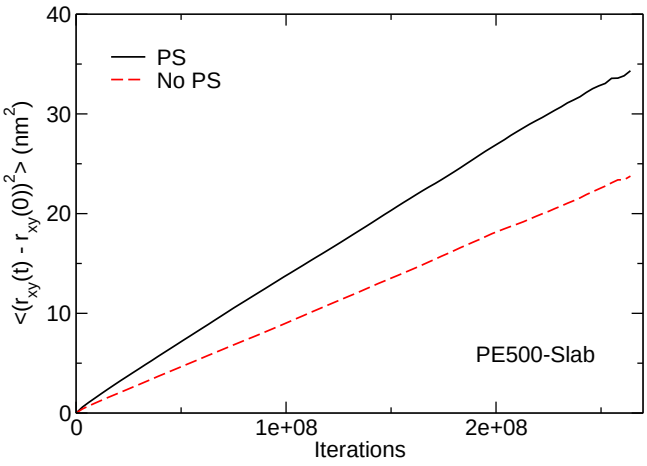

Figure 3.9: Mean-square displacement of initially tagged monomers along $x-y$ plane.

be observed from lateral mean-square displacements shown in Figure 3.9.

3.4.2 Surface Concentration

The local density of the polymer in proximity of the surface is often viewed as a measure of the strength of interactions between polymer-surface and a decrease in the first peak of radial density profiles is expected with increasing curvature [36]. The inset in Figure 3.11A demonstrates that moving from a flat surface to smaller nanoparticles indeed shows a decrease with the exception of the fullerene where a significantly higher density is observed. At first this may appear to be consistent with enthalpic interactions listed in Table 3.3. But the amplitude of the first peak in the density profiles can be misleading for estimation of effective strength of polymer-particle interactions due to the underlying assumption of the spherical symmetry, which is fairly inaccurate for the models of nanoparticles used in this study.

In order to investigate the concentration of monomers in contact with the surface further, we followed a simple distance criterion (polymer chains in contact with the surface have at least one atom within 0.6 nm from an atom of the surface) as

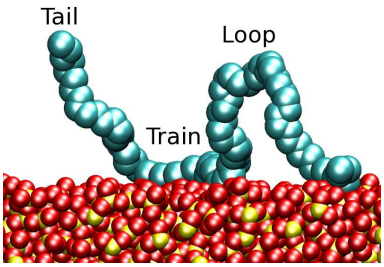

Figure 3.10: Snapshot depicting tail, train and loop segments formed by a chain in contact with the surface.

described in the study of Daoulas et al. [30] to decompose polymer segments according to the Scheutjens-Fleer theory [27] into trains, tails and loops (Figure 3.10), which are defined as following:

1. Tails are the segments which are hinged to the surface at one end while the other end is dangling freely into the bulk polymer.

2. Train segments are the consecutive monomers in contact with the surface.

3. The loop segments are constituted by the monomers in-between two train segments, which are not in contact with the surface.

Figure 3.11A demonstrates three distinct regimes for chains in contact with the surface: a first layer of monomers in contact with the surface constituting train segments, a second layer where a decay a decrease of loop segments density dominates the density profile of chains in contact while tail segment density remains constant and a third regime where tail segments extend into the bulk polymer melt. The inset of Figure 3.11A shows that the area under the first peak becomes significantly broader for the smaller particles, which is an expected outcome of the increased roughness. Using the above definitions, the number of monomers in contact with the surface can be evaluated without the approximation of spherical symmetry.

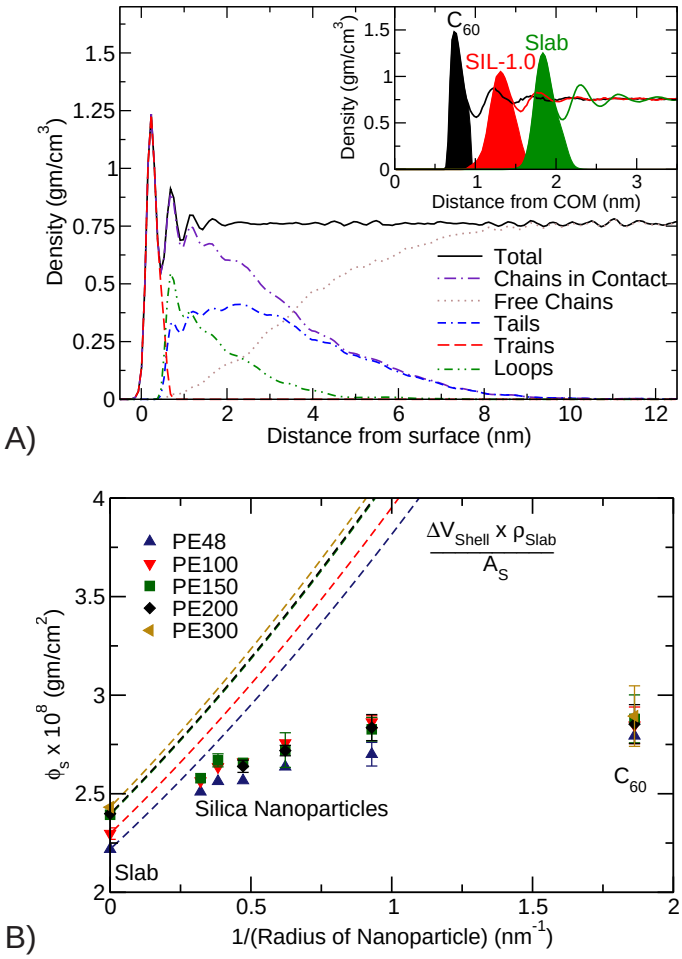

Figure 3.11: A) Density distribution for PE500-Slab as a function of distance from the surface, and decomposition to tail, train and loop segments. The inset provides profiles for selected systems. B) Surface concentration together with the predictions from geometrical arguments for ideal spherical geometry. Reproduced from Ref. 6, Copyright 2012, American Institute of Physics.

The mass of monomers in contact with the surface per unit area or surface concentration (Φ_s) is calculated by integrating the density profile of the train segments using

$$\Phi_s = \frac{\int_{R_{eff}}^{\infty} \phi_{train}(r)\, dr}{A}, \tag{3.22}$$

where, R_{eff} is radius of nanoparticle, ϕ_{train} is the density profile of the train segments and *A* is the polymer accessible surface area of the nanoparticle or surface

(Table 3.3). Before further analyzing the data extracted from such analysis, it is important to discuss the effect of particle geometry when a distance criterion is used. If the nanoparticles are hypothesized as spheres surrounded by a constant density of polymer (ρ_0) in a layer of Δr thickness and volume ΔV_{Shell} accounting for the first layer or monomers in contact, then the mass adsorbed is given by $M_s = \Delta V_{\text{Shell}} \times \rho_0$ or, $M_s = \frac{4}{3}\pi((r+\Delta r)^3 - r^3)\rho_0$ and subsequently surface concentration can be defined as

$$\Phi_s = \frac{(r+\Delta r)^3 - r^3}{3r^2}\rho_0, \tag{3.23}$$

where a constant density ρ_0 is multiplied with the ratio of the volume of a spherical shell representing first monolayer (ΔV_{Shell}) to the surface area of a sphere (A_S). Such geometric arguments suggest that under the assumption of constant polymer density independent of curvature, surface concentration should show a steep increase upon decreasing the particle radius since the volume available for the first adsorbed monolayer *per unit surface area* ($\Delta V_{\text{Shell}}/A_s$) increases significantly for smaller particle sizes (Figure 3.12).

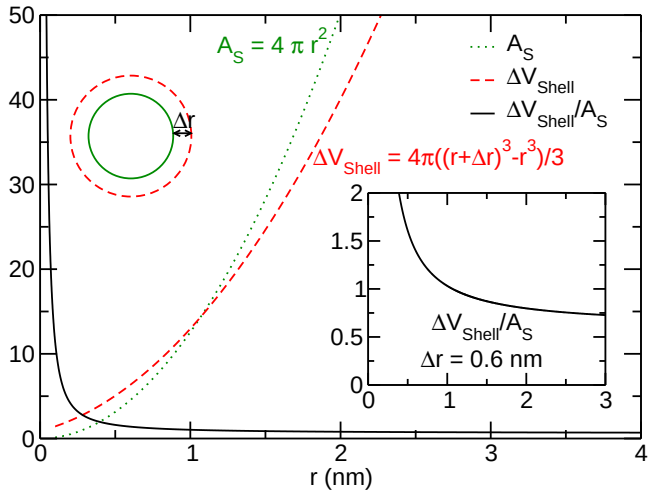

Figure 3.12: A decrease in particle radius leads to a steep increase in ($\Delta V_{\text{Shell}}/A_s$).

Using ρ_{Slab} as a reference density ($\rho_0 = \rho_{\text{Slab}}$), predictions based on geometric arguments are shown for different chain lengths by the dashed-lines in Figure 3.11B. It can be readily observed that a significant increase in surface concentration is predicted, which is in sharp contrast to calculations showing a gradual increase not at par with the predictions made by geometric arguments. These results demonstrate that the analysis provides a surprising initial increase of surface concentration with increase in curvature, which falls significantly short of anticipated values by the use of volumetric definition suggesting a decrease in effective polymer-particle interactions. It should also be noted that consideration of additional peaks (multi-layer adsorption) would further enhance this conclusion since systematic lower ordering is observed upon moving to the smaller particles. One of the striking results of this analysis is that surface concentration Φ_s for the relatively smooth C_{60} particles is actually at par with the smallest silica nanoparticles in spite of significantly higher enthalpic interactions. This observation suggests that collective properties beyond the enthalpic interactions between a single monomer and the surface listed in Table 3.3 appear to play a critical role in determining surface concentration.

To understand the molecular origin of the increase in surface concentration being lower than expected, the histograms of train segments of specific lengths similar to the work of Daoulas et al. for PE on graphite [30] are calculated. Among the systems studied, one selected profile for the PE500-Slab system is shown in Figure 3.13A which demonstrates a clear peak that corresponds roughly to a train segment of the size of one Kuhn length ($\approx$ 1.47 nm or 12 UA beads) with very low populations for the train segment lengths exceeding 50 UA beads. If the train segment length S is considered to be an order parameter for adsorption of a single train segment, the associated free energy cost will follow $-kT \ln P_{\text{tr}}(S)$. Despite the limited statistics, the logarithms of such histograms are presented in Figure 3.13A

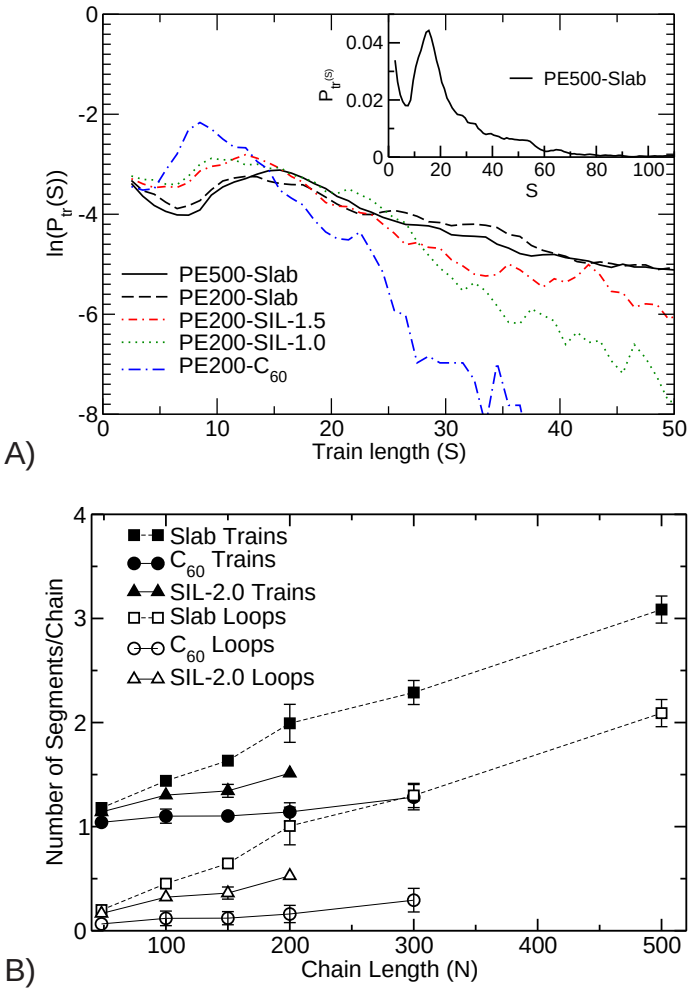

Figure 3.13: A) Probability distributions of train segment lengths for PE200 systems. B) Average numbers of train and loop segments per chain. Reproduced from Ref. 6, Copyright 2012, American Institute of Physics.

where several features become evident. No significant differences for the slab systems were observed for N > 100. The profiles show almost linear decrease beyond the maximum suggesting that addition of atoms beyond a Kuhn segment length is unfavorable due to the entropic penalty associated (free energy difference $\approx kT$ for an additional segment of length S = 50). The most interesting finding of this analysis is observed upon increasing particle curvature, where the maxima moves towards shorter segments and the probability of observing longer train segments abolishes. Furthermore, the significant changes in the slope of the decay suggests

an increased free energy penalty to augment a train segment. This finding is attributed to intramolecular interactions, which favor planar all-trans train segments hindering the formation of longer contacts on a highly curved nanoparticle surface. This critical effect for the smallest nanoparticle C_{60} seems to overcome the higher single atom-particle intermolecular interactions leading to increased populations of shorter contacts between the polymer chains and nanoparticle surface.

Following the previous discussion, it remains to be examined whether an increase in the number of shorter train segments facilitates the formation of multiple contacts within the same chain or corresponds to an increased number of polymer chains forming contacts with the surface. Figure 3.13B shows that the number of train segments per chain increases with molecular weight for the slab systems, but this is not the case for the particles even for the PE300-C_{60} system having a ratio of $R_{\text{eff}}/R_{\text{g}}^{0} \approx 0.17$. It is further demonstrated in Figure 3.14A, in the weak-adsorption limit considered here, the decrease of the average length of train segments leads to an increase in the number of chains interacting with particles with an almost linear dependence on the particle curvature.

This phenomenon can serve as a rationale behind the lower than anticipated increase in surface concentration. Train-segments on the surface (as shown in the representative snapshot in Figure 3.5) can add more atoms as intramolecular neighbors; an observation attributed to the well-established correlation hole effect, which is further demonstrated by the lateral radial distributions in Figure 3.14B. Therefore, upon increasing the particle curvature, local packing effects lead to the calculated values of surface concentration that fail to follow the anticipated scaling (Figure 3.11B) by recruiting sufficiently large number of chains in contact with the surface. To conclude, as the particle curvature increases and size decreases, more polymer chains form contacts of shorter length with the particle surface. This effect eventually alters the amount of polymer melt interacting with the surface.

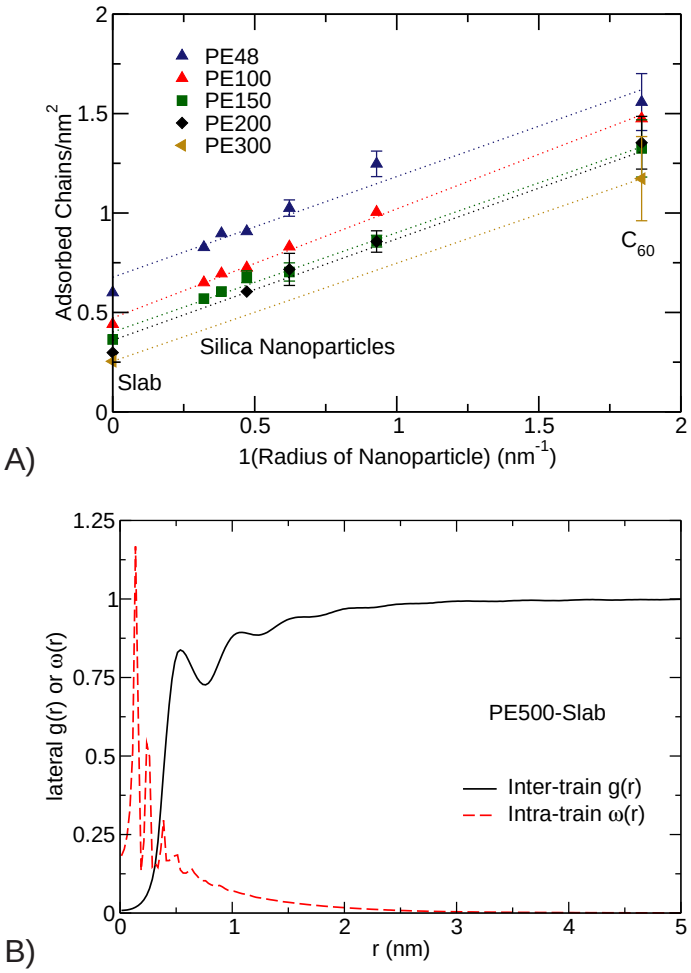

Figure 3.14: A) Number of chains per unit area in contact with the surface as a function of curvature. B) Lateral distribution functions for train segments in the PE500-Slab system. Reproduced from Ref. 6, Copyright 2012, American Institute of Physics.

3.4.3 Bound Layer Thickness

Another quantity of interest in quantifying polymer-particle interactions is the adsorbance Γ, which is defined as the total mass of polymer bound per unit surface area. Adsorbance can be calculated by integrating the density profile of the polymer chains in contact with the surface following the expression

$$\Gamma = \frac{\int_{R_{\text{eff}}}^{\infty} \phi_{\text{ads}}(r)\, dr}{A}, \tag{3.24}$$

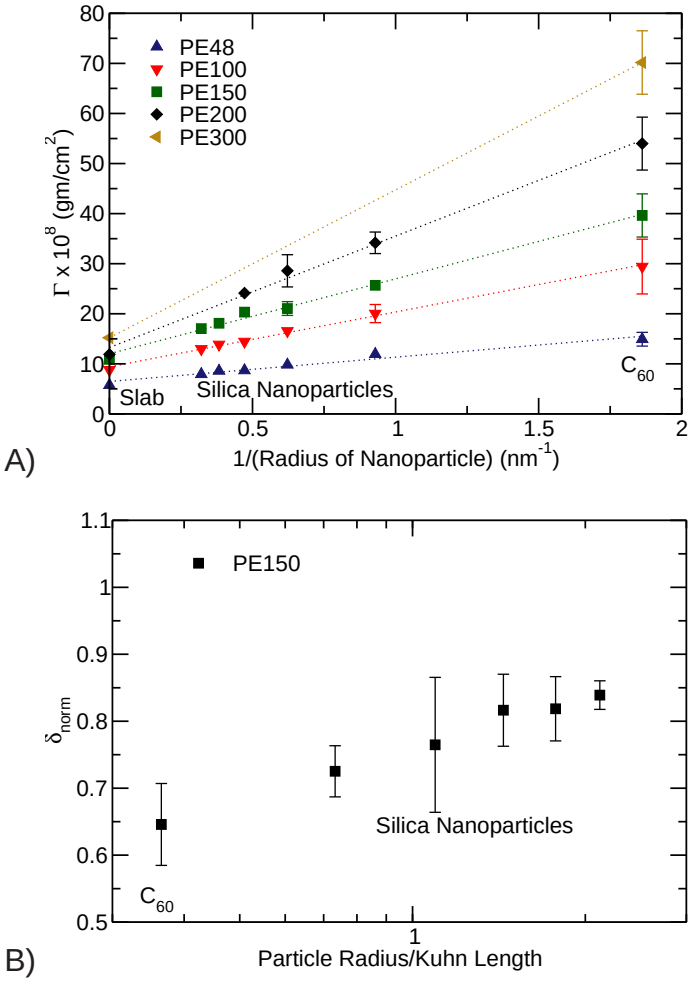

Figure 3.15: A) Adsorbance increases with increasing particle curvature B) Normalized RMS layer thickness $\delta_{\text{norm}} = \delta_{\text{RMS}}/\delta_{\text{RMS}}^{\text{Slab}}$ for PE150 systems. Reproduced from Ref. 6, Copyright 2012, American Institute of Physics.

where, R_{eff} is the effective radius of nanoparticle, ϕ_{ads} is density profile of the polymer chains in contact with the surface and *A* is the polymer accessible surface area. It is noted that the increased number of polymer chains forming contact with the surface and length of tail segments (resulting from shorter trains) will directly alter the amount of polymer mass bound to the surface. Indeed, a monotonic increase in adsorbance is observed for all the systems studied as shown in Figure 3.15A.

The extent of the polymer layer in contact with the surface can be quantified

by defining an average thickness of the bound layer which serves a vital parameter in predictive design of dispersions and fine tuning of the degree of flocculation [189]. Following the definition given by Scheutjens and Fleer [27]. the root mean square (RMS) thickness of the bound polymer layer is given by

$$\delta_{\text{RMS}} = \sqrt{\frac{\int_{r=0}^{\infty} \phi_{\text{ads}}(r) r^2 \, dr}{\int_{r=0}^{\infty} \phi_{\text{ads}}(r) \, dr}}, \tag{3.25}$$

where ϕ_{ads} is the density profile of the polymer chains in contact with the surface and r is the distance from the surface. The calculated values of RMS thickness of polymer bound layer on silica slabs ($\delta_{\text{RMS}}^{\text{Slab}}$) are listed in Table 3.5. These values have a magnitude of the order of the bulk polymer radius of gyration (R_{g}^{0}) [27]. In a recent study, Harton et al. [3] employed the lattice-based Scheutjens-Fleer self-consistent mean-field theory [27] and found that the curvature can decrease the bound layer thickness by 50$\%$ for the particles of size equivalent to polymer Kuhn segment length relative to a flat surface. The origin of this effect lies in the geometric arguments discussed earlier. As hypothesized by Garvey et al. [186, 187], if the volume (mass) of polymer in contact with the surface per unit area remains constant then an increase in particle curvature will result in decrease of thickness due to excess volume available per unit area for a corresponding shell surrounding the nanoparticle. Baker et al. [188] recognized that geometrical corrections "systematically undercorrect" the bound layer thickness.

The findings in this study agree with a reduction of the layer thickness. However, the additional feature emerging from the detailed atomistic simulations is that the increased adsorbance for smaller particles presents a competing effect, which leads to a lower reduction (30$\%$ to 35$\%$) of the layer thickness as shown in Figure 3.15B for the PE150 systems (all particle sizes considered for this chain

Table 3.5: Bulk polymer chain size R_g^0 and corresponding RMS thickness of adsorbed layer with silica Slab (δ_{RMS}^{Slab}). Reproduced from Ref. 6, Copyright 2012, American Institute of Physics.

Chain Length	R_g^0(nm)	δ_{RMS}^{Slab}(nm)
48	1.09 ± 0.01	1.14 ± 0.01
100	1.68 ± 0.03	1.74 ± 0.03
150	2.17 ± 0.02	2.11 ± 0.09
200	2.50 ± 0.06	2.33 ± 0.08
300	3.14 ± 0.04	2.88 ± 0.03
500	3.85 ± 0.04	3.12 ± 0.08

length). This analysis not only confirms the importance of volumetric corrections [186–188], but it also establishes that variation in adsorbance originating from local stiffness is an important contributing factor in curvature-induced effects on RMS thickness of polymer bound layer. It should be noted that the variations of bound layer thickness as a function of intrinsic rigidity of polymer have been observed using the worm-like chain models in polymer solutions and nanocomposites due to the changes in polymer structure along the normal to the surface [14, 191]. In this chapter, the changes induced by packing along the surface due to curvature-induced effects for the particle sizes comparable to the polymer Kuhn length were reported and discussed in detail.

3.5 Conclusions

This chapter presented a detailed atomistic study of a polymer melt in the proximity of a flat or highly curved surface and examined changes induced by the particle curvature at length-scales comparable to the polymer Kuhn segment. Large system sizes were prepared to avoid confinement effects and studied employing Monte Carlo algorithms involving a preferential sampling scheme that focuses on accelerating equilibration in the proximity of surface without sacrificing

the explicit representation of bulk material. A new implementation of connectivity-altering Monte-Carlo move together with an extended reptate algorithm was discussed. It was demonstrated that the extended reptate move facilitates transfer of polymer mass from the surface to bulk polymer. The analysis performed in this study elaborates that these new methods can enhance sampling significantly and render the study of large systems of long macromolecules at interfaces feasible.

The findings show that the high surface curvature induces considerable changes in the polymer-particle interactions that are dependent on the polymer architecture. In particular, surface concentration is directly affected by the free energy penalty imposed by extending long contacts of PE along the surface of small nanoparticles. An increased number of train segments belonging to different chains were shown to partially compensate for this phenomenon, but the local packing characteristics such as the correlation hole effect hinder the anticipated scaling. Eventually, shorter train segments allow formation of an increased number of contacts with different polymer chains surrounding the nanoparticle. The latter effect (together with slightly longer tail segments) leads to an increase in the adsorbed polymer mass per unit area on a highly curved surface. Previous experimental [3, 186–188] and theoretical [3] studies have established that geometrical arguments promote a decrease of the bound layer thickness. The atomistic simulations in this chapter support this decrease however the intriguing increase in polymer mass per unit area in contact with the surface suggests that this effect was overestimated in previous work [3].

It should be noted that this analysis of bound layers does not account for variability in the strength of interactions for the contacts made. Train segments of longer length are expected to exhibit increased interactions with the surface therefore despite an increased number of chains in contact with the surface, the bound layer could provide for overall decreased steric repulsion between multiple

particles immersed in a polymer melt. Incorporation of a finite concentration of nanoparticles to study such phenomena requires prohibitively large system sizes in atomistic detail. An alternative approach to gain insight on the thermodynamics of these bound layers is the study of solely a pair of particles to extract free energy profiles as a function of separation [79, 184]. Another attractive avenue for such studies is employing coarse-grain descriptions of polymer that account for local rigidity [14, 209, 210] and faithfully capture the characteristics of polymer bound layer. The next chapter will focus on developing such coarse-grained descriptions to model polymer-particle interactions. It is anticipated that for all the cases mentioned above, the techniques described in this chapter that focus computational effort in proximity to the surfaces will prove to be beneficial.

Chapter 4 Hierarchical Modeling of Polymer-Nanoparticles

4.1 Introduction

Interactions of polymers with nanoparticles are complex in nature and both enthalpic and entropic contributions play significant role in determining the effective polymer-nanoparticle potential [15, 22, 23]. Polymer chains gain enthalpy by interacting with the nanoparticle atoms, but restrictions posed on their conformational degrees of freedom due to presence of nanoparticle leads to loss of entropy. Capturing such complex interactions is an outstanding challenge in predictive modeling of polymer-nanoparticle systems. The pairwise additive forms used in modeling homogeneous polymer melts are not necessarily appropriate in modeling heterogeneous polymer-particle systems due to consideration of the many body effects [77, 78, 191]. Moreover, chemical details of particle surface and polymer also need to be considered in modeling [191]. Furthermore, stereo-regularity of polymers has shown to have a significant effect upon visco-elastic properties of polymer with different tacticity [211], which makes it imperative to incorporate the effects of tacticity and chemical architecture in polymer models as well. Encompassing such a multitude of information in a few parameters describing the model polymer-particle systems is the subject of this chapter.

Describing the structure and properties in good agreement with experiments is not the only challenge in developing these models. Large system sizes required

for avoiding finite size effects in polymer-particle systems up to polymer relaxation time [6] add up to the computational challenges in such studies. The limitations posed by large system sizes can be partially addressed by using coarse-grained (CG) models. Grest and Kremer [212, 213] provided one of the earliest CG representation for model polymer. Their generic model represented the polymer as a bead-spring system, the efforts in recent years have taken the chemical details of polymers into consideration. Numerous studies in the past years have focused on deriving effective CG potentials for various polymers with specific chemical architecture such as *trans*-1,4 Polyisoprene [71], poly(ethylene oxide) [214], poly(methyl methacrylate) [209], polystyrene [72, 73, 210, 215–218], and bisphenol-A-polycarbonate [76]. On the other hand, some studies have also focused on developing CG representation of nanoparticles [84, 219–221]. Combining the coarse-grained models of specific polymers and nanoparticle surfaces is not straight forward. Deriving the cross-interactions requires careful consideration of the polymer-mediated interactions [92]. Such considerations require rigorous methodologies [7, 210] tailored for specific polymers and model particle surfaces.

It is important to acknowledge that significant progress has been made during recent years in the simulation methods applied to polymer melts and polymer nanocomposites [2, 6, 65, 66, 69, 195]. These advances in simulation methods in addition to the progress in CG representation of polymer nanocomposite melts can provide an effective tool for modeling the interface of polymer and nanoparticles. The previous chapter discussed a simulation methodology, which allows rapid equilibration of polymer in contact with the surfaces. In this chapter, efforts are focused on developing CG representation to capture the polymer-particle interactions incorporating effect of intrinsic stiffness of polymer at local length scales. Polyisoprene (PI) at a silica surface is chosen as the system of study and CG interaction potentials are derived. As the results in this chapter will show, the potentials

derived for polymer-particle interactions are able to predict the polymer bound layer in quantitative agreement with the atomistic simulations.

4.2 Models and Systems

The atomistic model of *trans*-Polyisoprene prescribed by Faller et al. [178] modified for *cis*-1,4 Polyisoprene (*cis*-1,4 PI) was employed to represent fully atomistic polymer matrix as in the literature [222]. The atomistic models of silica nanoparticle and surface were same as discussed in the previous chapter. For atomistic simulations of pure polymer melt, a system containing 100 *cis*-1,4 Polyisoprene 24*mer* chains (*cis*-1,4 PI24*mer*) was employed. This system contained 31,400 atoms. The atomistic configurations were mapped to their CG equivalent by applying a scheme adopted from the work of Reith et al. [7], where the center-of-mass (COM) of the first and last carbon atoms of two successive monomers were used as the CG interaction site. Figure 4.1 demonstrates the atomistic to CG mapping scheme.

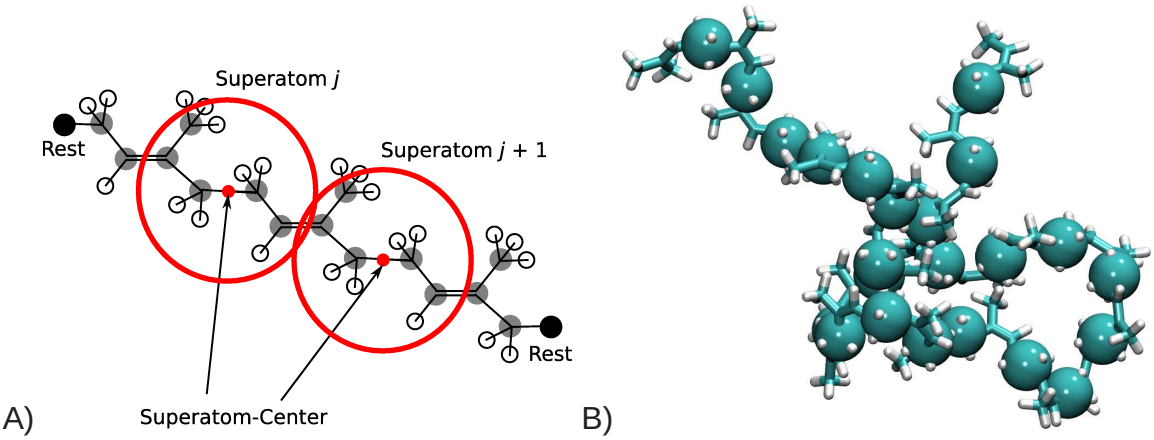

Figure 4.1: A) CG mapping scheme for *trans*-1,4 Polyisoprene adapted from Ref. 7 and B) CG bead positions are shown for a *cis*-1,4 Polyisoprene 24*mer* overlapped with the atomistic representation.

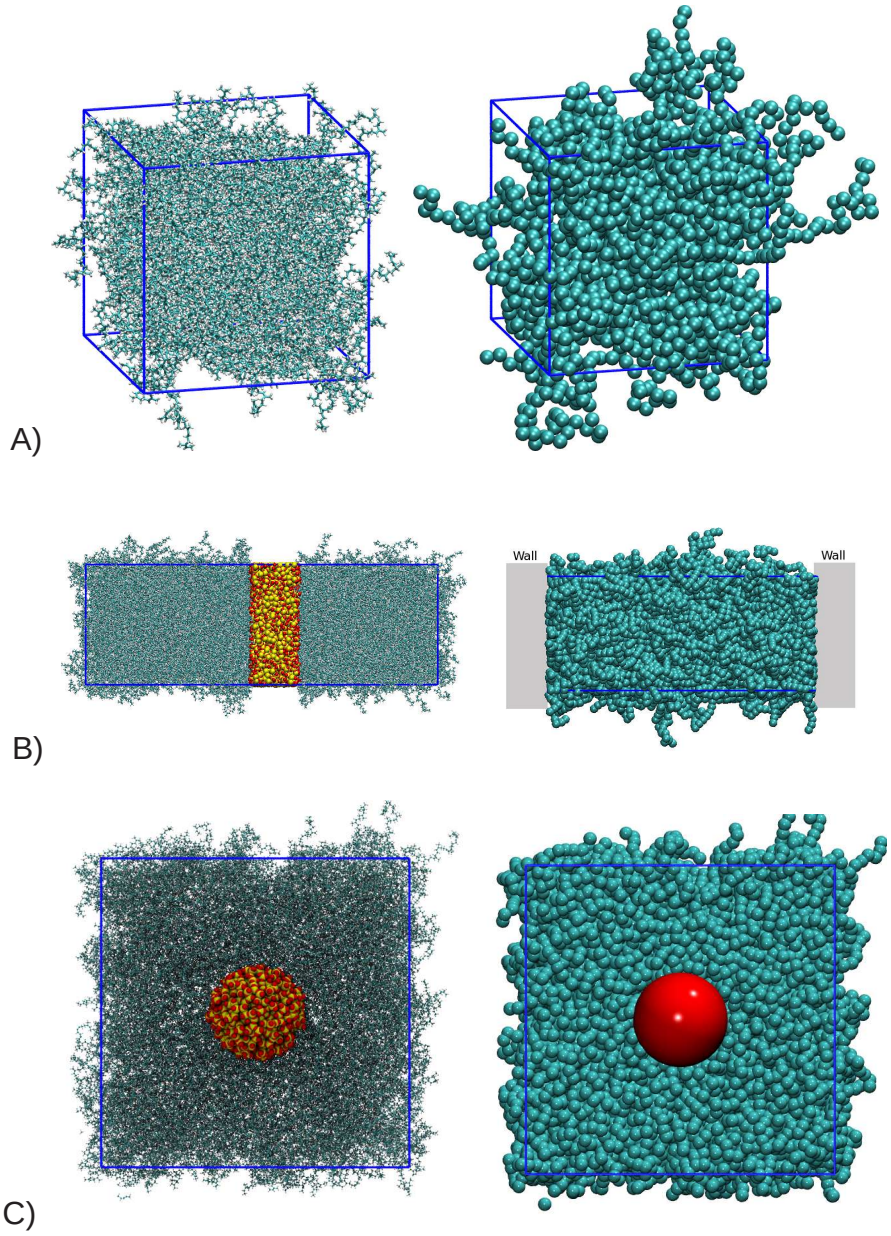

Figure 4.2: Atomistic (left) and mapped CG (right) representations for *cis*-1,4 Polyisoprene 24*mer* A) bulk polymer melt, B) with and flat surface (Slab), and C) with SIL-2.0 nanoparticle.

While obtaining CG models of a bulk polymer melt is straightforward (Figure 4.2A), some amount of effort was required in preparing a *cis*-1,4 PI24*mer* Slab system. The silica atoms were completely removed from the simulation box and the atomistic chains were mapped to the CG interaction sites. Further to this point,

the polymer chains in the box were translated such that each surface of the Slab is represented by the extremities of the simulation box. The equivalent potentials to mimic the Slab were incorporated by the means of wall potentials in Gromacs [204] as shown in Figure 4.2B. There are two main advantages of this approach. First, removal of the silica atoms leads to decreased number of beads in the system, which reduces computational efforts during simulations. Second, efforts required for deriving CG potentials for intraparticle CG interactions are avoided.

Going forward, CG interaction sites corresponding to the polymer chains were obtained for the *cis*-1,4 PI24*mer* SIL-2.0 system and the SIL-2.0 particle was substituted by a single-site at the particle COM (Figure 4.2C). This mapping scheme also has the advantages similar to the *cis*-1,4 PI24*mer*-Slab system. In addition to the SIL-2.0 system, a series of systems with a CG representation of nanoparticle ranging from nominal radius 0.5-2.5 nm were prepared for the study of curvature induced effects by employing *cis*-1,4 PI-Silica systems.

4.3 Simulation Methodology

4.3.1 Atomistic Simulations

A 50 ns atomistic NPT molecular dynamics simulation of *cis*-1,4 PI24*mer* bulk polymer melt system was performed using Gromacs v4.5.5 [204] (referred to as melt simulations in later part). The non-bonded interactions were truncated at a cut-off distance of 1 nm and a timestep of 1 fs was used for integrating the equations of motion. Temperature was maintained at 413 K by applying velocity-rescaling temperature coupling [223]. The Berendsen barostat [224] with a time constant of 1 ps was employed to maintain an average system pressure of 1 bar. Atomistic NPT molecular dynamics simulations of 400 *cis*-1,4 PI24*mers* in the

presence of a silica Slab and 800 *cis*-1,4 PI24*mers* with a silica nanoparticle of radius $\simeq$ 2 nm (SIL-2.0) were performed. The cut-off distance, timestep, temperature coupling and barostat were kept similar to the melt simulations, except that separate temperature coupling for Slab/nanoparticle and polymer was employed and for the polymer matrix containing silica Slab, semi-isotropic pressure coupling was applied so that the dimensions of Slab surface perpendicular to z-axis remain constant. The duration of the simulations exceeded 45 ns and 30 ns for the systems containing Slab and SIL-2.0 respectively.

4.3.2 Coarse-Grained Potentials for Polymers on Flat Surfaces

The first step in the development of CG interaction potentials for polymer-polymer interactions was the generation of a CG simulation trajectory corresponding to the atomistic melt simulations following the CG mapping scheme discussed in the previous section. The distributions for bond lengths $P(l)$, angles $P(\theta)$, radial distribution function $g(r)$ and dihedral angles $P(\phi)$ for mapped CG representations were calculated. These distributions were utilized as the target distribution functions for deriving CG bonded, angular, dihedral and nonbonded interaction potentials. The initial guess potential for bonded interactions was given by

$$V^0_{\text{bonded}}(l) = -k_{\text{B}}T \ln(P(l)/l^2). \tag{4.1}$$

The initial guess for the angular potential was generated from

$$V^0_{\text{angular}}(\theta) = -k_{\text{B}}T \ln(P(\theta)/\sin\theta). \tag{4.2}$$

The initial nonbonded potential between the polymer beads were derived from the $g(r)$ as

$$V^0_{\text{nonbonded}}(r) = -k_{\text{B}}T \ln(g(r), \tag{4.3}$$

and for dihedral potentials

$$V^0_{\text{dihedral}}(\phi) = -k_{\text{B}}T \ln(P(\phi) \tag{4.4}$$

was used.

Optimizing all of the above potentials simultaneously was found to be infeasible. Therefore, interaction potentials were optimized in the order of their successive strength i.e. $V_{\text{bonded}} \rightarrow V_{\text{angular}} \rightarrow V_{\text{nonbonded}} \rightarrow V_{\text{dihedral}}$ [7]. The optimization of these potentials was carried out following the Iterative Boltzmann Inversion (IBI) method as described in the previous studies to optimize similar set of potentials [7, 225]. IBI method uses a simple Boltzmann inverse of probability distribution $P(\xi)$ for an order parameter ξ, which leads to free energy

$$F(\xi) = -k_{\text{B}}T \ln P(\xi). \tag{4.5}$$

This free energy can be used as an initial guess of potential $V^0(\xi)$. The initial guess is then updated by a correction term $-k_{\text{B}}T \ln[P^0(\xi)/P(\xi)]$ in an iterative scheme and the corrected potential is calculated by

$$V^{i+1}(\xi) = V^i(\xi) - k_{\text{B}}T \ln\left(\frac{P^i(\xi)}{P(\xi)}\right). \tag{4.6}$$

Following the above scheme, bonded, angular, nonbonded and dihedral potentials were optimized by using

$$V^{i+1}_{\text{bonded}}(l) = V^{i}_{\text{bonded}}(l) - k_{\text{B}}T \ln\left(\frac{P^{i}(l)}{P(l)}\right), \tag{4.7}$$

$$V^{i+1}_{\text{angular}}(\theta) = V^{i}_{\text{angular}}(\theta) - k_{\text{B}}T \ln\left(\frac{P^{i}(\theta)}{P(\theta)}\right), \tag{4.8}$$

$$V^{i+1}_{\text{nonbonded}}(r) = V^{i}_{\text{nonbonded}}(r) - k_{\text{B}}T \ln\left(\frac{g^{i}(r)}{g(r)}\right), \tag{4.9}$$

and

$$V^{i+1}_{\text{dihedral}}(\phi) = V^{i}_{\text{dihedral}}(\phi) - k_{\text{B}}T \ln\left(\frac{P^{i}(\phi)}{P(\phi)}\right), \tag{4.10}$$

In order to evaluate the convergence of the above iterative schemes an objective function was applied, using the form

$$f_{\text{target}}(\xi) = \int w(\xi)(P^{i+1}(\xi) - P^{i}(\xi))^2 d\xi, \tag{4.11}$$

where

$$w(\xi) = \exp(-\xi), \tag{4.12}$$

is the prefactor that penalizes deviations at smaller values of ξ. Obviously, such a penalty is meaningful only in the case of nonbonded interactions at shorter distances between the first neighbors to capture the first peak in the radial distribution function. Therefore, $w(\xi)$ was set to 1 in the objective functions for bonded, angular and dihedral potential optimization scheme. For optimization of nonbonded interactions, matching of $g(r)$ alone is not sufficient as the average pressure of the system may differ by orders of magnitude. To alleviate this problem, pressure corrections were employed following the recipe provided by Wang et al. [226]. For an iterative process with interactions being truncated at a cutoff distance r_{cut}, the

correction to the potential at ith iteration is given by

$$\Delta V_i(r) = A_i \left(1 - \frac{r}{r_{\text{cut}}}\right), \tag{4.13}$$

where the ramp A_i is calculated following

$$-\left[\frac{2\pi N\rho}{3r_{\text{cut}}}\int_0^{r_{\text{cut}}} r^3 g_i(r)dr\right] A_i \simeq (P - P_{\text{target}})V. \tag{4.14}$$

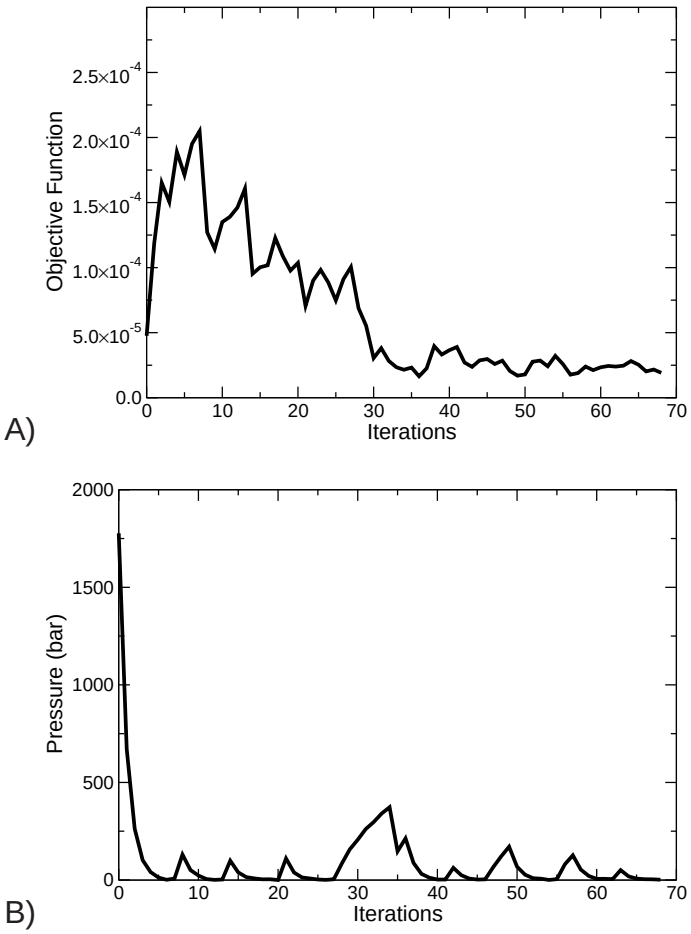

Figure 4.3: Variations in A) objective function f_{target} and B) average system pressure as a function of number of iterations. Notice that pressure correction steps compete with matching $g(r)$.

In Eq. 4.14 N is the total number of particles in a system of volume V, number density ρ and pressure P. P_{target} is the pressure to be achieved. Figure 4.3

presents an interesting aspect of the pressure corrections. It can be observed that an improvement in the objective function f_{target} is associated with deviations in the average system pressure. Owing to this, corrections were performed alternate in an alternating scheme. Pressure corrections were performed until the relative change in pressure saturated to a predefined value and then corrections to match $g(r)$ were applied until the objective function converged to a certain degree. The alternate steps of corrections were continued until a good match of $g(r)$ was obtained with an average system pressure $\approx$ 2 bar. This approach lead to the estimates of the CG interaction potentials (Figure 4.4), which enabled NVT molecular dynamics simulations with 3 fs timestep and 1.5 nm cut-off distance resulting in the average system pressure very close to 1 bar ($\simeq$ 5 bar) and excellent quantitative agreement between the target and CG probability distributions (Figure 4.5). These CG potentials were further used in simulations of *cis*-1,4 PI with a flat surface (denoted by wall potentials) for estimation of effective CG polymer-surface interaction potentials.

For estimation of effective CG interaction potentials between polymer bead and silica Slab, atomistic simulations of the *cis*-1,4 PI24*mer* Slab systems were performed. The target radial distribution function of the CG beads as a function of distance from the Slab surface obtained from the mapped *cis*-1,4 PI24*mer* Slab trajectory were used for deriving effective interaction potential following the IBI procedure. This iterative process followed the Eq. 4.9. No efforts were made to apply pressure corrections during this optimization process. It should be noted that these optimizations are carried out in the NVT ensemble and in absence of periodic boundaries along z-axis. It will be discussed along with results that the interaction potentials estimated here not only reproduce the “Total” radial distribution of CG beads, but also provide the distributions of tail, train and loop segments in good quantitative agreement with the target distributions.

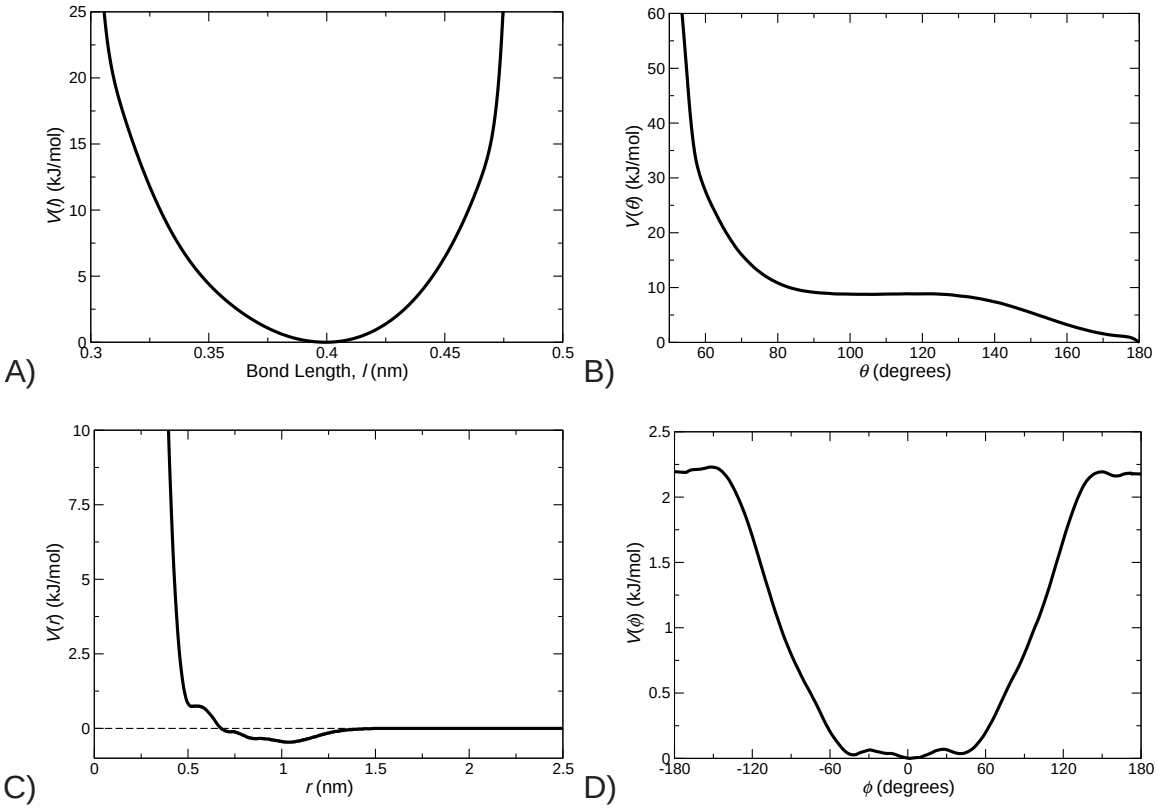

Figure 4.4: Estimates of CG interaction potentials for *cis*-1,4 Polyisoprene derived from IBI method. A) Bonded potential, B) angular potential, C) nonbonded potentials, and D) dihedral potential.

4.3.3 Transferring CG Interactions to Nanoparticles

This section outlines a procedure, that provides estimates of the interaction potentials between a polymer bead and a particle of arbitrary curvature based upon the interaction potentials between the polymer bead and a flat surface. Nielsen et al. [227] presented a scheme, where the interaction potential between a single interaction site of the substrate and a polymer bead (single-site potential, $u(\xi)$) can be derived by taking the second derivative of the effective interaction potential between the surface and the polymer ($U_{\text{Slab}}(\xi)$) and dividing it with a term accounting

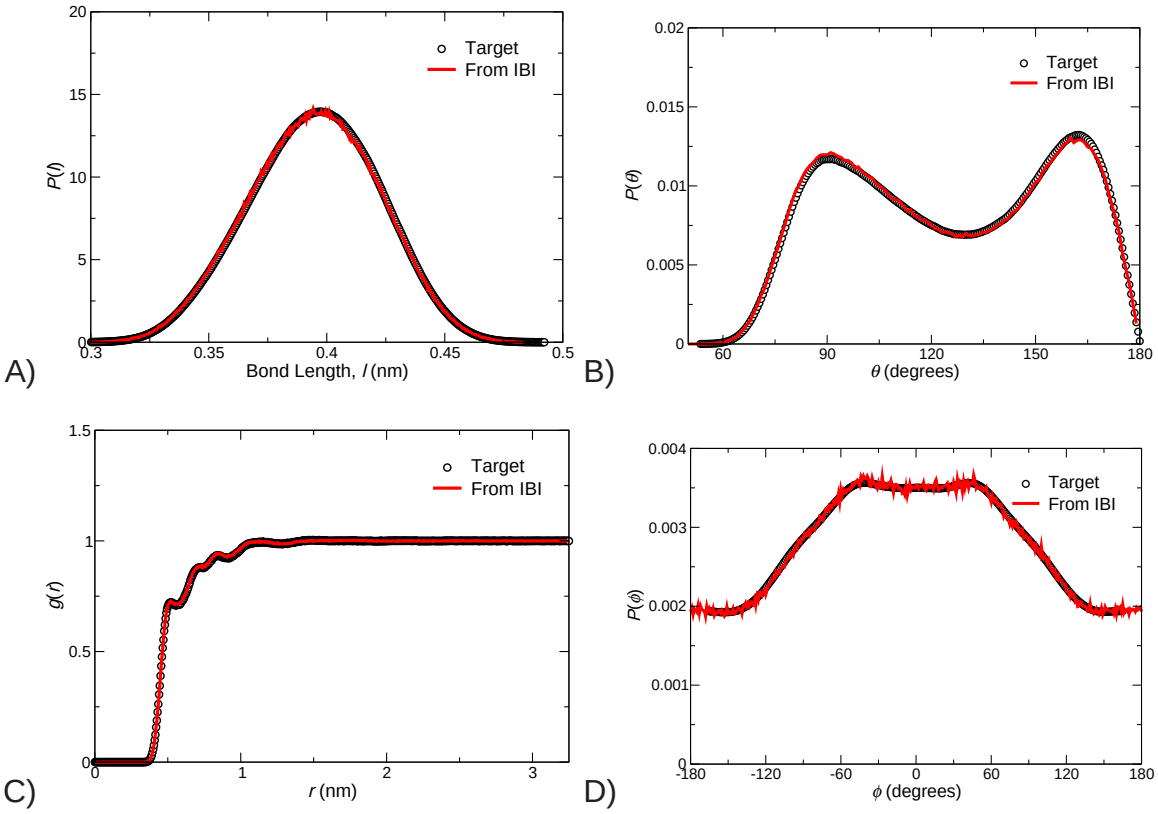

Figure 4.5: Comparison of A) bond length, B) bond angles, C) radial distribution function, and D) dihedral angles for *cis*-1,4 Polyisoprene obtained from the derived CG interaction potentials with the respective target distributions.

for the number density of the interaction sites ρ. Using the functional form

$$u(\xi) = \frac{U''_{\text{Slab}}(\xi)}{2\pi\rho\xi}, \tag{4.15}$$

the single-site interaction potential between one interaction site on the Slab surface and a CG polymer bead is shown in Figure 4.6A. Once the single-site potential is calculated, the effective interaction potentials between the nanoparticles of any arbitrary curvature i.e. radii can be calculated by integrating the interactions over the particle volume within the cutoff distance (for details see Appendix A). Such potential between a segment of *cis*-1,4 PI and silica particles are presented in Figure 4.6B.

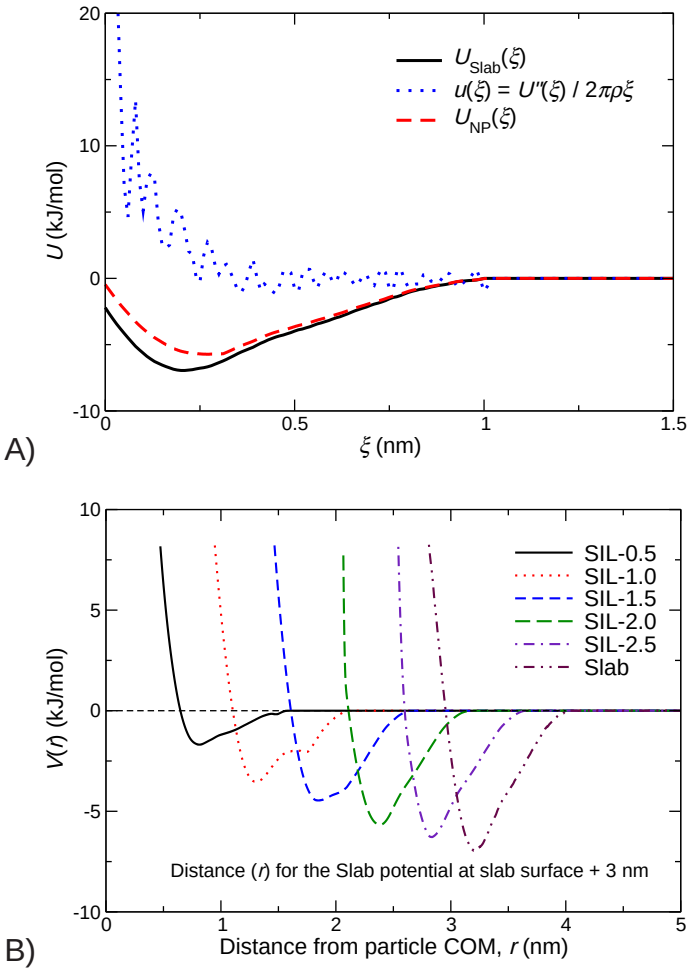

Figure 4.6: A) Figure showing polymer-slab interaction potential $U_{\text{slab}}(\xi)$, calculated single-site potential $u(\xi)$ and effective polymer-nanoparticle interaction potential $U_{\text{NP}}(\xi)$ obtained from integration. B) Effective interaction potentials between CG polymer bead and silica Slab (as a function of distance from the surface), and effective interaction potentials from integration of single site potential for nanoparticles of different radii. Part B: Reproduced with permission from Macromolecules, 'submitted for publication'. Unpublished work copyright 2013 American Chemical Society.

4.4 Results and Discussion

The effective interaction potentials between silica Slab/nanoparticles and CG polymer beads were subsequently employed in a 15 ns CG NVT molecular dynamics simulations of the matrix of *cis*-1,4 PI24*mers* containing silica

Slab/nanoparticles. The results from these simulations are discussed in the following sections.

4.4.1 Density Around a Nanoparticle

The polymer density as a function of distance from the Slab surface or nanoparticle center-of-mass (COM) was further decomposed into free chains and polymer chains in contact with the surface (or adsorbed chains). Any polymer chain with a bead within 4 Å from the effective surface (defined on the basis of effective volumes reported in the previous chapter) of Slab or nanoparticle was defined as a chain in contact. The radial distributions for the adsorbed chains were further decomposed into the tail, train and loop contributions. Figure 4.7 shows the comparison of the radial distribution functions and their decomposition into different segments. It can be observed that the effective interaction potentials between silica Slab and CG polymer bead obtained from the IBI procedure provide excellent match for both the total radial distribution and the decompositions. The same holds true for the systems containing SIL-2.0, a result that indicates the applicability of effective potentials obtained from the integration of the single-site potential in describing conformation of the polymer in contact with the Slab surface and the nanoparticles.

4.4.2 Length of Contacts

In order to further investigate the accuracy of the derived effective potentials, the probability distributions of tail, train and loop segments obtained from the atomistic and CG simulations of Slab and SIL-2.0 systems were compared. Figure 4.8A presents a good agreement between the segment probability distributions obtained from the atomistic and CG simulations. This result further indicates

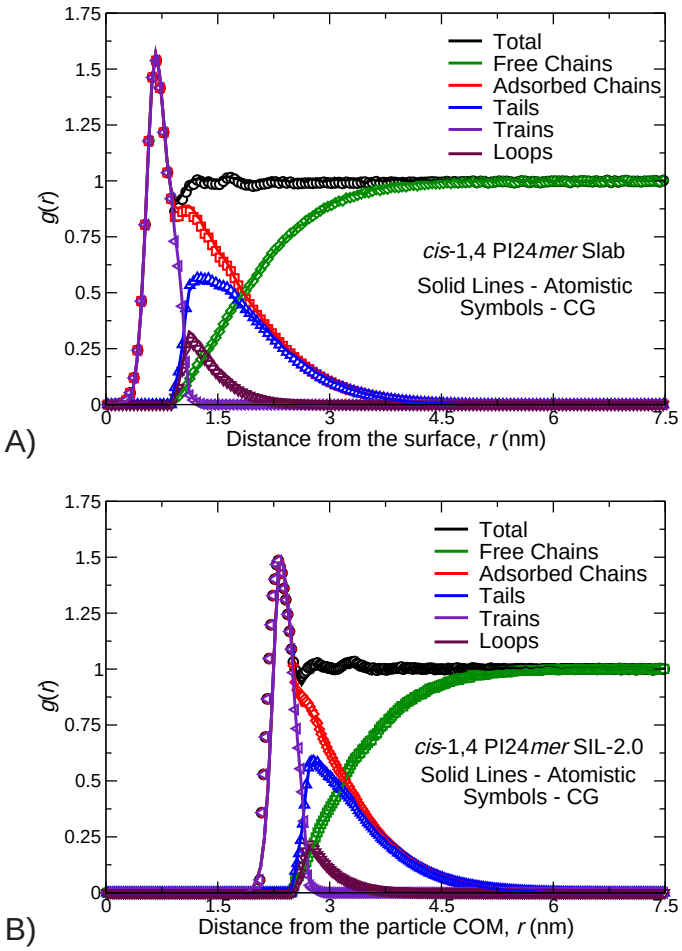

Figure 4.7: Radial distribution functions of *cis*-1,4 Polyisoprene 24*mer* beads and their decomposition A) as a function of distance from the Slab surface and B) as a function of distance from the COM of SIL-2.0 particle. Reproduced with permission from Macromolecules, 'submitted for publication'. Unpublished work copyright 2013 American Chemical Society.

that the derived effective potentials not only capture the density fluctuations as a function of distance from the surface of Slab/COM of nanoparticle, but they also very well capture the variations in the lengths of the individual segments. To the best of author's knowledge this is the first time when such a quantitative agreement is reported. Figure 4.8B shows the probability of train segment lengths for different sizes of nanoparticles. It can be observed that the smallest nanoparticle shows a significantly higher probability of forming shorter train segments and vanishingly small probability of forming long trains segment. In contrast to this, larger

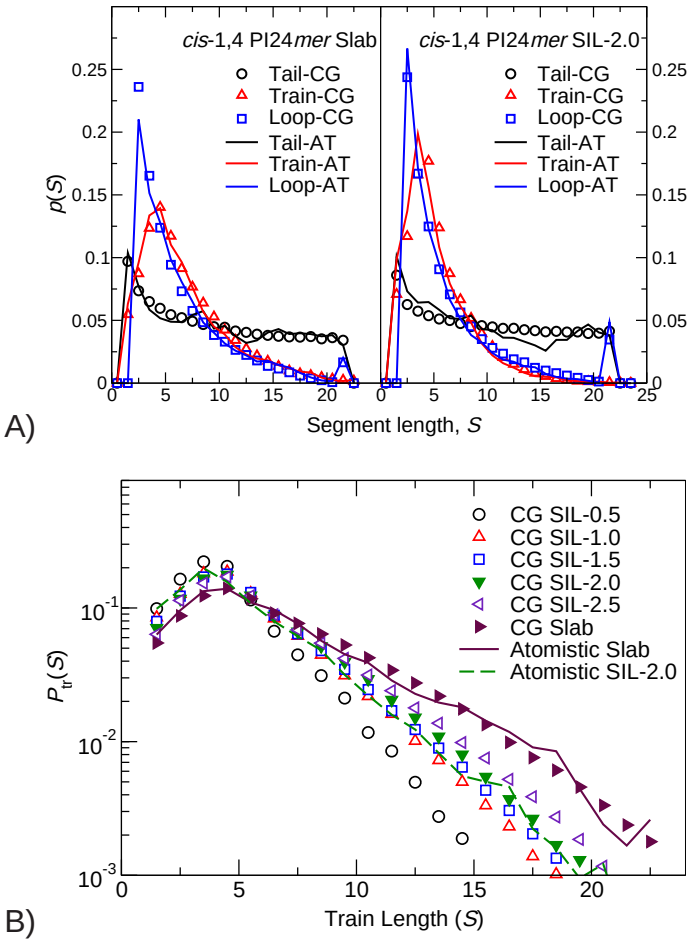

Figure 4.8: A) Comparison of probabilities of forming a segment of specific length obtained from atomistic and CG simulations for Slab and SIL-2.0 systems. B) Probability distributions for train segments from CG simulations for the silica Slab and different sizes of nanoparticles studied. Part B: Reproduced with permission from Macromolecules, 'submitted for publication'. Unpublished work copyright 2013 American Chemical Society.

nanoparticles and the Slab show an appreciable probability of forming larger train segments. In the previous chapter, similar trends as a function of particle size were observed and attributed to the significant entropic penalty for forming larger train segments at the surface of the smallest nanoparticles. This result demonstrates that the effective interaction potentials derived in this study are capable of capturing these phenomena quantitatively.

4.4.3 Bound Layer Thickness

The effect of particle size upon the normalized RMS bound layer thickness is shown as a function of the particle size relative to the polymer Kuhn segment length. For polyethylene (PE), a Kuhn segment length of 1.47 nm was adopted from the previous study [6]. For *cis*-1,4 Polyisoprene, a Kuhn segment length of 0.82 nm was adapted following Rubinstein. [64]. The plot reveals a very interesting trend for the decrease in the value of δ_{norm}. It can be observed that in spite of the differences in the chemical architecture of polyethylene and *cis*-1,4 Polyisoprene, the scaling of δ_{norm} with respect to the particle size relative to Kuhn segment length seems to collapse on the same master curve. Such similarity in the scaling of bound layer thickness may lead to more general scaling law for polymer with different architectures.

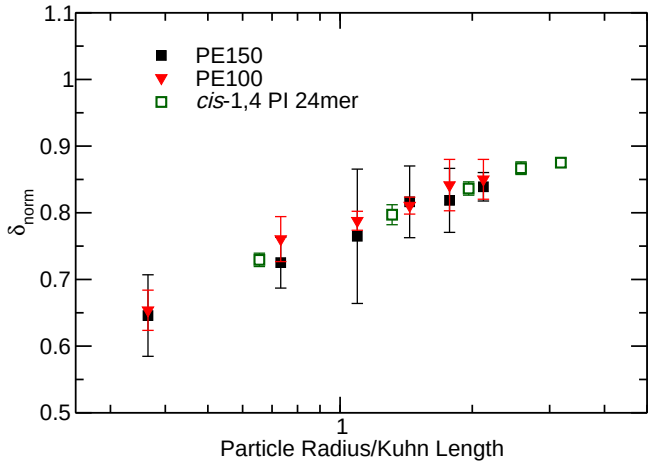

Figure 4.9: Normalized RMS bound layer thickness as a function of particle size relative to polymer Kuhn segment length. Reproduced with permission from Macromolecules, 'submitted for publication'. Unpublished work copyright 2013 American Chemical Society.

.

4.5 Conclusions

In this chapter, the methodology for developing coarse-grained models for the polymer-particle interactions was outlined. A hierarchical modeling approach started with the estimation of CG polymer-polymer interactions using IBI method [7]. Using the methods available in literature [226], the potentials were refined to provide a reasonable pressure in the system. These potentials were subsequently used for parametrization of the interactions between a flat surface and polymer in CG representation. It was demonstrated that the method [227] for calculating the interaction potentials for particles of arbitrary curvature based upon the CG interactions between polymer and flat surface not only reproduces the "Total" radial distribution functions for the Slab and nanoparticle systems, but also shows remarkable capability of capturing the density profiles for the tails, trains and loops. Furthermore, the effects of curvature upon the train segment distributions [6] are also captured with the potentials derived in this chapter. It is emphasized that such kind of coarse-grained potential development methodology not only reduces the effort required in optimization of potentials with particles of different sizes, but also provides an excellent description of the polymer in the contact with the nanoparticle surface. This was the first time when such accuracy of CG models was demonstrated.

Up to this point, the studies were focused on the study of the interfacial phenomena in the systems, which do not involve reactions. In the next chapter, a problem of significant industrial interest involving reaction-diffusion phenomena near the interfaces is studied using the lattice simulations.

Chapter 5 Stochastic Modeling of Reaction-Diffusion in Chemically Amplified Resists

5.1 Introduction

During the recent years, the most advanced and sophisticated integrated circuits e.g. microprocessors and memory chips, are patterned with projection lithography. The lithographic resolution (minimum feature size R_{min}) controls the efficiency of semiconductor devices. For keeping pace with the historic growth rates given by Moore's Law, future lithographic processes must attain the resolution limit of 10 nm [228]. For meeting this challenge, imaging materials for next-generation lithography must meet a number of demands, e.g., nanoscale resolution, near-perfect pattern uniformity, and high sensitivity to radiation [**?**].

The process called chemical amplification is the basis of most sensitive resists [229–231]. There are two principal components of chemically-amplified (CA) resists: (i) A lipophilic polymer with acid-labile protecting groups; and (ii) a low concentration of photoacid generator (PAG). Generation of a strong acid catalyst is accomplished by exposing the resist to radiation, and subsequent heating at moderate temperature promotes the acid-catalyzed decomposition of the protecting groups along the polymer backbone. The deprotection reaction changes the polymer polarity for development in an aqueous base. The high efficiency of CA systems is attributed to each photon absorbed by the resist generating ca. 0.3-3 acid molecules [232, 233], and each of these acid molecules cleaves hundreds of

bonds [229], therefore a low radiation dose is “amplified” through chemistry. However, there is a price for excellent sensitivity of CA resists due to limitations posed on the pattern resolution and uniformity originating from the catalytic efficiency and/or acid diffusion [57, 121, 228, 234, 235]. In addition, features with nanometer resolution are mechanically unstable due to high aspect ratio. A potential remedy to this issue is application of ultrathin films, but the potential effects of substrate interactions [60] in ultrathin films need to be quantified.

Prediction of the spatial extent-of-deprotection with nanoscale resolution clearly needs development of quantitative models of chemical amplification. It is well documented that deprotection kinetics in CA resists are controlled by acid catalyst diffusion [57, 121], but the mechanism cannot be described by a simple Fickian diffusion model [4, 113, 122]. Previous works [56, 116, 119, 137, 236] have proposed macroscopic models that include thermodynamic equilibria, free volume generation, acid trapping reactions, or concentration-dependent diffusion coefficients to describe the deprotection kinetics. These studies aim to capture particular aspects of the deprotection reaction kinetics such as the fast initial conversion or slow conversion at long times. In one of such efforts, Croffie et al. [119] introduced concepts from polymer physics to describe an initially fast deprotection rate, concurrent with the creation of free volume from escaping volatile by-products. The additional free volume subsequently relaxes and leads to a dense polymer resin that arrests the acid mobility. In a different approach, the overall deprotection rate is described as a series of thermodynamic equilibria between the acid catalyst and protected or deprotected polymer [57]. Finally, a number of studies have employed a phenomenological concentration-dependent acid diffusivity that increases with extent-of-deprotection [56, 118, 237]. In any of the cases mentioned here, it is unclear whether such descriptions can be successfully extended to model material behavior at the nanoscale, where molecular parameters such as

the distances between the reacting centers and acid-anion pair play a significant role [238]. These challenges in capturing macroscopic behavior with a mesoscopic model are further increased by the anticipated local fluctuations in composition and density [239], and it is not certain that mean values of the estimated parameters such as acid hopping times can adequately describe the transport mechanism in a reacting glassy polymer matrix. In fact, previous studies have failed to report a unified model of parameters (e.g., trapping rate constants) that captures the extent–of–reaction at all acid loadings.

In this chapter, a concerted modeling and experimental approach is employed to demonstrate that a surprisingly simple model of anomalous diffusive behavior can predict macroscopic deprotection rates. This model is based on an acid hopping process representing subdiffusive character, which generates extensive short-time reaction followed by long-time limiting behavior. The model is able to predict the higher-order dependence of deprotection rates on acid concentration accurately. Based on the recent studies of anomalous diffusion in complex materials [240], it is proposed that deprotection rates are controlled by an underlying non-exponential distribution of acid hopping rates. This study aims at providing a unique framework to examine the effects of polymer dynamics on reaction front propagation in CA resists. This is the first step towards quantitative modeling of reaction-diffusion phenomena in polymer films. This work opens the route for future efforts that will examine the effect of polymer film thickness.

5.2 Input from Experiments

The experiments were performed by Stein Research Group at the University of Houston. The aim of experiments was to measure the extent–of–reaction in a model chemically–amplified resist with infrared absorbance spectroscopy. These

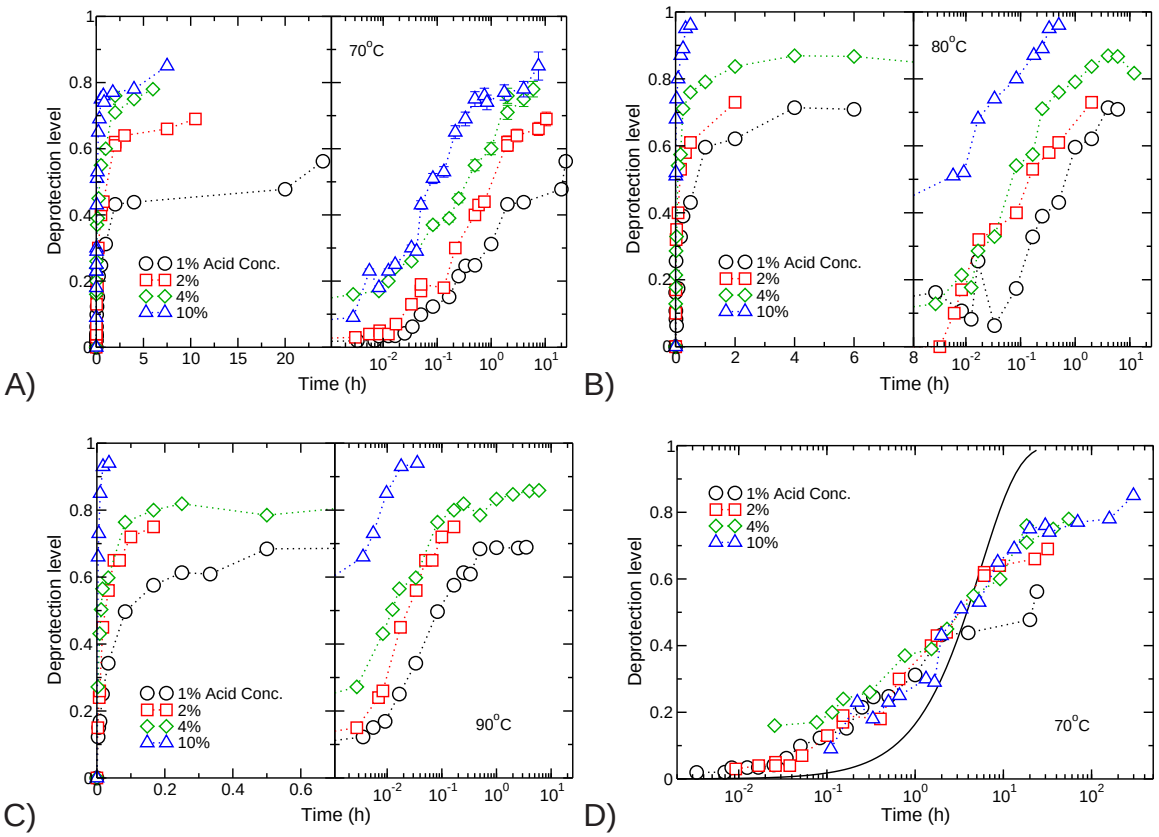

Figure 5.1: A-C) Deprotection levels as a function of time on linear and logarithmic scales. The curves have similar shapes, and they can be superimposed by assuming a nonlinear dependence on acid loading as illustrated in D) Solid line is the best-fit profile to a first-order reaction. Reprinted with permission from Ref. 8. Copyright 2012 American Chemical Society.

experiments were performed at variable catalyst loading, reaction temperature, and reaction time. The reaction temperature was always maintained at least 50 K lower than the polymer's glass transition temperature. A random copolymer resin poly(4-hydroxystyrene-co-tertbutyl acrylate) (PHOST–PTBA), 60% PHOST by volume, with molecular weight M_n = 10.4 kg/mol and polydisperty index of 1.8 was used with the photoacid generator (PAG) triphenylsulfonium perfluoro-1-butanesulfonate (PFBS).

All formulas were prepared by dissolving the polymer, PAG in propylene glycol monomethyl ether acetate (PGMEA) and double–side polished p-type (100)

silicon wafers were used as substrate. In order to study deprotection kinetics, resist formulas were prepared with PHOST-PTBA resin and PAG loadings of 1 wt%, 2 wt%, 4 wt% or 10 wt%. The polymer concentration in PGMEA was 10 wt% for all studies. Deprotection levels quantified by the fraction of deprotected groups in resist films of thicknesses of 250–300 nm were calculated employing Fourier-Transform Infrared (IR) Spectroscopy at 70°C, 80°C, and 90°C temperatures as a function of post-exposure bake time. The deprotection profiles for the mentioned acid loadings at the three temperatures are shown in Figure 5.1A-C.

5.3 Modeling Methodology

The simulations employed a lattice model with the material divided into cubic elements of volume of 1 nm^3, and an acid molecule represented by a single particle residing in one of the sites. Simple calculations based on the density of the resin lead to estimates of 3 HOST and 2 TBA groups in each lattice site. In addition, the size of the photogenerated ions is estimated in the range of 0.2-0.3 nm^3, which is smaller than the volume of each cell but larger than the polymer groups. Molecular characteristics such as anion orientation [238] and fluctuations in local concentration [239] are critical factors in determining the actual distances between deprotecting groups and acid molecules. It will become evident from the discussion in the later sections that in our approach such features are implicit to the description employed to model the distribution of time intervals for acid hopping within the cubic lattice. The model assumes that deprotection reaction, escape of volatile products, and volume relaxation all are fast events, therefore acid mobility is the only factor controlling the deprotection rates. Furthermore, when an acid molecule jumps into a new site, deprotection of the microscopic volume occurs instantaneously. Acid molecules randomly distributed at initial locations do not deprotect

any material – a hopping event must be selected prior to occurrence of a deprotection event. If acid molecules are allowed to deprotect *before* a hopping event, it will produce an instantaneous deprotection level matching the acid concentration. For low acid concentrations, the difference between these initial conditions is minimal. With the initial condition that allows deprotection event only after a hopping event takes place, deprotection profiles for a Fickian model are accelerated in proportion to acid loading. Furthermore, such an initial condition avoids a situation where all acid molecules simultaneously deprotect their cells at t = 0 [241]. For the lattice simulations, cubic lattice models with 30^3 cells were used for the optimization scheme, while final profiles were generated using cubic lattice containing 50^3 cells.

The acid hopping events on the lattice were modeled using two different algorithms. The first algorithm reproduces a random walk described by an ergodic Markov process following a stochastic Kinetic Monte Carlo approach [242, 243]. Similar methods are widely applied in the literature [57–59, 116, 134, 139] and implemented by executing reactions or displacements based on time intervals associated with these events drawn from an underlying exponential distribution

$$\psi(t) = \frac{1}{\tau} e^{-\frac{t}{\tau}}. \tag{5.1}$$

In case of spatial displacements, the Green's function for diffusion is recovered with a macroscopic diffusion coefficient D. The second algorithm used in this study employs a non-ergodic non-Markovian description, which is based on a distribution function for waiting time intervals that follow long-tail kinetics [244] to model anomalous diffusive behavior. Processes following long-tail kinetics are increasingly observed in the problems related to transport in complex systems [240, 245–250], and are supported by a developing theoretical framework [251, 252]. However, these methods have not been employed to analyze experimental data in acid-catalyzed

deprotection reactions in previous works. Additional details pertaining to the selection and implementation of the models are discussed in the Results section.

It should be emphasized that the main aim of this study is to directly test the effect of acid diffusion on the observed macroscopic deprotection rates. During the recent years, significant progress in characterizing diffusion in complex materials is fueled by development of advanced algorithms and new experimental techniques that are able to probe molecular length-scales [253–257]. In literature, different types of waiting time distributions have been proposed. In order to incorporate simulations as function calls within an optimization scheme [258], selection of a functional form enabling execution within a short time is imperative. Each function evaluation proposes a specific value of acid diffusivity D (or γ, τ depending on the model) followed by creation of a new random distribution of the acid molecules (remodeled with each evaluation), performing the simulation, and then comparison of the simulated deprotection profiles against experimental data. (It should be noted that all data are projected onto the lowest acid concentration 1 wt%, a detail further discussed in the Results section.) The optimization scheme accepts/rejects proposed changes in the parameter D based on a Metropolis criterion at a "temperature" associated within a specific number of move attempts. For a specific "temperature," 20-50 runs are performed and by cycling through low and high temperatures, a number of profiles and parameters corresponding with the local minima are generated. Since each of these runs requires hundreds of function evaluations, a simple and efficient model of anomalous diffusion [240] is absolutely essential for the success of this approach. Considering the accuracy of available data, there was no convincing physical basis for introduction of additional parameters apart from acid-acid interactions at high loadings (acid molecules are "phantom" particles in our first approach).

5.4 Results

5.4.1 Macroscopic reaction kinetics

Figure 5.1A-C present the deprotection level with respect to time at 70°C, 80°C and 90°C respectively. A number of features observed in other studies are evident in the experimental data presented here. The data reported on a linear timescale appears to depict a self-limiting reaction with a maximum deprotection level that depends on acid concentration [54, 236, 259, 260]. However, plotting the same data on logarithmic timescale reveals that the deprotection reaction continues with an extremely slow rate. A reduction in deprotection rates as the conversion increases has been discussed by other studies. Often this behavior is captured with phenomenological models, e.g., volume relaxation or a temporal acid–trapping through additional reactions [119, 261]. As mentioned earlier, these models may fail to describe experimental data for different acid loadings with the same parameters. Before addressing the phenomena that control long-time behavior, it is important to discuss the microscopic mechanisms that controls deprotection at short-to-intermediate timescales. Data from resists with different acid concentrations are used to guide this discussion. All of the data discussed here were acquired from glassy polymer resists, which means that the deprotection temperature is well-below the polymer's glass transition temperature ($T_g - T \geq 50$ K). Furthermore, unless otherwise stated, the data reviewed from other studies were also based on glassy polymer resins.

Usually the deprotection reaction is modeled as a first-order reaction with a very long catalytic chain [57, 121]. To quantitatively describe the experimental data,

a simple analytical differential equation for reaction-limited kinetics

$$\frac{d\phi}{dt} = k[\mathrm{H}^+](1-\phi) \tag{5.2}$$

was used. If [H^+] remains constant throughout the reaction, then a new parameter $K = k[\mathrm{H}^+]$ that depends linearly on acid concentration can be employed to formulate the observed deprotection. Therefore, a reduction in the acid concentration by a factor of 2 should provide a rate of deprotection twice as slow. Some studies have reported linear dependence of deprotection rate upon acid concentration [236], which is consistent with the model in Eq. 5.2, but many examples with the reaction order greater than 1 are available. For example, Ferguson et al. [259] studied the deprotection of tert-butyloxycarbonyl (t-BOC) groups in poly(t-BOC-styrene sulfone) resists and reported exponents in the range of 1.2-1.8. The range of exponents was affected by the variations in temperature (always below T_g), PAG concentration, and type of PAG. Recently, Jung et al. [262–264] examined acid-catalyzed deprotection in two types of polymers: A poly(methyladamantyl methacrylate-co-γ-butyrolactone methacrylate) (PMAdMA-PGBLMA) resin with adamantyl protecting groups, and a poly(hydroxylstyrene-co-styrene-co-*tert*butyl methacrylate) (PHOST-PS-PTBMA) resin with *tert*butyl methacrylate protecting groups. These studies measured the resist sensitivity as a function of acid loading (photospeed), which is roughly proportional to deprotection rates at the reaction temperatures both below and above T_g. At temperatures below T_g, it was found that reducing the acid concentration by 1/2 would reduce the MAdMA-PGBLMA and PHOST-PS-PTBMA photospeeds by factors of 16 and 4, respectively. This result is in disagreement with first-order deprotection kinetics. In contrast, the same study detected first-order deprotection kinetics using laser spike annealing ($T >> T_g$). In

accordance with the available literature, the chemistry of the deprotection reaction cannot explain an increased reaction order. Based upon the data from Jung et al., it is likely that deprotection rates in polymer-based resists are controlled by the dynamical properties of the polymer resin [264].

The experimental results in this study provide a macroscopic deprotection rate exhibiting stronger-than-linear dependence on acid concentration,

$$K = k[\mathrm{H}^+]^n,\ n > 1. \tag{5.3}$$

It was determined that the exponent n was approximately 1.6 at 70°C, 1.5 at 80°C, and 1.5 at 90°C. To further demonstrate this behavior, Figure 5.1D reports all data for 70 °C on a master curve accounting for the nonlinear dependence of reaction rate on acid concentration. For example, the data for 10 wt% PAG upon multiplication by $10^{1.6}$ superimposes those points onto the 1 wt% PAG curve. This finding indicates that the underlying deprotection mechanism does not vary with acid concentration, but a simple linear rate law cannot explain the observed macroscopic behavior. Figure 5.1D also shows the model curve based on Eq. 5.2 (solid black line), and supports that an exponential decay of reacting groups does not describe the reaction kinetics. Apart from the observed slow reaction at very long times, a faster decrease in TBA groups was observed at short times. Previous studies of chemically-amplified resists have attributed such type of features to a competing thermolysis reaction [57, 261]. It should be noted that the PHOST-PTBA resin used in experimental studies is thermally-stable [229]. Keeping all these factors in mind, it is believed that a different microscopic model is needed for a quantitative description of the observed deprotection kinetics.

5.4.2 Fickian diffusion

For more than 30 years, the acid-catalyzed deprotection of glassy polymer films has been studied extensively. It is widely accepted that acid diffusion controls the macroscopic reaction rate, but the models based on Fickian diffusion are unable to adequately describe experimental data [115, 117]. A number of phenomenological diffusion models that reduce the acid transport rates with increasing extent-of-deprotection were developed. Many studies of acid transport in deprotected and protected polymers support this view, where extremely low diffusivity in the deprotected phase (10^{-16}-10^{-18} cm^2/s) is orders of magnitude less than the diffusivity in protected phase (10^{-12}-10^{-14} cm^2/s) [57, 113, 124]. One of such models suggests that volatile reaction products lead to creation of additional free volume and a subsequent desorption of these molecules with polymer relaxation decays the free volume to an equilibrium state [119]. While this hypothesis presents a plausible scenario, the model introduces several parameters that are difficult to estimate or measure. Furthermore, experiments reported that desorption is much faster than deprotection reaction in direct contrast to the volume–relaxation mechanism [265]. Some other studies have proposed a simple relationship between acid diffusivity and extent-of-reaction, such as a linear *increase* in diffusion rate with increasing deprotection level [56, 118]. Although this view is not supported by direct measurement of acid transport, such models appear to describe the image blur in a real photoresist. Owing to the difficulties in determination of an appropriate acid transport model, Fickian diffusion with a constant acid diffusivity is often employed to interpret experimental data [4, 54, 55]. To summarize, capturing both short-time and long-time behavior with the models of acid-catalyzed deprotection faces significant challenges. Therefore, different parameters based upon the aim of each study are introduced to capture the timescale of interest.

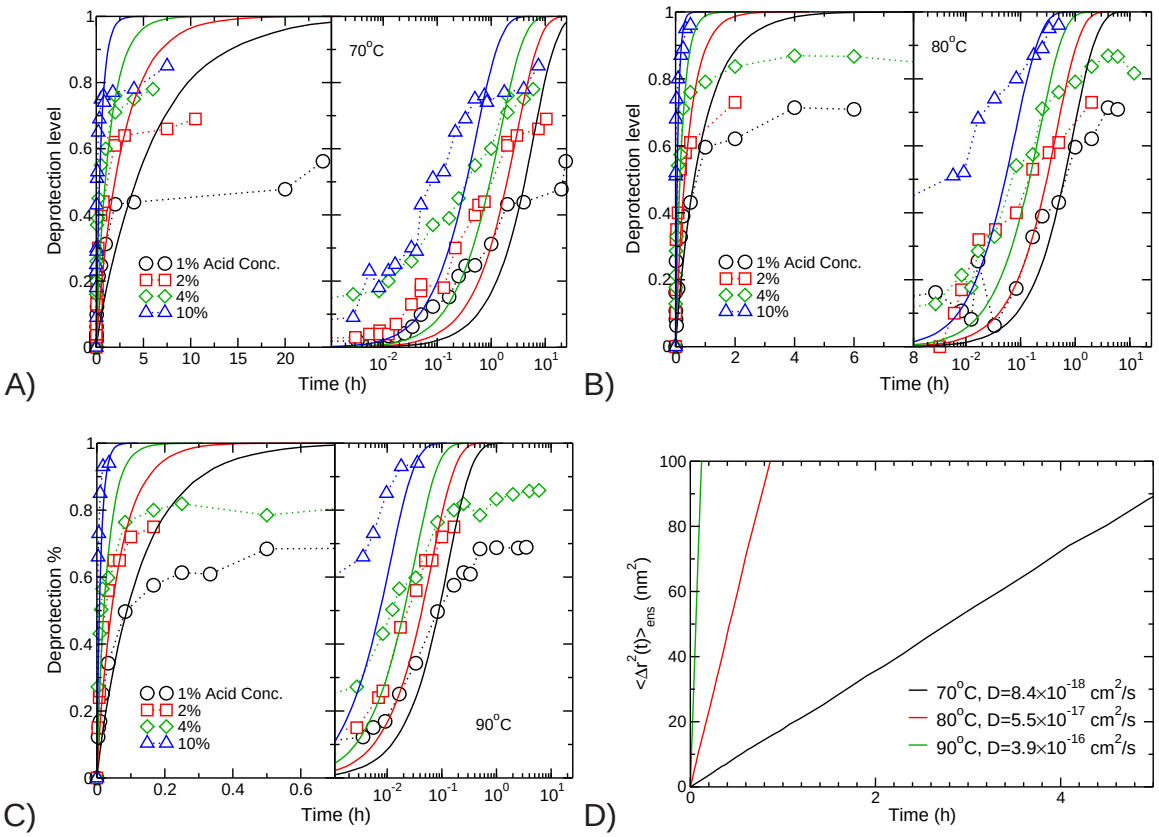

Figure 5.2: Deprotection profiles using Fickian diffusion model. A-C) Optimal D determined for the superimposed data at 1 wt%, and predicted profiles for higher acid loadings using the same D. D) Calculated mean-square displacement of acid molecules as a function of time. Reprinted with permission from Ref. 8. Copyright 2012 American Chemical Society.

In previous studies [57–59, 109, 116, 134], stochastic simulations have been used to describe reaction kinetics and acid transport in chemically-amplified resists. Using a lattice Kinetic Monte Carlo algorithm [139, 242, 243], a microscopic model based on an explicit description of acid molecules was defined that performs random walks with Gaussian statistics. In this algorithm, processes and associated transition probabilities are initialized for all lattice cells based upon the provided input. The probability to perform process *j* at lattice site *i* is given by

$$p_{ij} = \frac{\Gamma_{ij}}{\sum_{j=1}^{N_\mathrm{P}} \sum_{i=1}^{N_\mathrm{L}} \Gamma_{ij}} = \frac{\Gamma_{ij}}{\sum_{i=1}^{N_\mathrm{L}} \Gamma_{i,\mathrm{tot}}} = \frac{\Gamma_{ij}}{\Gamma_{\mathrm{tot}}}, \tag{5.4}$$

where Γ_{ij} is transition probability of process *j* at site i, $\Gamma_{i,tot}$ is sum of transition probabilities of all processes at site *i* and Γ_{tot} is sum of transition probabilities of all processes over all the lattice sites. Calculations of Γ_{tot} and $\Gamma_{i,tot}$ are done *a priori* i.e. before selecting the lattice cell and process to perform. Such processes associated with each lattice cell will be presented later in discussion of Figure 5.6. A lattice cell-process pair (*l*, *p*) is selected by using a uniformly generated random number $\zeta_1 \in (0, 1)$ following

$$\frac{\sum_{j=1}^{(p-1)} \sum_{i=1}^{l} \Gamma_{ij}}{\Gamma_{\text{tot}}} < \zeta_1 \leq \frac{\sum_{j=1}^{p} \sum_{i=1}^{l} \Gamma_{ij}}{\Gamma_{\text{tot}}}. \tag{5.5}$$

Another uniformly generated random number $\zeta_2 \in (0, 1)$ is used for the stochastic time increment proposed from the distribution

$$\Delta t = \frac{\ln(\zeta_2)}{\Gamma_{tot}}, \tag{5.6}$$

which corresponds to the exponential distribution represented by Eq. 5.1. This process is repeated until the desired simulation time is reached. Each function call in the optimization scheme performs one simulation of specified duration. The objective function defined by the sum of squared differences between experimental data and deprotection profile calculated from the simulations is minimized by following an acceptance or rejection based on the Metropolis criterion.

As discussed in the description in the Modeling Methods section, the diffusion coefficient D was the only adjustable parameter within the optimization scheme. The master curve described in Figure 5.1D was used for this refinement of D, rather than the individual data sets, which improved the algorithm's reliability and the simulation speed. After extracting the diffusivity D for low acid concentration (1 wt%), deprotection profiles for the higher acid loadings were created independently

Table 5.1: Parameters extracted for the Fickian diffusion and anomalous diffusion models. Reprinted with permission from Ref. 8. Copyright 2012 American Chemical Society.

Model Temperature	70°C	80°C	90°C
Fickian diffusion			
D (cm^2/sec)	8.4×10^{-18}	5.5×10^{-17}	3.9×10^{-16}
Anomalous diffusion			
τ (sec)	4.1×10^{-1}	7.6×10^{-2}	2.3×10^{-2}
γ	0.44	0.46	0.47
Anomalous diffusion with annihilation			
τ (sec)	7.8×10^{-1}	2.1×10^{-1}	6.6×10^{-2}
γ	0.53	0.59	0.67

using the *same* D. The values of D as a function of temperature are reported in Table 5.1, and Figure 5.2 shows the simulated deprotection levels obtained using Fickian diffusion against the experimental data. The extracted values of D are consistent with the acid mobility in deprotected resins reported in other works [121].

There are two aspects of these simulations that require further discussion. Referring to Figure 5.2, it can be observed that the simulated curve shows an exponential growth, which is very similar to the analytical model described by Eq. 5.2 and reported in Figure 5.1. Furthermore, the simulated deprotection rate shows a linear dependence on acid concentration. The apparent first-order dependence on acid concentration is attributed to independent random walks, where the mean-square displacement of acid molecules increases linearly with time and reproduces a Fickian diffusion coefficient as shown in Figure 5.2D. To summarize, while the simulated profiles are able to capture the correct time scale for deprotection, they still lack a quantitative agreement with the experimental data. It should be noticed that with the same D, profiles for different acid loadings are not captured.

5.4.3 Anomalous diffusion

As discussed in the previous section, the macroscopic deprotection rate cannot be captured by a simple microscopic Fickian diffusion mechanism. However, this discrepancy could be associated with an underlying hopping process that exhibits the features of anomalous diffusion [240, 245, 247–250]. The deviations from Fickian diffusion are consistent with the acid-anion hopping described by a waiting time distribution with long-tail kinetics [244]. A stretched exponential behavior exhibited in such type of dynamic processes resembles to probe diffusion in polymer glasses [141, 253, 266, 267]. A number of models [248, 254–256, 268] have been proposed to provide a quantitative description of anomalous diffusion in complex materials. For this study, the mathematical formalism of a continuous random walk, where sub-diffusive behavior originates from acid hopping described by a broad distribution of waiting times was employed [240, 269]. These waiting times were selected from the Pareto distribution [252],

$$\psi(t) = \frac{\gamma/\tau}{(1 + t/\tau)^{(1+\gamma)}}, \tag{5.7}$$

where γ is the anomalous exponent and τ corresponds to the characteristic time. This probability density function facilitates rapid sampling of waiting times between successive hopping events, and it satisfies the required long-time asymptotic scaling [245, 246, 252],

$$\psi(t) \propto \frac{\gamma}{\tau}\left(\frac{t}{\tau}\right)^{-1-\gamma}. \tag{5.8}$$

This algorithm was implemented following the literature with instantaneous reaction introduced when an acid translates to a non-deprotected lattice site [241, 252]. Reaction kinetics is solely controlled by acid transport, which is described with only two parameters, τ and γ. These parameters were determined for the

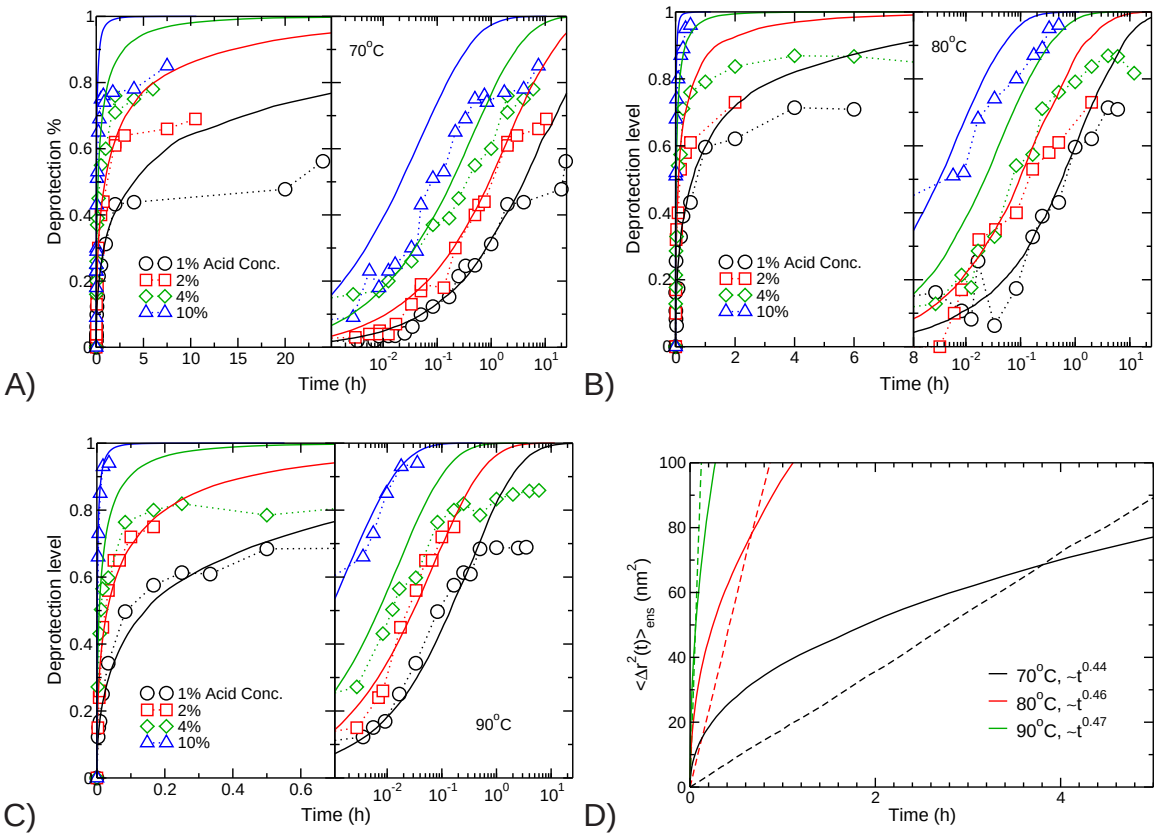

Figure 5.3: Deprotection profiles using the anomalous diffusion model. A-C) Optimal τ and γ determined for the superimposed data at 1 wt%, and predicted profiles for higher acid loadings using the same parameters. D) Calculated mean-square displacement of acid molecules as a function of time for anomalous diffusion compared with the Fickian model. Reprinted with permission from Ref. 8. Copyright 2012 American Chemical Society.

lowest acid concentration at each temperature, and then the profiles were predicted for the remaining acid concentrations. Figure 5.3 provides insight into the microscopic mechanism of the reaction process described by the model. At low concentrations and short times, the model of anomalous diffusion offers a quantitative description of bulk deprotection data consistent with the observed dependence on acid concentration. The subdiffusive character of acid transport serves as the underlying feature that generates this macroscopic behavior with the mean-square displacement

$$< \Delta r^2(t) >_{\text{ens}} \propto t^{\gamma}. \tag{5.9}$$

This subdiffusive behavior is depicted in Figure 5.3D for γ < 1. In order to extract these data, ensemble averaging without time averaging is required; since the latter could produce inhomogeneous Fickian diffusion [270]. The diffusion coefficient in subdiffusive model has a time dependence. However, using fractional derivatives a constant value can be defined [240]. Within the fractional derivative description, diffusion coefficient D_γ with values of 3.0×10^{-15}, 5.8×10^{-15}, and 5.3×10^{-14} cm^2/sec were extracted for 70°C, 80°C and 90°C, respectively [252,271]. It should be noted that the long-tail kinetics leads to a higher value of D, a finding that is similar to models based on Fickian diffusion with an acid-trapping process [54]. Nevertheless, it will be shown in the next section that an irreversible trapping reaction within a local volume is unable to capture the higher-order dependence on acid loading. The subdiffusive framework promotes the short-time displacements of acid molecules, but long-range diffusion is significantly penalized. These characteristics are required to capture our experimental data. Other works have also emphasized that models must include short-range fast dynamics while accounting for the extremely low diffusion coefficient in the deprotected polymer [113]. The chemistry involved in the reaction-diffusion process is not understood completely. However, a unique insight into the underlying physics is provided by the subdiffusive model, that offers a good description of the process with only two free parameters. Furthermore, this concept is consistent with the studies of inert probe diffusion in glasses [141, 253, 266, 267].

5.4.4 Acid-acid interactions

The microscopic view of subdiffusive transport discussed in the previous section is consistent with the experimental data for low acid concentrations and short reaction times. However, for higher acid loadings and longer reaction times, the subdiffusive model tends to over predict the extent-of-deprotection. It should be

noted that Fickian diffusion underestimated the deprotection level at short-times for all acid loadings, which is in contrast to subdiffusive model. While industrial processes tend to focus on lower acid loadings and short deprotection times, we sought to identify the cause of such deviations.

It may be hypothesized that acid loss will reduce the deprotection level at long times. Considering this fact, a selected acid molecule was attempted to be annihilated based on an additional rate in-between hopping intervals [251, 252]. This approach is similar to the phenomenological acid-trapping models proposed in earlier studies [4, 54, 55, 236, 260]. This mechanism was able to provide a quantitative description of the deprotection rates at low acid loadings (1 wt%), but the same values for τ, γ, and trapping rate could not capture the data for higher acid loadings. Specifically, it was observed that significant deviations between predicted and measured profiles exist at short times. These results are presented in Figure 5.4A. It is apparent that the loss mechanism must depend on acid concentration in addition to time to describe the experimental data quantitatively.

The model employed in this study projects a simplistic picture of acid molecules translating as "ghost" particles without any explicit interactions. Large ionic molecules within a volume of 1 nm^3 could invalidate this assumption. In addition, it is possible for reaction products to be present within their immediate environment. The effect of local composition on the reaction chemistry is unclear. Owing to these facts, a simple loss mechanism is proposed that does not require specification of new parameters: an acid molecule is deactivated if it hops into an already occupied lattice site. This mechanism is equivalent to the following instantaneous annihilation process,

$$H^+ + H^+ \rightarrow H^+. \tag{5.10}$$

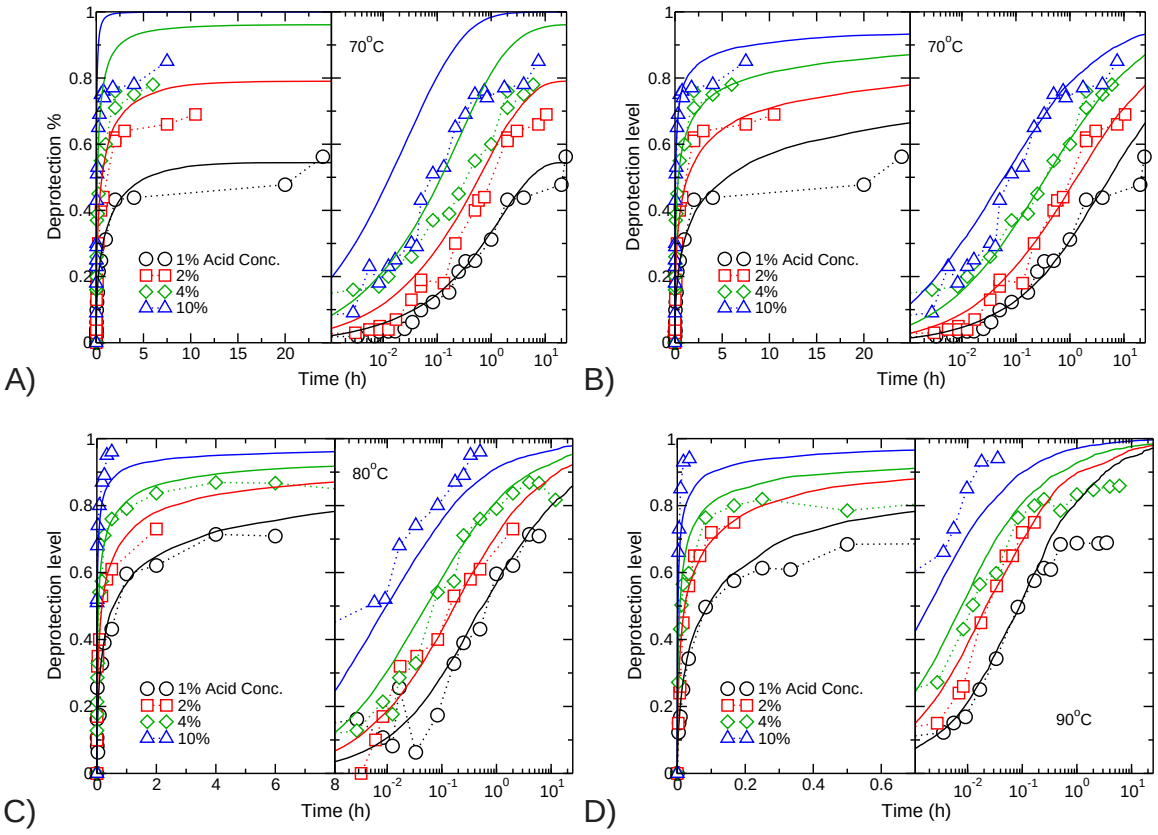

Figure 5.4: A) Anomalous diffusion model employing a linear acid loss $d\mathrm{H}^+/dt = -k[\mathrm{H}]$ with τ=0.26 sec, $\gamma = 0.44$ and $k = 5.5 \times 10^{-5}$ molecule/sec. B-D) Anomalous diffusion model with partial deactivation upon acid-acid encounters. Reprinted with permission from Ref. 8. Copyright 2012 American Chemical Society.

This process occurs when acid molecules exist within 1 nm of each other, which is equal to the lattice grid and an implicit feature of this algorithm. Use of this simple approach can provide quantitatively description of all experimental data at 1, 2 and 4 wt% acid loading with two parameters for the distribution of waiting times. The results based on instantaneous annihilation mechanism are summarized in Figure 5.4. It should be noted that small deviations persist for the 10 wt% loading, but this may be attributed to the initial conditions: it is possible to have non-uniform spatial distribution of the PAG at such high concentrations [58], or it may be plausible that a plasticizing effect leads to faster deprotection rates at the highest temperatures [272]. Two data sets for 90°C exhibit a plateau at long times

(ca. 1-10 hours). These features are not captured by the acid depletion model. The reason behind this behavior is unknown. It should be noted that similar trends have been observed in other studies that incorporated a base quencher [121, 273]. While the resist formula in the experiments does not contain base additives, the possibility of airborne contaminants that were slowly adsorbed onto the surface of these films and accidentally deactivated the catalyst with a very slow timescale cannot be denied.

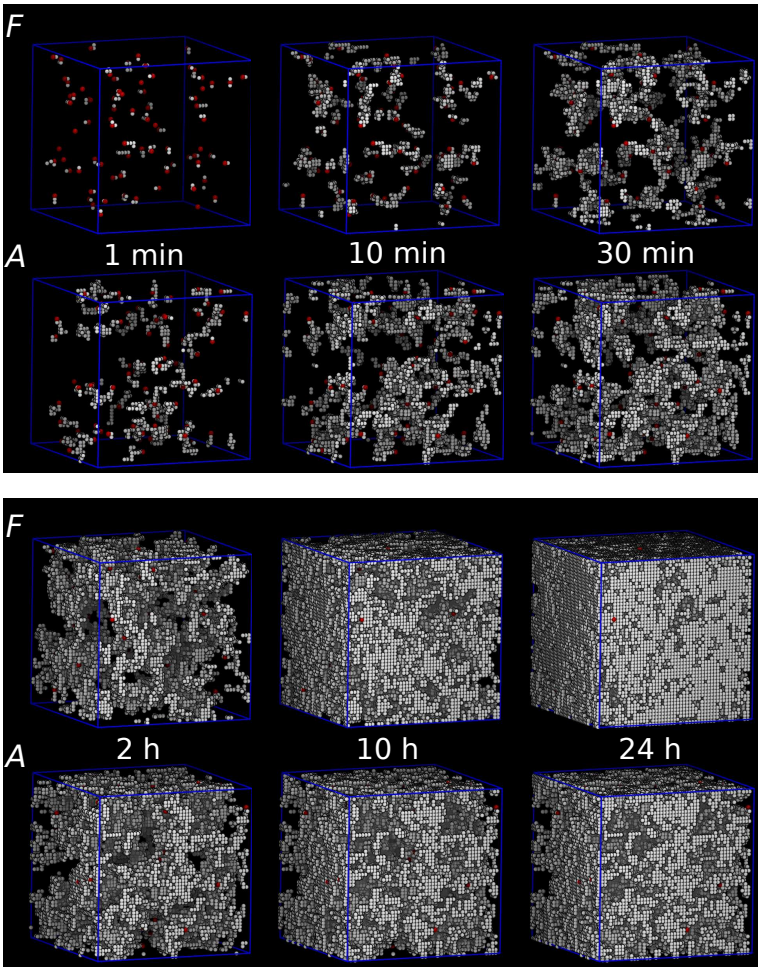

Figure 5.5: Snapshots of a 0.05 wt% acid system at 80°C for the Fickian model (F) and anomalous diffusion with acid-acid interactions (A). Extracted parameters are summarized in Table 5.1. Initial acid positions are rendered in red color, and reacted material is represented in white color. Reprinted with permission from Ref. 8. Copyright 2012 American Chemical Society.

The origin of the proposed phenomenological acid depletion is unclear. The reaction denoted by Eq. 5.10 may capture aggregation (with collective movement of aggregates) [233], or partial deactivation of catalyst due to shift in reaction equilibrium caused by an increased local acid concentration [121]. Currently, direct measurements to support any of these mechanisms do not exist. However, this model leads to deactivation of most of the catalyst ultimately, and aggregation alone fails to explain this behavior due to absence of large-scale phase separation in microscopy measurements of the resist films.

To highlight the differences between the Fickian diffusion model and subdiffusive behavior, the system was modeled with a very low initial concentration of acid (0.05 wt%) to facilitate visualization of the process. It should be noted that acid-acid interactions are not relevant in this case. The evolution of this system at 80°C is illustrated in Figure 5.5, where snapshots from the simulations based on the best-fit parameters for Fickian and anomalous diffusion (with annihilation) as reported in Table 5.1 are presented. Within 10 min, the anomalous diffusion model predicts 3% (volume) of reacted material, while the Fickian model predicts only 1%. After 2 hours, almost 11% of the material has undergone deprotection irrespective of the model used. Furthermore, the Fickian model predicts 70% and anomalous transport model predict 32% conversion after 24 hours.

5.4.5 Interfacial effects in Chemically-Amplified Resists

So far this chapter focused on the development of a model that is able to predict deprotection kinetics in quantitative agreement with the experimental data. One of the outstanding challenges in the semiconductor fabrication employing CA resists arises due to the mechanically unstable narrow features, which can be overcome by application of the ultrathin films. In the ultrathin films, interfacial effects

near substrate and free surface become important [50] and significantly affect image formation [52]. Estimation of such effects requires incorporation of existing knowledge of interfacial phenomena in thin films [60, 61] in the simulation schemes discussed in earlier sections.

It is emphasized that this section is a proof–of–concept to demonstrate that lattice simulations can incorporate spatially variable parameters, which can be instrumental in capturing the features arising in ultrathin film resists. These features are attributed to film thickness dependent acid diffusion and acid segregation at the interface. In the previous studies [4, 54, 55, 236, 260], acid loss due to trapping of photoacid by deprotected polymer was used along with reaction and diffusion processes. Following a similar approach in this section, three types of processes namely diffusion, reaction and trapping were modeled. The lattice Kinetic Monte Carlo algorithm discussed in the previous sections was employed. Diffusion probabilities were kept same as experimentally established diffusivity of acid molecules in polymer film following a Fickian model. As shown in Figure 5.6, deprotection reaction converts a protected cell (green) to a deprotected cell (white) in presence of an acid molecule (blue) with a microscopic reaction rate k_{P}. Trapping reaction [119] occurs at a deprotected non-trapping cell (white), which converts deprotected non-trapping cell into a deprotected trapping cell (red) with a microscopic rate k_{T}. Acid molecules transiting to deprotected trapping cell are immobilized instantaneously.

Applicability of the lattice Kinetic Monte Carlo algorithm for modeling CA resists was established by reproducing the time evolution of deprotection profiles during post-exposure bake (PEB) of poly(methyladamantyl methacrylate) (PMAdMA) films with di(*tert* - butylphenyl) iodonium perfluorooctanesulfonate (DTBPI-PFOS) photo acid generator (PAG) [4]. A 3D lattice (140 cells $\times$ 50 cells $\times$ 80 cells) was used with each cell representing a volume of 1 nm $\times$ 1 nm $\times$ 1 nm. In Figure 5.7A, symbols show experimental results of Vogt et al. [4] and solid lines with similar color

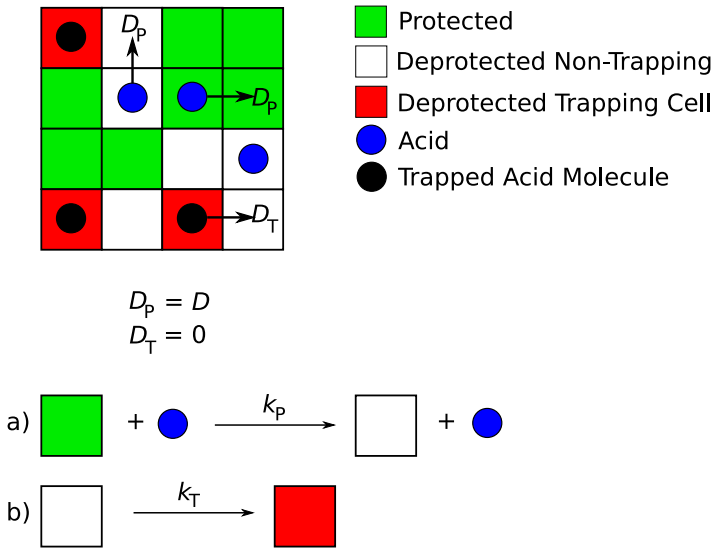

Figure 5.6: Processes used in kinetic Monte Carlo simulations of CA resists.

coding show results from the lattice simulations. Incorporation of acid-diffusion, deprotection reaction and acid-trapping helps in reproducing self limiting behavior of reaction-diffusion front in quantitative agreement with the experiments. however, if different acid loadings are considered, these parameters need to be reoptimized. It is observed that trapping process is important for achieving self limiting behavior. It should be noted that previous sections outlined that behavior is not self limiting, but for this first testing the interfacial effects, this concept is adopted in this section.

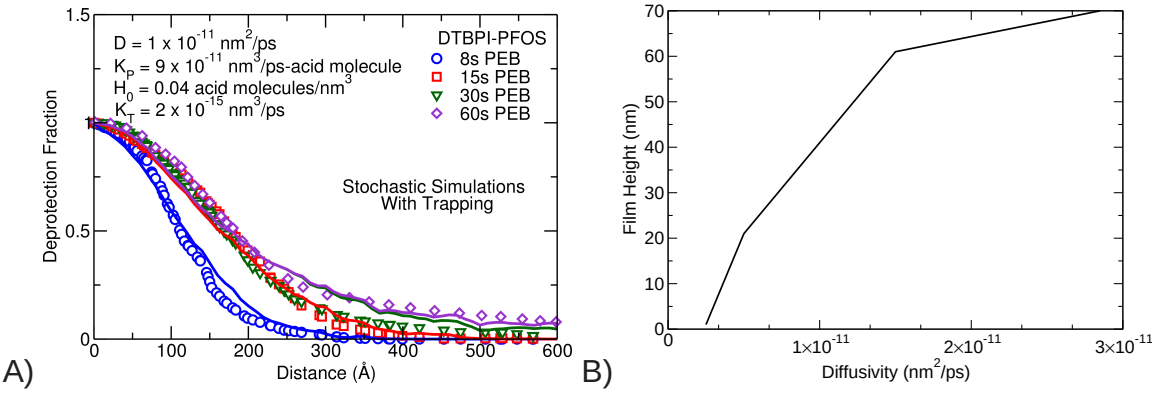

Figure 5.7: A) Deprotection fraction from stochastic simulations and experiments [4]. B) Spatial variation in diffusivity for stochastic simulations.

For incorporating interfacial effects in ultrathin films, a spatially variable diffusivity profile (Figure 5.7B) was implemented in simulation models. Moreover, initial acid distribution was generated from a probability distribution obtained by convolution of a multidimensional Heaviside step function and Gaussian probability distribution function.

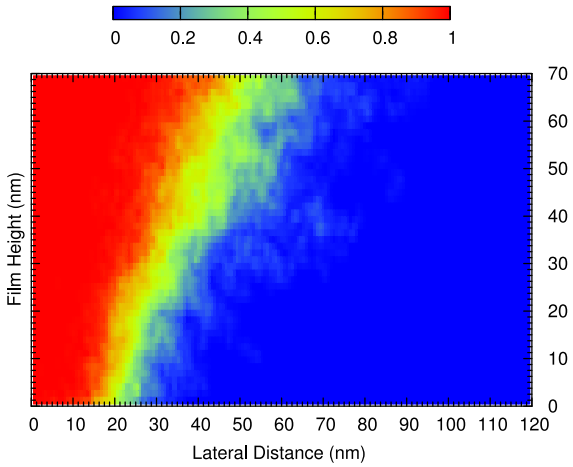

Figure 5.8: 2D map showing variation in fraction of deprotected polymer at 20s of PEB. Red color depicts higher levels of deprotection.

The experimental deprotected feature shapes were based upon the experimental data from using poly(hydroxystyrene-*co*-*tert*-butyl acrylate) or P(HOSt-*co*-tBA) thin films with triphenylsulfonium purfluoro-1-butanosulfonate (TPS-PFBS) PAG at 90°C. 2D maps of spatial variation in deprotection levels obtained from lattice simulations are shown in Figure 5.8. Figure 5.9A shows that for each film height z, deprotection profile exhibits a decay region, where normalized deprotection level varies from 1 to 0. The profiles in decay region were fitted against exponential function

$$C(x) = \exp\left(\frac{-x^2}{A_0}\right), \tag{5.11}$$

where A_0 is a fit parameter and $C(x)$ is normalized deprotection fraction. The

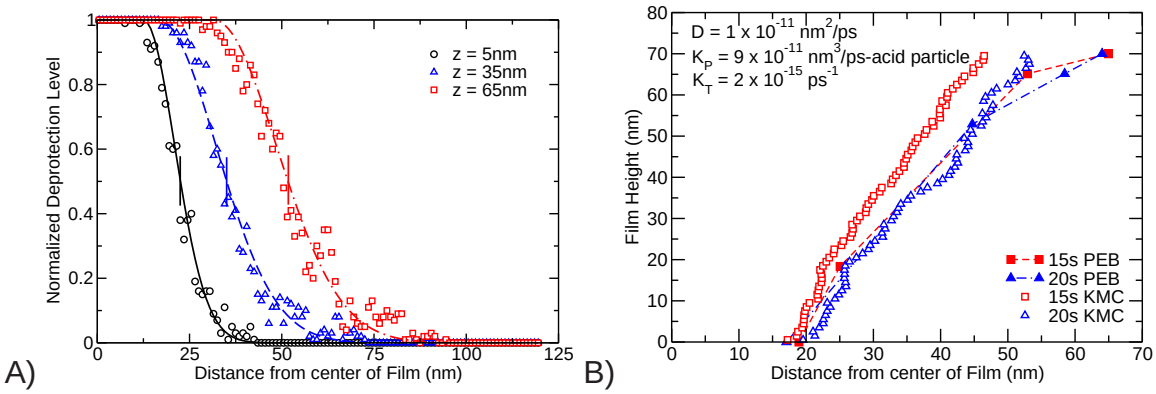

Figure 5.9: A) Normalized deprotection profiles at three film heights (empty symbols) and exponential fits (lines) in the decay region. B) Experimental deprotected feature shape profiles (dotted lines and filled symbols) and simulated shape profiles (empty symbols).

equideprotection point obtained from these fits was used as a measure of deprotected feature width at corresponding film height. The deprotected feature shapes extracted by following the above methodology are shown in Figure 5.9B.

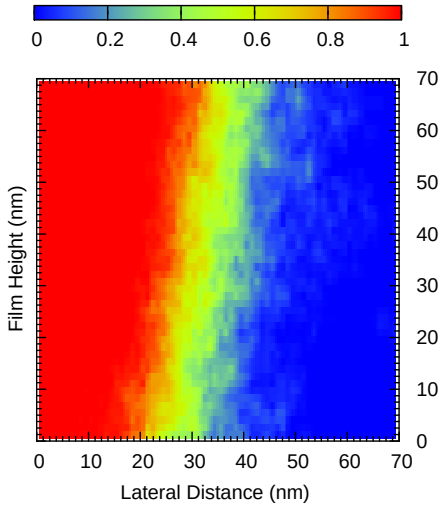

Figure 5.10: 2D density map showing spatial variation in deprotection fraction at 15s PEB upon incorporation of excess surface acid concentration. Red color depicts higher levels of deprotection.

The simulated feature shapes are in good agreement with the feature shapes obtained from experimental data. Also, introduction of spatially variable diffusivity

assists in capturing the narrow feature shape near the substrate and broader feature shape near the free surface of ultra-thin film. To conclude, lattice simulations can provide a tool for capturing heterogeneity in diffusion rates arising from the interfacial effects, which enables prediction of the levels of deprotection and shapes of deprotected features in CA resists in both qualitative and quantitative agreement with experiments at fine spatial resolution. For testing the effect of segregation of acid to the free surface, three regions were defined within the thin film: 1) proximal region within 20 nm of substrate, 2) free surface region within 10 nm of free surface and 3) remaining bulk region. To study the effect of surface acid excess, an initial lattice configuration with acid density of 0.25 $\times H_0$, 2.5 $\times H_0$ and H_0 (bulk acid density H_0 = 0.04 acid-molecules/nm^3) in region 1, 2 and 3 respectively was used. Such variation in acid density produces linearly increasing feature shape (Figure 5.10) with nearly constant layer of partial deprotection.

5.5 Conclusions

There is substantial demand for quantitative predictions of resolution limits in chemically-amplified photoresists. Insight from macroscopic models applied to nanoscale lithography is often qualitative rather than quantitative in nature. Such models attempt to predict acid mobility based on the average material composition, and additional phenomenological processes such as free volume generation, acid trapping, or thermodynamic equilibria are employed to capture the temporal deprotection rates. However, glasses are characterized by dynamic heterogeneities, and incorporation of fluctuations at microscopic length scales into Fickian diffusion models (or in variants based on local composition) is not straightforward.

In this chapter, the results of acid-catalyzed deprotection of a glassy polymer resin obtained with infrared absorbance spectroscopy were modeled using

stochastic simulations. The experimental data were interpreted with a model that explicitly accounts for acid transport and introduces local heterogeneities through a non-exponential distribution of waiting times between successive hopping events. A different view that supports the anomalous diffusion behavior is a hopping process with binding-unbinding events at energetic or geometric traps [240]. Thus, this simplified mathematical model provides the foundation for explicit examination of acid transport without introducing difficult to capture details of the changing environment at local length scales. It is found that subdiffusive behavior with long-tail kinetics is able to capture key attributes of the observed deprotection rate and offers a near-quantitative description of macroscopic deprotection rates. Only two parameters need to be specified to obtain such quantitative description. The same model parameters can describe the deprotection level for different acid concentrations, and their variation with temperature follows the expected behavior. For high acid loadings, it was found necessary to include acid-acid interactions that deplete the effective acid concentration. While the exact underlying mechanism of such acid depletion is unclear, it is to be believed that other factors are of greater interest for future studies. For example, study of changes in acid-counterion size, polymer chemistry, resist film thickness, and proximity to T_g would highlight how the polymer's dynamical properties affect reaction front propagation.

Finally, proof–of–concept simulations were employed to show the efficacy of lattice simulations in capturing the interfacial effects in the CA resists. These simulations coupled with subdiffusive behavior and acid-acid interactions can be employed to predict the pattern shapes. In future studies, these results will help in gaining insight about the changes in the rate of reaction due to interfacial phenomena. The next chapter will consider phenomena, where interfacial interactions can actually determine the size and shape of the growing surface. Specifically, crystallization/growth rates of zeolites are manipulated by using growth modifying

molecules, which are hypothesized to have their efficacy due to preferential binding to a particular crystal surface. This hypothesis is evaluated by employing molecular simulations.

Chapter 6 Interactions of Zeolite Growth Modifiers with Model Surfaces

6.1 Introduction

Zeolites are used in a number of industrial applications, e.g., ion exchange, separation processes, and catalysis. The specific pore size of the zeolites provides them shape selectivity for the separation processes. As catalysts, zeolites have been used in petroleum refineries [274], environmental catalysts [62], and more recently in the production of bio-fuels. It has been shown that carefully synthesized zeolite catalysts can have significant impact on the yield of fluid catalytic cracking [274]. On the other hand, irregular pore structure and defects in the zeolite channels may be attributed to poor shape selectivity and diffusion limitation [62]. Considering these factors, controlling the morphology of zeolites during the synthesis is vital for the optimum performance of these materials.

Zeolite morphology should be tailored to suit the target application. Most of the times, control of zeolite morphology targets at minimizing diffusion path length, increasing surface area and adjusting the orientation of the channels. Due to extensive commercial application, it is important to develop methods of morphology control, that are cost effective and scalable. In the pursuit of meeting the goal of affordable morphology control, Lupulescu and Rimer [1] demonstrated that certain molecules termed as zeolite growth modifiers (ZGM) can be instrumental in altering the growth of zeolites. In their work, they used molecules such as D-Arginine (D-Arg), spermine, and triethylenetetramine (TETA) to control the growth of silicalite-1

zeolites. Control experiments (in absence of any growth modifier) were performed at 160°C temperature, autogenous pressure and a pH of 12.7 in presence of structure directing agent (SDA) tetrapropylammonium (TPA^+). Tetraethylorthosilicate (TEOS) served as the silica source. Normally, silicalite-1 crystals show the fastest growth along c-axis or [0 0 1] direction followed by [1 0 0] and [0 1 0] directions. The comparison of silicalite-1 crystals produced by control experiments with the crystals obtained in the presence of ZGM molecules showed significant alteration in crystal growth. For example, addition of spermine produced silicalite-1 crystals with a thickness along the b-axis (along the less tortuous [0 1 0] channels) one third of the thickness observed in the control experiments. It was also noted that D-Arg is effective in inhibiting growth in [1 0 1] direction.

It is hypothesized that the growth inhibiting capability of ZGM molecules is due to their preferential binding to a particular crystal plane, which inhibits the crystal growth perpendicular to the specific crystal plane. The molecular mechanism and thermodynamic factors that provide ZGM the capability of inhibiting zeolite growth are unclear. Molecular simulations have been employed in a number of studies to probe adsorption of molecules in zeolites by using molecular dynamics (MD) [146–151] or Monte Carlo (MC) simulations [152–159]. Most of these studies have targeted the adsorption and diffusion of the alkanes and alcohols inside the zeolite channels, while some studies focusing on the outer surface of zeolites are also available in literature [151, 160–165]. In a recent study, Salvalaglio et al. [170] employed well-tempered metadynamics [171] to understand the molecular mechanism of urea crystal growth in the presence of additives such as biuret and acetone. Following a similar approach, the mechanism of ZGM facilitated zeolite synthesis can be examined by using molecular level information of these systems. In this chapter, molecular simulations are employed for elucidating the origin of growth

inhibition and the hypothesis of preferential binding is tested by evaluation of quantitative thermodynamic parameters.

6.2 Models and Systems Studied

Silicalite-1 (MFI framework) slabs were employed to study the binding affinity of D-Arg molecules to specific MFI surfaces. The silicalite-1 slabs (without defects) were created using an orthorhombic $Pnma$ crystallographic structure by using the initial atomic positions determined from crystallographic experimental data published by van Koningsveld et al. [275]. The crystallographic parameters were a = 20.022 Å b = 19.899 Å and c = 13.383 Å , where b-axis gives the direction of the straight channels (along [0 1 0] direction).

One of the important consideration in simulation studies of zeolites is whether a rigid framework should be used or the structure should be allowed to remain flexible [147, 149, 151, 152, 166–168]. Smirnov [147] studied adsorption and diffusion of methane in silicalite-1 by MD simulations considering both rigid and flexible frameworks and concluded that framework flexibility does not alter methane adsorption significantly. Similar results were showed for the adsorption of Argon in silicalite-1 [167]. On the other hand, Hughes et al. [168] probed desalination of water using zeolites. The study focused on thermodynamics of salt rejection by accessing the interactions of chloride ions with zeolite environment. They emphasized that framework flexibility is critical to the studies involving small molecules in zeolite channels. Despite such claims, it was noted that flexible frameworks may overestimate diffusion coefficients for small molecules, worse than the predictions obtained from rigid framework [166]. Considering the size of ZGM molecule of interest (D-Arg, $\approx$ 1 nm), it was deemed appropriate to use a rigid framework. The silicalite-1 surfaces were prepared using the crystallographic coordinates and their

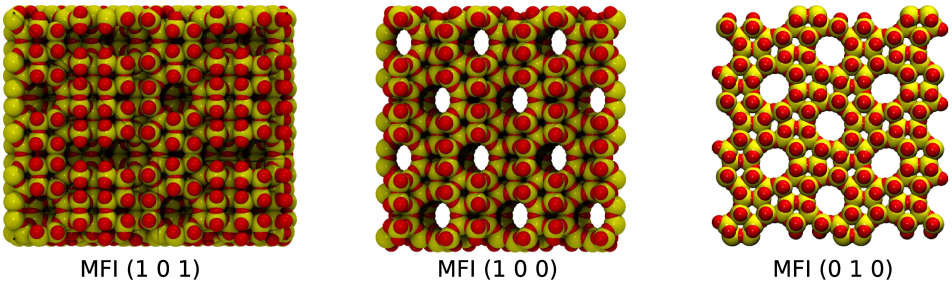

Figure 6.1: Snapshots presenting zeolite surfaces considered in this chapter.

consistency with the experimentally observed stable crystal surfaces [169] was validated. Figure 6.1 shows the snapshots of the silicalite-1 surfaces studied in this chapter.

All surface silicon atoms were saturated by adding oxygens to satisfy their valency. It should be noted that silanol groups have a reported pK_a value of $\approx$ 9 [276]. For the synthesis pH of 12.7, this translates to one undissociated silanol group in every 5,000 surface silanols. Considering this, it was assumed that all surface silanols on silicalite-1 surface are dissociated. The non-bonded interaction parameters for the Si and O atoms were adopted from the force field prescribed by Nicholas et al. [277]. The interactions of ZGM molecule (D-Arg) were modeled by `GROMOS53A6` forcefield (Figure 6.2A) [278], whereas a simple point charge (SPC) model was used for modeling the interactions of water [279]. For the D-Arg molecule, the protonation states of the carboxylic group (pK_a = 2.17 [276]), α-amino group (pK_a = 9.04 [276]) and guanidinium group (pK_a = 12.48 [276]) were found to be dominated by deprotonated states. The simulation systems contained a single D-Arg molecule in $\approx$ 3,000 water molecules. The water layer extended $\approx$ 5 nm from the zeolite surface (represented by surface oxygen atoms). This width of water layer was sufficient to observe reasonable span of bulk-like water density (Figure 6.2B). The charge neutrality of the systems was maintained by introducing Na^+ ions as performed in previous work [280]. The simulation system was large

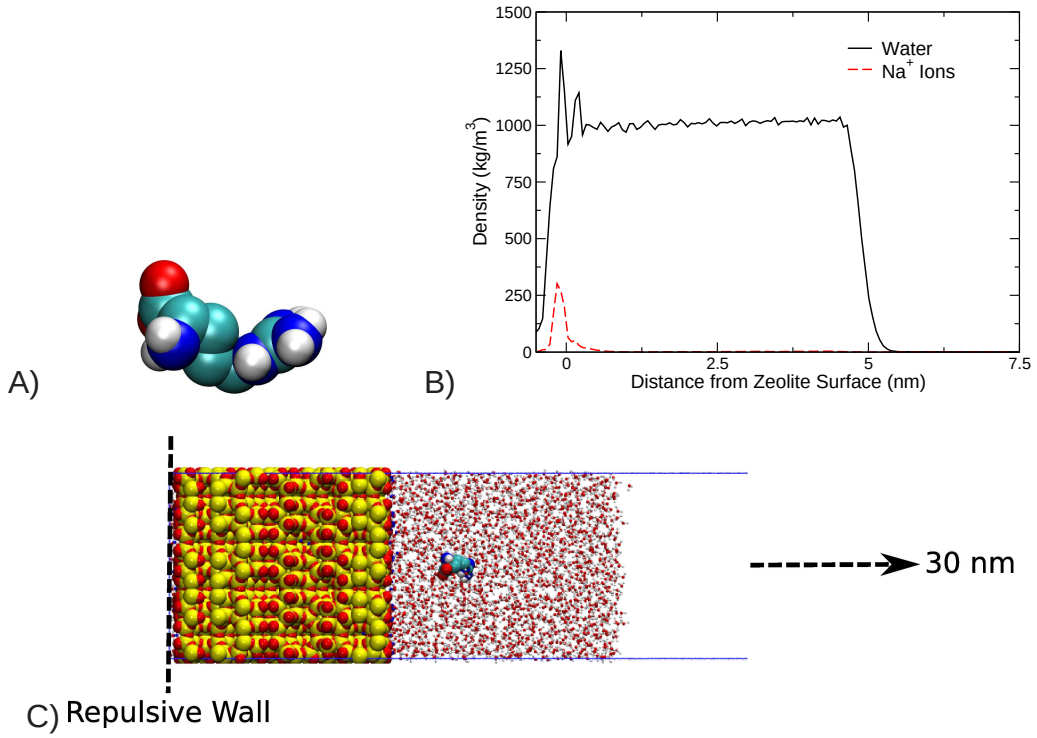

Figure 6.2: A) Snapshot of a D-Arginine molecule. B) Density of water and Na^{+} ions in MFI (1 0 1) system as function of distance from the surface oxygen atoms, and C) snapshot of a representative simulation box.

enough along the axis perpendicular to the zeolite surface in order to avoid finite size effects. In addition, a repulsive wall was introduced at z = 0 to avoid any water escaping from the lower end of the zeolite framework (Figure 6.2C).

6.3 Simulation Methodology

6.3.1 Standard Molecular Dynamics Simulations

Atomistic NVT MD simulations for 200 ns employing the simulation setup discussed in the previous section were performed using Gromacs v4.5.5 [204]. The non-bonded interactions were smoothly switched to zero between 1.0 nm and 1.2 nm. Electrostatic interactions were treated by Particle Mesh Ewald (PME)

method [281] with a correction for slab geometry [282]. The real-space part of the Ewald sum was also smoothly switched to zero between 1.0 nm and 1.2 nm. All bonds were constrained by the LINCS algorithm [283] and a timestep of 2 fs was used for integrating the equations of motion. Temperature was maintained at 298 K by applying the velocity-rescaling temperature coupling with a time constant of 1 ps [223]. The results obtained from the analysis of the MD simulations are discussed in the later section.

6.3.2 Well-Tempered Metadynamics

Quantitative insight of the binding affinity between the ZGM and zeolite surfaces can be obtained by free energy calculations. For accurate estimate of free energy, rigorous sampling of an order parameter or collective variable (CV) is required. Standard molecular dynamics simulations require extensive simulation times to accomplish such sampling, which is not within reach of current computational power. To alleviate such challenges is metadynamics [284], in which the system evolution is biased by a history dependent potential. This potential is constructed as the sum of Gaussian functions deposited along the simulation trajectory in the CVs space. Convergence of the free energy profile may not be achieved within standard metadynamics [171]. To address such issues present in the metadynamics method, Barducci et al. [171] proposed well-tempered metadynamics. For a system described by a set of microscopic coordinates q, free energy surface (FES) as a function of a set of CV $s(q)$ can be written as

$$F(s) = -T \lim_{t \to \infty} \ln N(s,t), \tag{6.1}$$

where $N(s,t)$ is the histogram of variable s obtained from an unbiased simulation. The sampling can be accelerated by applying a history-dependent potential

$$V(s,t) = \Delta T \ln\left(1 + \frac{\omega N(s,t)}{\Delta T}\right), \tag{6.2}$$

where ω has dimensions of energy rate, ΔT is temperature and $N(s,t)$ are histograms accumulated from simulations. The bias potential given in Eq. 6.2 disfavors the more frequently visited configuration and enhances the sampling of configurations, which have not been visited during the course of simulation. In practice, the FES can be estimated by using Eq. 6.2 as

$$\tilde{F}(s,t) = -(T + \Delta T) \ln\left(1 + \frac{\omega N(s,t)}{\Delta T}\right). \tag{6.3}$$

For the limit $\Delta T \rightarrow \infty$, Eq. 6.3 yields $\tilde{F}(s,t)$ = -$V(s,t)$ and the standard metadynamics algorithm is recovered. The Gaussian height w is calculated by

$$w = \omega \exp\left(-\frac{V(s,t)}{\Delta T}\right) \tau_G, \tag{6.4}$$

where τ_G is the time interval at which the Gaussians are deposited. For the simulation to converge, the Gaussian height has to reach zero. A reweighing algorithm [285] available in the literature can be used for estimating the FES. The well-tempered metadynamics algorithm is implemented in PLUMED [286], which is freely available as a plug-in to Gromacs. For the simulations performed in this chapter, PLUMED v1.3.0 was used with Gromacs v4.5.5. The simulation conditions and interactions in the well-tempered metadynamics simulations were kept as in the standard MD simulations. The simulation time for each system exceeded 150 ns. The results from these simulations are discussed in the later section.

6.4 Results and Discussion

6.4.1 Standard Molecular Dynamics Simulations

The simulation trajectories obtained from MD simulations were analyzed to find possible clues of affinity between the the growth inhibitor molecule D-Arg and silicalite-1 surfaces. The first attempt in this direction was the estimation of the residence time of the molecules at the crystal surface. To characterize D-Arg molecules "interacting" with the zeolite surface, the distance of molecule COM along z-axis from the zeolite surface oxygen atoms, $d_{\text{ARGN-COM}}$ was calculated (Figure 6.3A). Any molecule with $d_{\text{ARGN-COM}}$ < 1 nm was considered to be interacting with the crystal surface. Figure 6.3B shows evolution of $d_{\text{ARGN-COM}}$ with the simulation time for the three systems studied. For the MFI (1 0 1) and MFI (0 1 0) surfaces, inhibitor molecule finds suitable binding locations and remains on the crystal surface for the rest of the simulation trajectory. For the MFI (1 0 0) surface, the D-Arg molecule approaches and departs the surface a number of time. However, the condition $d_{\text{ARGN-COM}}$ < 1 nm is satisfied very few times during the 200 ns simulation duration. While it may be tempting to derive a conclusion that MFI (1 0 0) surface is not favorable for binding, surface residence alone should not be taken as a sole indicator of binding affinity as will be discussed later in this section.

In addition to surface residence, the number of hydrogen bonds formed by the inhibitor molecule with the surface oxygen atoms were also calculated as a function of time. A hydrogen bond is defined using a conventional distance criteria of 0.35 nm and 30° angle. As can be clearly seen from Figure 6.3C, inhibitor molecule interacting with the MFI (1 0 1) forms on an average $\sim$ 3 hydrogen bonds. A closer comparison of Figure 6.3B and 6.3C reveals that between 80 ns to 120 ns, this average shifts closer to $\sim$ 4 hydrogen bonds. At the same time $d_{\text{ARGN-COM}} \approx$ 0.3 nm

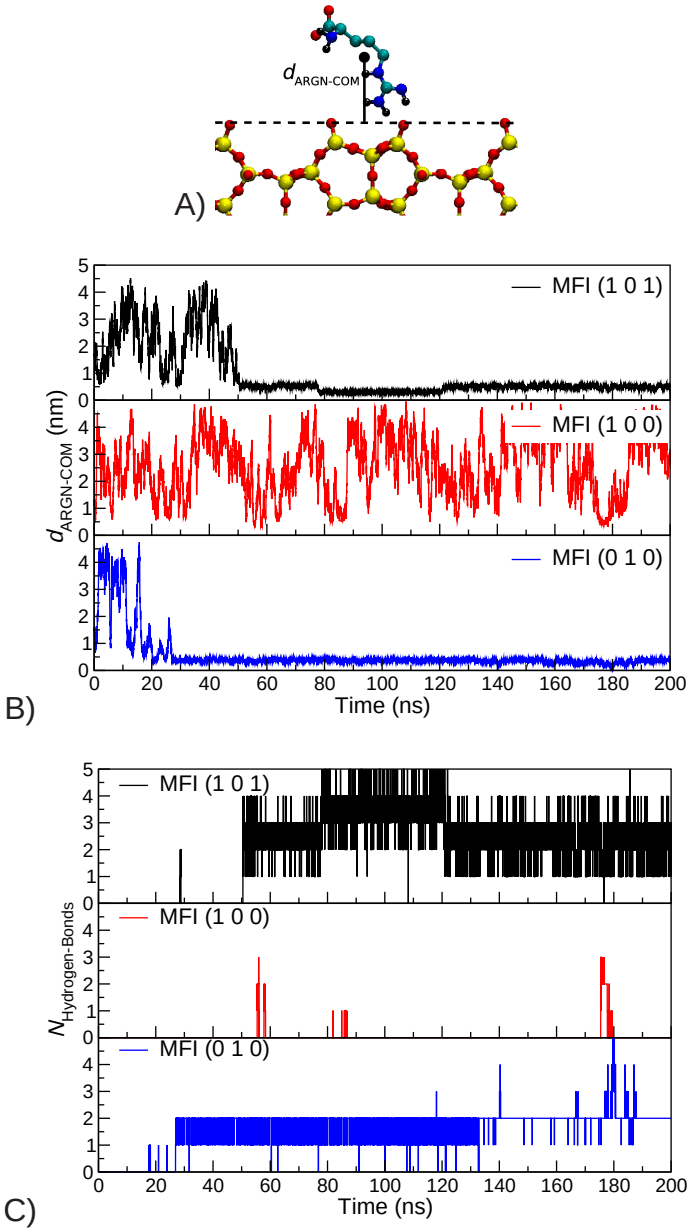

Figure 6.3: A) Schematics depicting the D-Arginine COM distance from the surface oxygen atoms $d_{\text{ARGN-COM}}$, B) position of D-Arginine COM as a function of time during standard MD simulations, and C) number of hydrogen bonds formed between D-Arginine molecule and zeolite surfaces.

and significantly smaller amplitude of fluctuations in $d_{\text{ARGN-COM}}$ are observed. In contrast to this for the MFI (0 1 0) surface, average number of the hydrogen bonds remains close to 2 and $d_{\text{ARGN-COM}} \approx 0.35$ nm with almost consistent fluctuations in

the $d_{\text{ARGN-COM}}$ values. Unfortunately, for the MFI (1 0 0) surface, no such information can be obtained due to very limited statistics. Based upon these observations two things can be hypothesized. First, D-Arg at the MFI (1 0 1) surface appears to interact with the surface stronger between the 80 ns and 120 ns of the simulation trajectory. In this duration, molecule is able to form 4 (at times 5) hydrogen bonds, which indicates that D-Arg at the MFI (1 0 1) surface exhibits two preferable binding conformations. One of these conformations shows stronger affinity indicated by smaller fluctuations and more number of hydrogen bonds. Second, there appears to be one favorable binding conformation with 2 hydrogen bonds for the MFI (0 1 0) surface.

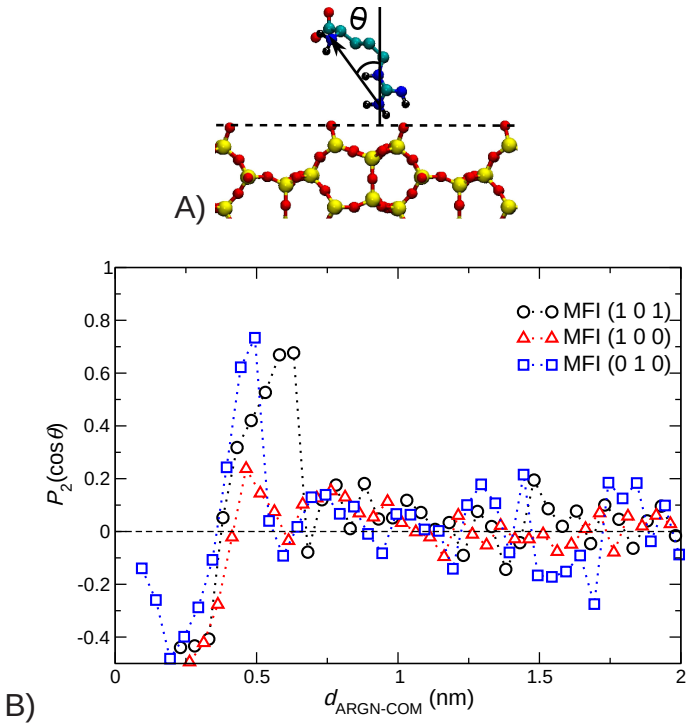

Figure 6.4: A) Schematics depicting the D-Arginine orientation, and B) orientation of D-Arginine as a function of $d_{\text{ARGN-COM}}$ during standard MD simulations.

In order to further investigate the difference in the number of hydrogen bonds formed by the inhibitor molecule, the orientation of molecules in the proximity of zeolite surfaces was investigated. The orientation of D-Arg molecule was defined

by the angle between a vector joining the nitrogen atoms of the NH_2 of α-amino group and guanidinium group with the z-axis (depicted by θ in Figure 6.4A). The second Legendre polynomial is subsequently defined by

$$P_2(\cos\theta) = (3 < \cos^2\theta > -1)/2. \tag{6.5}$$

$P_2(\cos\theta)$ values of -0.5, 0 and 1 represent parallel, random and normal to surface orientations respectively. It can be observed from Figure 6.4B that the molecule orients parallel to the MFI (1 0 1) surface at $d_{\text{ARGN-COM}} \approx$ 0.3 nm. This parallel to surface orientation enables D-Arg to form 3-5 hydrogen bonds with the surface at this COM separation. At larger separations, the orientation of D-Arg molecule at the MFI (1 0 1) surface first becomes random and then a tendency of close to normal orientation is observed at $d_{\text{ARGN-COM}} \approx$ 0.6 nm. Thus fewer hydrogen bonds can be formed at larger separations. This finding about D-Arg orientation is consistent with the observations made in Figure 6.3C. On the other hand, at the MFI (0 1 0) surface, a parallel orientation is observed at $d_{\text{ARGN-COM}} \approx$ 0.2 nm and then a gradual transition to random orientation occurs at the distance of $d_{\text{ARGN-COM}} \approx$ 0.35 nm. This random orientation of D-Arg at the MFI (0 1 0) surface is consistent with $\approx$ 2 hydrogen bonds observed in Figure 6.3C. No such observations were possible for the MFI (1 0 0) system due to limited statistics.

While above observations provide an initial explanation of the stronger affinity between D-Arg and the MFI (1 0 1) surface and provide some support to the hypothesis of preferential binding, the extent of sampling remains questionable. To probe sampling along the lateral surface of zeolite, 2-dimensional probability density maps of inhibitor atom locations were prepared from the MD simulation trajectories. It can be observed from the maps shown in Figure 6.5 (top) that D-Arg shows very high probability of visiting a particular binding site for the MFI (1 0 1)

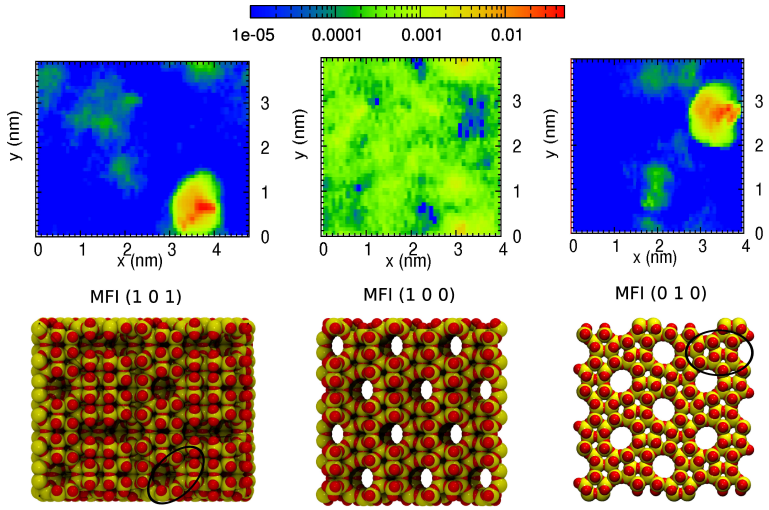

Figure 6.5: Two dimensional maps constructed from standard MD simulations showing the probability density of finding a D-Arginine atoms along the lateral positions on the zeolite surface for $d_{\text{ARGN-COM}}$ < 1 nm. Red color depicts higher probability.

and MFI (0 1 0) surfaces. Furthermore, these maps help identify the preferential binding locations on the surface. As can be seen from the snapshots of the zeolite surfaces in Figure 6.5 (bottom) that the topographic arrangement of surface oxygen atoms for MFI (1 0 1) and MFI (0 1 0) preferential binding sites differs significantly. The topography of surface oxygen sites on the MFI (1 0 1) surface is more approachable for D-Arg α-amino group and guanidinium group in parallel orientation. Also, the results from the standard MD simulations are based upon one highly favorable interaction site. On the other hand, for the MFI (1 0 0) surface, D-Arg interacts with the whole surface almost uniformly, but an indication of preferential binding with the surface is absent. These findings raise concern that standard MD alone is not sufficient for rigorous sampling of all the binding sites on the zeolite surfaces. Furthermore, a quantitative understanding of the thermodynamic parameters defining the binding affinity lacks from these simulations. To address these concerns, well-tempered metadynamics simulations [171] of these systems were performed as discussed previously.

6.4.2 Well-Tempered Metadynamics Simulations

The trajectories from the well-tempered metadynamics simulations were subjected to similar analysis to track the location of the D-Arg molecules COM location along z-axis. Figure 6.6A shows the $d_{\text{ARGN-COM}}$ as the function of simulation time. It can be observed that the molecule samples separations between the surface and $d_{\text{ARGN-COM}} \approx$ 2 nm extensively. This assists sampling along the z-axis as well as the lateral crystal plane (Figure 6.6B (top)). It can be noted that D-Arg molecules explore more than one preferred binding locations for all the three surfaces studied. Furthermore, more than one binding sites with specific topographic arrangement of surface oxygen atoms can be identified for the MFI (1 0 1) surface as shown in Figure 6.6B (bottom).

The enhanced sampling of conformations helps in estimation of free energy profiles [285] as a function of $d_{\text{ARGN-COM}}$. The free energy profiles and orientation of D-Arg on the three zeolite surfaces are shown in Figure 6.7, which provide estimates of free energy difference between the bulk and zeolite surface. For MFI (1 0 1) surface, two free energy minima are observed at $d_{\text{ARGN-COM}} \approx$ 0.27 nm (-33 kJ/mol) and 0.40 nm (-41kJ/mol). Corresponding values of $P_2(\cos\theta)$ at these COM distances are $\approx$ -0.35 and 0.0 respectively. This indicates that the free energy minima closer to the MFI (1 0 1) surface has a preference for parallel orientation of D-Arg molecule, whereas the minima slightly far away from the surface indicates a random orientation based on the average value of $P_2(\cos\theta)$. These observations about the orientation are somewhat consistent with the observations from the standard MD simulations, where parallel orientation was observed at $d_{\text{ARGN-COM}} \approx$ 0.3 nm. For the MFI (0 1 0) surface, a very deep free energy minima (-60 kJ/mol) was observed at $d_{\text{ARGN-COM}} \approx$ 0.4 nm and $P_2(\cos\theta) \approx$ 0.2 at this distance indicated preferred non-parallel orientation. In addition, for MFI the (1 0 0) surface a free

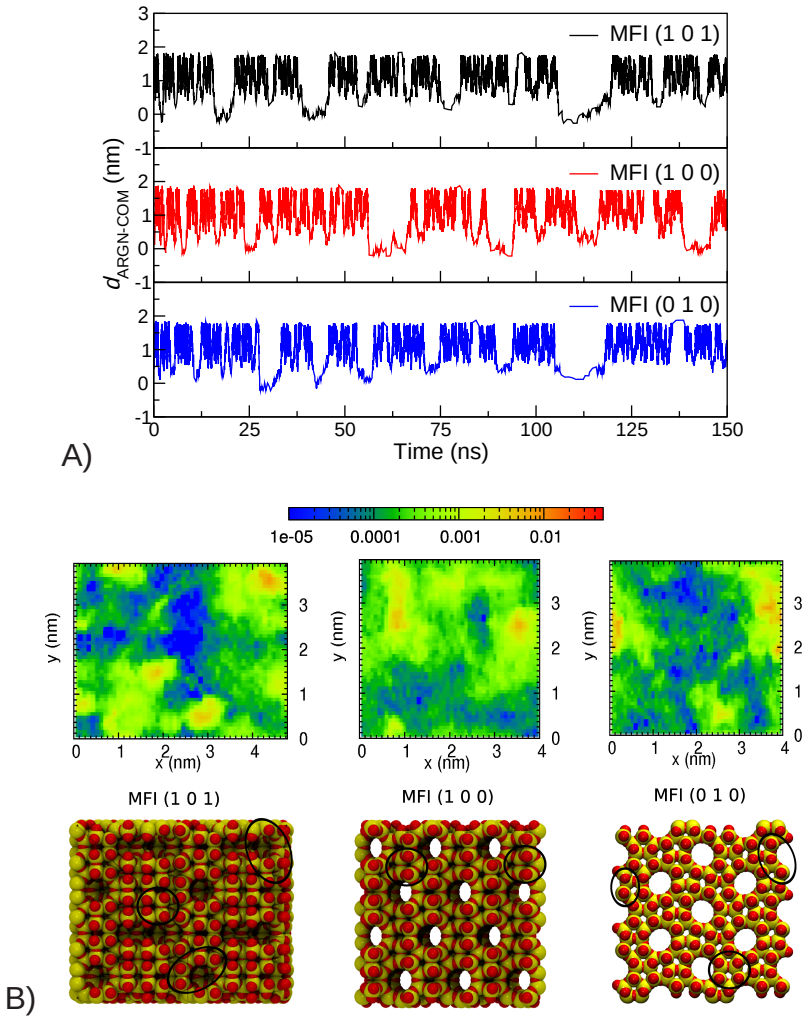

Figure 6.6: A) Position of D-Arginine COM as a function of time during well-tempered metadynamics simulations. B) Two dimensional maps constructed from well-tempered metadynamics simulations showing the probability density of finding a D-Arginine atoms along the lateral positions on the zeolite surface for $d_{ARGN-COM}$ < 1 nm. Red color depicts higher probability.

energy well of -45 kJ/mol was observed at a relatively closer distance of 0.2 nm from the surface with $P_2(\cos\theta) \approx$ -0.15 indicating slight preference for parallel orientation.

Since the average values of $P_2(\cos\theta)$ do not provide information about the distribution of orientations of the molecules, the 2-dimensional probability maps of angle θ (as defined in Figure 6.4A) were constructed. Since θ is defined as

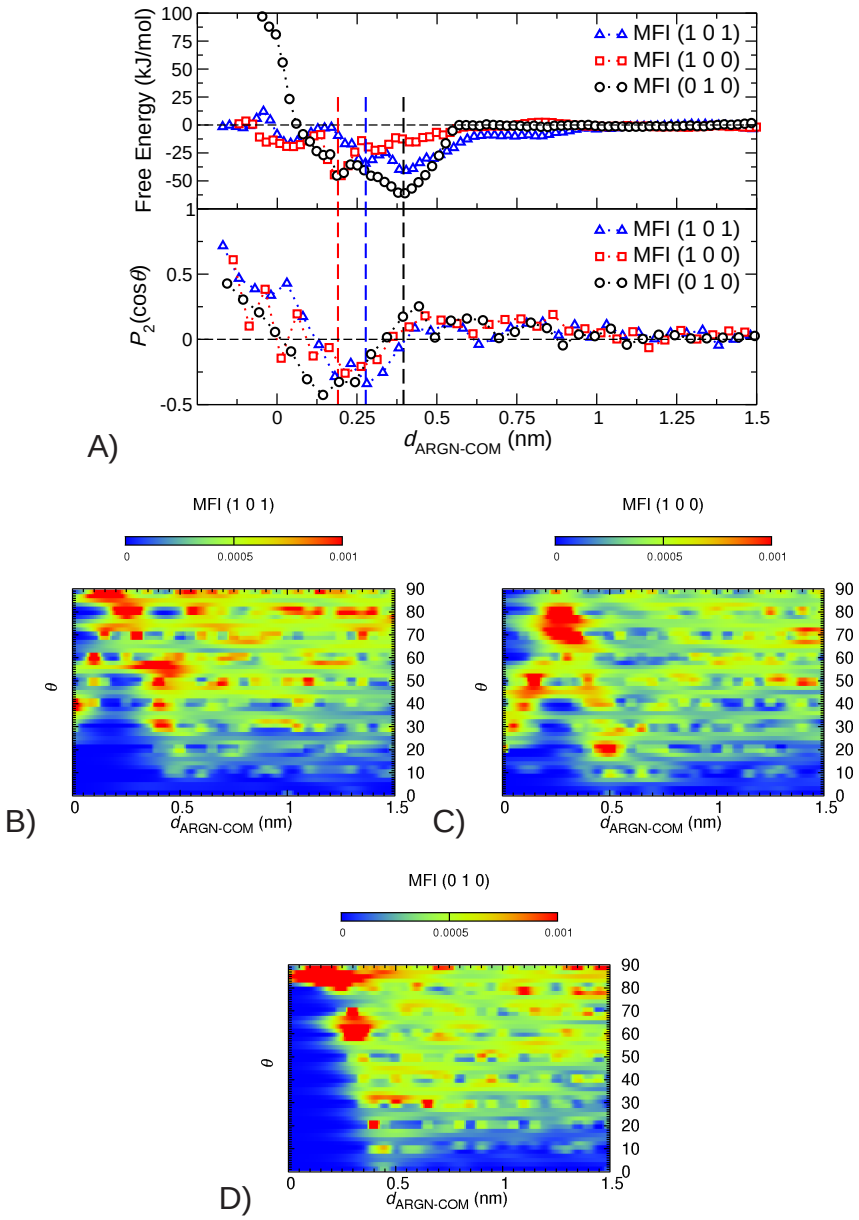

Figure 6.7: A) Free-energy surfaces reconstructed based upon the well-tempered metadynamics simulations (top) and orientation based upon these simulations. 2-dimensional maps showing probability distribution of orientation for B) MFI (1 0 1), C) MFI (1 0 0), and D) MFI (0 1 0) surfaces. Red color depicts higher probability.

the angle formed with x-axis, θ = 90° represents molecules oriented parallel to the zeolite surface. For the MFI (1 0 1) surface (Figure 6.7B), distribution shows strongly favored close to parallel orientation (very small population for θ < 50°) near

$d_{\text{ARGN-COM}} \approx$ 0.27 nm. At the location of second free energy minima $d_{\text{ARGN-COM}} \approx$ 0.4 nm, θ values are concentrated in the range 60° > θ > 30° indicating tendency of non-parallel orientation.

For the MFI (0 1 0) surface (Figure 6.7D) near $d_{\text{ARGN-COM}} \approx$ 0.4 nm, θ values are distributed over a broad range with significantly higher probability at $\theta \approx$ 90° and $\theta \approx$ 20°. This distribution indicates a combination of parallel and normal orientation of inhibitor molecule at the MFI (0 1 0) surface. Finally, Figure 6.7C shows preference for near parallel orientation with diminishing probability of observing normal orientation at $d_{\text{ARGN-COM}} \approx$ 0.2 nm for the MFI (1 0 0) surface.

To summarize above observations, D-Arg binds preferentially at the sites with specific topographic arrangement of surface oxygens at the MFI (1 0 1) surface. The free energy minima close to the MFI (1 0 1) surface is accompanied by preferred parallel orientation of the inhibitor molecule. This enables higher surface coverage per inhibitor molecule and blocks more precursor molecules from interacting with the crystal surface. For the MFI (0 1 0) surface, non-parallel orientation near the free energy minima results in relatively lower surface coverage, which hinders fewer precursor molecules approaching the surface.

Finally, for the MFI (1 0 0) surface, the free energy minima is found to be very close to the surface. Despite a preference to near parallel orientation, part of inhibitor molecule may enter the sinusoidal pores at these separations offering lower surface coverage. It should be noted that binding of inhibitor molecule to the surface causes release of sodium ions from the zeolite surface to bulk water. The release of ions results in entropic gain [287, 288]. The inhibitor molecule in parallel orientation will release more ions, which will lead to entropically favorable configuration.

It is acknowledged that providing a complete picture of growth inhibition

mechanism requires consideration of a finite concentration of inhibitor molecules, which is beyond the scope of current study. However, these results indicate that on a per inhibitor molecule basis, D-Arg provides a higher surface coverage at the MFI (1 0 1) surface and offers higher growth inhibition by blocking more precursor molecules.

6.5 Conclusions

In this chapter, molecular simulations were employed to study the mechanism and thermodynamic factors behind the growth inhibiting action of D-Arg molecules in synthesis of silicalite-1 zeolites. Both standard MD simulations and well-tempered metadynamics [171] were employed to gain insight of the underlying mechanism of growth inhibition. It was observed that MD simulations offer limited sampling. Well-tempered metadynamics method was found to be effective in sampling the D-Arg conformation and provided quantitative insight into thermodynamic origins of growth inhibition.

This chapter highlights that the binding affinity estimated from the free energy minima alone can not predict the growth inhibition offered by the molecules. It was found that the location of the free energy minima and the orientation of inhibitor molecule in this minima play vital role in determining the efficacy as a growth inhibitor. Experiments [1] have shown that D-Arg is the most effective for inhibiting the growth perpendicular to MFI (1 0 1) crystal surface. In this study, it was found that the free energy minima near the MFI (1 0 1) surface favors parallel orientation of the D-Arg molecule and facilitates larger surface coverage, thereby blocking more precursor molecules from attaching to the surface per inhibitor molecule. Furthermore, despite the deeper free energy minima near the MFI (0 1 0) surface, a preference for non-parallel orientation was attributed to the lesser surface coverage

per inhibitor molecule. It is important to acknowledge that these simulation results are limited to quantifying the interactions of a single molecule with the surface. Further investigation to reaffirm the findings of this study is required by considering finite concentration of the molecules. Such an approach will account for the many-body interactions between growth inhibitor molecules, which is beyond the reach of current study considering surface interactions of a single molecule.

Chapter 7 Summary and Future Directions

7.1 Summary

This dissertation focused on computer simulations of interfacial phenomena. Three different applications of interfacial phenomena namely polymer bound layers in the proximity of nanoparticles, polymer thin films at a substrate and zeolite growth modifiers were studied by developing new simulation algorithms [6, 8] or by applying existing techniques.

The study of polymer-nanoparticle systems with specific focus on the interfacial polymer layer was accomplished by employing a novel Monte Carlo simulation methodology. This methodology coupled connectivity-altering algorithms [2, 69] with preferential sampling [183] for the first time. In addition development of a new Monte Carlo move involving shrinking/growing of inner segment coupled with a growing/shrinking of a randomly selected end [6] was implemented enabling mass transfer from the surface to bulk polymer. As a result of these developments, rapid equilibration of polymer conformations in the proximity of silica surfaces was achieved. The simulations were directed at probing the effect of curvature on the conformation of bound layer. It was found to play important role in determination of the bound layer characteristic. These effects become more pronounced as the size of nanoparticle becomes comparable to the polymer Kuhn segment length. The origin was traced to the entropic penalty associated with the formation of longer contacts at highly curved nanoparticle surfaces. As the consequences, the extent of polymer bound layer in the proximity of nanoparticles also exhibited a decrease. Furthermore, the elusive origin of curvature dependence of bound layer

thickness was explained beyond geometric arguments [186–188]. It was acknowledged that even these improved simulation algorithms cannot render the simulations of long polymer chains feasible. To extend this study further, coarse-grained (CG) polymer models were developed. Following a hierarchical approach similar to previous work [225], CG models accounting for local stiffness of a polymer (*cis*-1,4 Polyisoprene) were developed by employing the Iterative Boltzmann Inversion (IBI) method [7]. Furthermore, interaction potentials between *cis*-1,4 Polyisoprene and silica surfaces were derived. Using a method available in literature [227], potentials for particles of arbitrary curvature were calculated with significantly lower computational efforts than the existing methods [83, 84]. For the first time it was demonstrated that the derived CG potentials faithfully reproduce conformation of the polymer bound layers and fluctuations of train segment lengths.

The reaction-diffusion phenomena in the chemically-amplified resists was modeled using stochastic simulations. For the first time, a unified framework was presented that is able to describe deprotection rates at different acid loading with the same set of parameters. The diffusion of acid molecules in the glassy thin films was modeled as anomalous diffusion [240, 269] to achieve sub-diffusive behavior. It was observed that anomalous diffusion alone was not able to capture the experimental results for acid catalyzed deprotection in resists. A new mechanism of acid annihilation was proposed, and it was shown that the proposed mechanism was able to capture the experimental deprotection profiles with the help of only two adjustable parameters for a wide range of acid loadings. On a related topic, the effects of substrate-induced depth dependent diffusion rates were studied. The lattice simulations employed depth dependent diffusivity in conjunction with the deprotection model available in literature [54]. Proof–of–concept simulations demonstrated that interfacial effects e.g. narrowing of features near substrate and broader feature size near the free surface can be modeled by incorporating

depth dependent diffusion rates in simulation model.

Finally, the thermodynamic origin of zeolite growth modifier molecules was probed by molecular simulations. The effect of D-Arginine on silicalite-1 growth were shown to depend upon the binding affinity and preferred orientation at the preferential binding sites. It was demonstrated that D-Arginine provides highest surface coverage per growth inhibitor molecule for the MFI (1 0 1) surface due to parallel orientation at the free energy minima close to zeolite surface. Therefore, on a per molecule basis, D-Arginine blocks more precursor molecules from attaching at the surface. It was acknowledged that a complete understanding of growth inhibition mechanism requires finite concentration of growth inhibitors in solution, which was not considered in the current study.

7.2 Future Directions

7.2.1 Thermodynamic and Structural View of Interacting Bound Layers

Polymer bound layers around particles interact with each other to form a percolating network [3], which is at the origin of enhanced mechanical and barrier properties [13, 14]. Free energy of interaction between two particles in polymer matrix as a function of their separation [11, 85] can define the region where bound layers interact (Figure 7.1). Individual contributions arising from tail, train and loop segments requires properly designed efficient simulations. Such information will further elucidate the extent of interactions between the different segments of bound layers, which play critical role in understanding the behavior of interfacial layers.

Quantification of polymer-particle and particle-particle interactions and its impact on structure is a driving factor in selection of nanoparticle modifications [289]. Chemistry of polymer and particles both affect the effective interactions. The

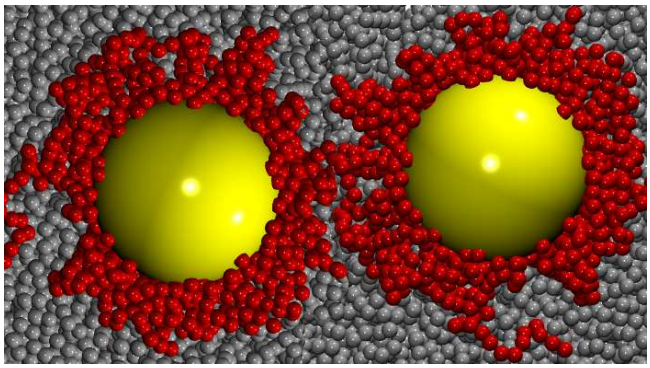

Figure 7.1: Snapshot depicting two nanoparticles with their polymer bound layers interacting with each other.

CG models development methodology applied for *cis*-1,4 Polyisoprene discussed in Chapter 4 will be extended to polymers with diverse chemical architecture and stereo specificity in combination with the surfaces beyond silica such as graphite [30, 31, 86] and carbon black [290]. These studies will provide the properties of polymer bound layer for a diverse set of polymers at the surfaces with varying interaction strengths and chemical details.

CG models used in the simulations studies are able to provide structural properties in good agreement with the atomistic simulations and experiments, but their effectiveness in estimating dynamic and mechanical properties remains a topic of further deliberation [92, 217, 291]. For instance, CG models tend to accelerate or slow down the dynamics of particle motion in polymer matrix [92, 291] whereas mechanical properties predicted by CG models for bulk polymer may differ from experimental values by an order of magnitude [217]. One possible avenue of addressing these issues is reverse-mapping of CG structure to atomistic structure [292]. Sampling of polymer structures can be performed in CG representation, followed by reverse-mapping to atomistic details for estimation of dynamic and mechanical properties of the system. Following this approach will be helpful in estimation of dynamic and mechanical properties of the polymer-nanoparticle systems.

Transferability of CG potentials at different temperatures and degree of polymerization [293, 294] remains another issue to be addressed. Such issues may be paramount in studies below the glass transition temperature of polymer. Recent experiments [295] have shown that the conditions for mechanical reinforcement for glassy nanocomposites are strikingly different from those considered in nanocomposite melts. Future modeling efforts on understanding the structure property relationship in the light of polymer-particle interactions should be directed at investigating such effects in glassy polymer nanocomposites. All of the above challenges present significant future opportunities in the modeling of polymer-nanoparticle interactions and developing clearer understanding of the interfacial phenomena in polymer nanocomposites.

7.2.2 Interfacial Effects in CA Resists

Quantitative estimation of parameters controlling image formation in thin film CA resists is successfully achieved by incorporating anomalous diffusion and acid annihilation mechanism [8]. In Chapter 5, stochastic lattice simulations incorporating position dependent diffusion rates were shown to produce depth dependent feature shapes. In future, methodologies employing anomalous diffusion to produce depth dependent diffusion rates accounting for interfacial effects in ultrathin films [50, 140–145] will be pursued. Such studied will provide better quantitative understanding of reaction-diffusion process in ultra-thin films and help in estimation of line edge roughness (LER). In addition, Vogt et al. [4] demonstrated that the size of photogenerated acid molecule is a critical factor in determination of LER. Studies considering acid molecules of variable size will help in predicting effects of size of acid molecules on LER. Another avenue for gaining further insight is employing coarse-grained simulations as have been performed in previous studies [135]. Such kind of mesoscale simulations can be helpful in estimation of the

diffusion rates in near substrate regions and help further in predicting the deprotected feature shapes.

7.2.3 Control of Zeolite Morphology

Adsorption on a solid interface is a topic of wide interest. In this dissertation, current efforts were focused on validating the hypothesis that preferential adsorption of growth modifiers controls resulting zeolite morphology. The free energy simulations of atomistic models of small molecules on zeolite surface were able to provide quantitative insight about the interactions between a single molecule and model surface. However, complete explanation of the mechanism will require consideration of a finite concentration of growth inhibitor molecules in solution at synthesis conditions (160°C temperature and autogenous pressure).

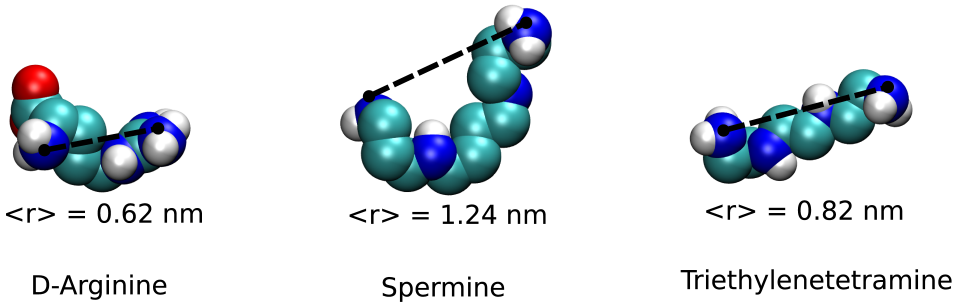

Figure 7.2: Schematics of different zeolite growth modifier molecules with the mean distance of the terminal Nitrogen atoms.

It is observed in experimental studies that changes in the chemical architecture of the inhibitor molecules 7.2 have profound effect on the zeolite morphology. For instance, spermine effectively inhibits growth of the MFI (0 1 0) surface, but triethylenetetramine does not show similar effect despite the similar number of amine groups. Simulations will analyze details such as mechanism of adsorption and conformational arrangement of growth modifiers on the zeolite surfaces, which may not

be directly measurable from experimental techniques. Ultimate aim of the simulations, rational design of growth modifier will be performed by using simulations as a tool to achieve the final aim of optimal design of zeolite structures.

References

[1] A. I. Lupulescu and J. D. Rimer, “Tailoring Silicalite-1 Crystal Morphology with Molecular Modifiers,” *Angew. Chem. Int. Ed.*, vol. 51, no. 14, pp. 3345–3349, 2012.

[2] N. C. Karayiannis, V. G. Mavrantzas, and D. N. Theodorou, “A Novel Monte Carlo Scheme for the Rapid Equilibration of Atomistic Model Polymer Systems of Precisely Defined Molecular Architecture,” *Phys. Rev. Lett.*, vol. 88, p. 105503, Feb 2002.

[3] S. E. Harton, S. K. Kumar, H. Yang, T. Koga, K. Hicks, H. Lee, J. Mijovic, M. Liu, R. S. Vallery, and D. W. Gidley, “Immobilized Polymer Layers on Spherical Nanoparticles,” *Macromolecules*, vol. 43, no. 7, pp. 3415–3421, 2010.

[4] B. D. Vogt, S. Kang, V. M. Prabhu, E. K. Lin, S. K. Satija, K. Turnquest, and W.-l. Wu, “Measurements of the Reaction-Diffusion Front of Model Chemically Amplified Photoresists with Varying Photoacid Size,” *Macromolecules*, vol. 39, no. 24, pp. 8311–8317, 2006.

[5] D. S. Pearson, G. Ver Strate, E. Von Meerwall, and F. C. Schilling, “Viscosity and self-diffusion coefficient of linear polyethylene,” *Macromolecules*, vol. 20, no. 5, pp. 1133–1141, 1987.

[6] Y. N. Pandey and M. Doxastakis, “Detailed atomistic Monte Carlo simulations of a polymer melt on a solid surface and around a nanoparticle,” *J. Chem. Phys.*, vol. 136, no. 9, p. 094901, 2012. [Online]. Available: http://dx.doi.org/10.1063/1.3689316

[7] D. Reith, M. Pütz, and F. Müller-Plathe, “Deriving effective mesoscale potentials from atomistic simulations,” *J. Comput. Chem.*, vol. 24, no. 13, pp. 1624–1636, 2003.

[8] G. M. Perera, Y. N. Pandey, A. A. Patil, G. E. Stein, and M. Doxastakis, “Reaction Kinetics in Acid-Catalyzed Deprotection of Polymer Films,” *J. Phys. Chem. C*, vol. 116, no. 46, pp. 24 706–24 716, 2012. [Online]. Available: http://dx.doi.org/10.1021/jp308997g

[9] B. W. H. van Beest, G. J. Kramer, and R. A. van Santen, “Force fields for silicas and aluminophosphates based on *ab initio* calculations,” *Phys. Rev. Lett.*, vol. 64, pp. 1955–1958, 1990.

[10] I. Saika-Voivod, F. Sciortino, and P. H. Poole, “Computer simulations of liquid silica: Equation of state and liquid–liquid phase transition,” *Phys. Rev. E*, vol. 63, p. 011202, Dec 2000.

[11] J. B. Hooper and K. S. Schweizer, “Contact Aggregation, Bridging, and Steric Stabilization in Dense Polymer-Particle Mixtures,” *Macromolecules*, vol. 38, no. 21, pp. 8858–8869, 2005.

[12] S. Sen, Y. Xie, S. K. Kumar, H. Yang, A. Bansal, D. L. Ho, L. Hall, J. B. Hooper, and K. S. Schweizer, “Chain Conformations and Bound-Layer Correlations in Polymer Nanocomposites,” *Phys. Rev. Lett.*, vol. 98, p. 128302, 2007.

[13] G. J. Papakonstantopoulos, K. Yoshimoto, M. Doxastakis, P. F. Nealey, and J. J. de Pablo, “Local mechanical properties of polymeric nanocomposites,” *Phys. Rev. E*, vol. 72, p. 031801, 2005.

[14] L. Khounlavong and V. Ganesan, “Influence of interfacial layers upon the barrier properties of polymer nanocomposites,” *J. Chem. Phys.*, vol. 130, no. 10, p. 104901, 2009.

[15] R. Krishnamoorti, “Strategies for Dispersing Nanoparticles in Polymers,” *MRS Bull.*, vol. 32, pp. 341–347, 3 2007.

[16] J. Jancar, J. Douglas, F. Starr, S. Kumar, P. Cassagnau, A. Lesser, S. Sternstein, and M. Buehler, “Current issues in research on structure-property relationships in polymer nanocomposites,” *Polymer*, vol. 51, no. 15, pp. 3321–3343, 2010.

[17] V. Ganesan, “Some issues in polymer nanocomposites: Theoretical and modeling opportunities for polymer physics,” *J. Polym. Sci., Part B: Polym. Phys.*, vol. 46, no. 24, pp. 2666–2671, 2008.

[18] V. Ganesan, C. J. Ellison, and V. Pryamitsyn, “Mean-field models of structure and dispersion of polymer-nanoparticle mixtures,” *Soft Matter*, vol. 6, pp. 4010–4025, 2010.

[19] V. Goel, T. Chatterjee, L. Bombalski, K. Yurekli, K. Matyjaszewski, and R. Krishnamoorti, “Viscoelastic properties of silica-grafted poly(styrene-acrylonitrile) nanocomposites,” *J. Polym. Sci., Part B: Polym. Phys.*, vol. 44, pp. 2014–2023, 2006.

[20] M. Surve, V. Pryamitsyn, and V. Ganesan, “Nanoparticles in Solutions of Adsorbing Polymers: Pair Interactions, Percolation, and Phase Behavior,” *Langmuir*, vol. 22, no. 3, pp. 969–981, 2006.

[21] J. B. Hooper and K. S. Schweizer, “Theory of Phase Separation in Polymer Nanocomposites,” *Macromolecules*, vol. 39, no. 15, pp. 5133–5142, 2006.

[22] M. E. Mackay, A. Tuteja, P. M. Duxbury, C. J. Hawker, B. Van Horn, Z. Guan, G. Chen, and R. S. Krishnan, “General Strategies for Nanoparticle Dispersion,” *Science*, vol. 311, no. 5768, pp. 1740–1743, 2006.

[23] M. Stamm and J.-U. Sommer, “Polymer-nanoparticle films - Entropy and enthalpy at play,” *Nat. Mater.*, vol. 6, no. 4, pp. 260–261, 2007.

[24] S. K. Kumar and R. Krishnamoorti, “Nanocomposites: Structure, Phase Behavior, and Properties,” *Annu. Rev. Chem. Biomol. Eng.*, vol. 1, no. 1, pp. 37–58, 2010.

[25] P. G. de Gennes, “Conformations of Polymers Attached to an Interface,” *Macromolecules*, vol. 13, no. 5, pp. 1069–1075, 1980.

[26] J. M. H. M. Scheutjens and G. J. Fleer, “Statistical theory of the adsorption of interacting chain molecules. 1. Partition function, segment density distribution, and adsorption isotherms,” *J. Phys. Chem.*, vol. 83, no. 12, pp. 1619–1635, 1979.

[27] J. M. H. M. Scheutjens and G. J. Fleer, “Statistical theory of the adsorption of interacting chain molecules. 2. Train, loop, and tail size distribution,” *J. Phys. Chem.*, vol. 84, no. 2, pp. 178–190, 1980.

[28] M. Aubouy and E. Raphaël, “Scaling Description of a Colloidal Particle Clothed with Polymers,” *Macromolecules*, vol. 31, no. 13, pp. 4357–4363, 1998.

[29] K. T. Marla and J. C. Meredith, “Nanoscale Colloids in a Freely Adsorbing Polymer Solution: A Monte Carlo Simulation Study,” *Langmuir*, vol. 20, no. 4, pp. 1501–1510, 2004.

[30] K. C. Daoulas, V. A. Harmandaris, and V. G. Mavrantzas, “Detailed Atomistic Simulation of a Polymer Melt/Solid Interface: Structure, Density, and Conformation of a Thin Film of Polyethylene Melt Adsorbed on Graphite,” *Macromolecules*, vol. 38, no. 13, pp. 5780–5795, 2005.

[31] K. F. Mansfield and D. N. Theodorou, “Atomistic simulation of a glassy polymer/graphite interface,” *Macromolecules*, vol. 24, no. 15, pp. 4295–4309, 1991.

[32] M. Doxastakis, Y.-L. Chen, O. Guzmán, and J. J. de Pablo, “Polymer-particle mixtures: Depletion and packing effects,” *J. Chem. Phys.*, vol. 120, no. 19, pp. 9335–9342, 2004.

[33] D. Brown, V. Marcadon, P. Mele, and N. D. Alberola, “Effect of Filler Particle Size on the Properties of Model Nanocomposites,” *Macromolecules*, vol. 41, no. 4, pp. 1499–1511, 2008.

[34] A. Nakatani, W. Chen, R. Schmidt, G. Gordon, and C. Han, “Chain dimensions in polysilicate-filled poly(dimethyl siloxane),” *Polymer*, vol. 42, no. 8, pp. 3713–3722, 2001.

[35] F. W. Starr, T. B. Schrøder, and S. C. Glotzer, “Molecular Dynamics Simulation of a Polymer Melt with a Nanoscopic Particle,” *Macromolecules*, vol. 35, no. 11, pp. 4481–4492, 2002.

[36] T. V. M. Ndoro, E. Voyiatzis, A. Ghanbari, D. N. Theodorou, M. C. Böhm, and F. Müller-Plathe, “Interface of Grafted and Ungrafted Silica Nanoparticles with a Polystyrene Matrix: Atomistic Molecular Dynamics Simulations,” *Macromolecules*, vol. 44, no. 7, pp. 2316–2327, 2011.

[37] L. M. Hall, A. Jayaraman, and K. S. Schweizer, “Molecular theories of polymer nanocomposites,” *Curr. Opin. Solid State Mater. Sci.*, vol. 14, no. 2, pp. 38–48, 2010.

[38] A. Jayaraman and K. S. Schweizer, “Effective Interactions, Structure, and Phase Behavior of Lightly Tethered Nanoparticles in Polymer Melts,” *Macromolecules*, vol. 41, no. 23, pp. 9430–9438, 2008.

[39] A. Jayaraman and K. S. Schweizer, “Effective Interactions and Self-Assembly of Hybrid Polymer Grafted Nanoparticles in a Homopolymer Matrix,” *Macromolecules*, vol. 42, no. 21, pp. 8423–8434, 2009.

[40] N. Nair and A. Jayaraman, “Self-Consistent PRISM Theory-Monte Carlo Simulation Studies of Copolymer Grafted Nanoparticles in a Homopolymer Matrix,” *Macromolecules*, vol. 43, no. 19, pp. 8251–8263, 2010.

[41] N. Nair, N. Wentzel, and A. Jayaraman, “Effect of bidispersity in grafted chain length on grafted chain conformations and potential of mean force between polymer grafted nanoparticles in a homopolymer matrix,” *J. Chem. Phys.*, vol. 134, no. 19, p. 194906, 2011.

[42] J. Berriot, H. Montes, F. Lequeux, D. Long, and P. Sotta, “Evidence for the Shift of the Glass Transition near the Particles in Silica-Filled Elastomers,” *Macromolecules*, vol. 35, no. 26, pp. 9756–9762, 2002.

[43] G. Allegra, G. Raos, and M. Vacatello, “Theories and simulations of polymer-based nanocomposites: From chain statistics to reinforcement,” *Prog. Polym. Sci.*, vol. 33, no. 7, pp. 683 – 731, 2008.

[44] Q. Zeng, A. Yu, and G. Lu, “Multiscale modeling and simulation of polymer nanocomposites,” *Prog. Polym. Sci.*, vol. 33, no. 2, pp. 191–269, 2008.

[45] D. M. Trombly and V. Ganesan, “Curvature effects upon interactions of polymer-grafted nanoparticles in chemically identical polymer matrices,” *J. Chem. Phys.*, vol. 133, no. 15, p. 154904, 2010.

[46] J. Kalb, D. Dukes, S. K. Kumar, R. S. Hoy, and G. S. Grest, “End grafted polymer nanoparticles in a polymeric matrix: Effect of coverage and curvature,” *Soft Matter*, vol. 7, pp. 1418–1425, 2011.

[47] D. Hone, H. Ji, and P. A. Pincus, “Polymer adsorption on rough surfaces. 1. Ideal long chain,” *Macromolecules*, vol. 20, no. 10, pp. 2543–2549, 1987.

[48] R. R. Madathingal and S. L. Wunder, “Confinement Effects of Silica Nanoparticles with Radii Smaller and Larger than Rg of Adsorbed Poly(ethylene oxide),” *Macromolecules*, vol. 44, no. 8, pp. 2873–2882, 2011.

[49] G. Arya, “Chain Stiffness and Attachment-Dependent Attraction between Polyelectrolyte-Grafted Colloids,” *J. Phys. Chem. B*, vol. 114, no. 48, pp. 15 886–15 896, 2010.

[50] D. S. Fryer, P. F. Nealey, and J. J. de Pablo, “Scaling of T-g and reaction rate with film thickness in photoresist: A thermal probe study,” *J. Vac. Sci. Technol., B*, vol. 18, no. 6, pp. 3376–3380, 2000.

[51] V. M. Prabhu, S. Sambasivan, D. Fischer, L. K. Sundberg, and R. D. Allen, “Quantitative depth profiling of photoacid generators in photoresist materials by near-edge X-ray absorption fine structure spectroscopy,” *Appl. Surf. Sci.*, vol. 253, no. 2, pp. 1010–1014, 2006.

[52] J. T. Woodward, J. Hwang, V. M. Prabhu, and K.-W. Choi, “Hunting the Origins of Line Width Roughness with Chemical Force Microscopy,” *AIP Conf. Proc.*, vol. 931, no. 1, pp. 413–418, 2007.

[53] R. L. Jones, T. Hu, E. K. Lin, W.-L. Wu, D. L. Goldfarb, M. Angelopoulos, B. C. Trinque, G. M. Schmid, M. D. Stewart, and C. G. Willson, “Formation of deprotected fuzzy blobs in chemically amplified resists,” *J. Polym. Sci., Part B: Polym. Phys.*, vol. 42, no. 17, pp. 3063–3069, 2004.

[54] S. Kang, W.-l. Wu, K.-W. Choi, A. De Silva, C. K. Ober, and V. M. Prabhu, “Characterization of the Photoacid Diffusion Length and Reaction Kinetics in EUV Photoresists with IR Spectroscopy,” *Macromolecules*, vol. 43, no. 9, pp. 4275–4286, 2010.

[55] V. M. Prabhu, S. Kang, D. L. VanderHart, S. K. Satija, E. K. Lin, and W.-l. Wu, “Photoresist Latent and Developer Images as Probed by Neutron Reflectivity Methods,” *Adv. Mater.*, vol. 23, no. 3, pp. 388–408, 2011.

[56] T. Kozawa, S. Tagawa, J. J. Santillan, and T. Itani, “Impact of Nonconstant Diffusion Coefficient on Latent Image Quality in 22 nm Fabrication using Extreme Ultraviolet Lithography,” *J. Photopolym. Sci. Technol.*, vol. 21, no. 3, pp. 421–427, 2008.

[57] F. A. Houle, W. D. Hinsberg, M. Morrison, M. I. Sanchez, G. Wallraff, C. Larson, and J. Hoffnagle, “Determination of coupled acid catalysis-diffusion processes in a positive-tone chemically amplified photoresist,” *J. Vac. Sci. Technol. B*, vol. 18, no. 4, pp. 1874–1885, 2000.

[58] R. A. Lawson and C. L. Henderson, “Mesoscale simulation of molecular resists: The effect of PAG distribution homogeneity on LER,” *Microelectron. Eng.*, vol. 86, no. 4-6, pp. 741–744, 2009.

[59] R. A. Lawson and C. L. Henderson, “Mesoscale kinetic Monte Carlo simulations of molecular resists: effects of photoacid homogeneity on resolution,

line-edge roughness, and sensitivity," *J. Micro. Nanolithogr. MEMS MOEMS*, vol. 9, no. 1, pp. 013 016–013 016–8, 2010.

[60] E. K. Lin, R. Kolb, S. K. Satija, and W. L. Wu, "Reduced polymer mobility near the polymer solid interface as measured by neutron reflectivity," *Macromolecules*, vol. 32, no. 11, pp. 3753–3757, 1999.

[61] Z. Yang, Y. Fujii, F. K. Lee, C.-H. Lam, and O. K. C. Tsui, "Glass Transition Dynamics and Surface Layer Mobility in Unentangled Polystyrene Films," *Science*, vol. 328, no. 5986, pp. 1676–1679, 2010.

[62] P. S. Metkar, V. Balakotaiah, and M. P. Harold, "Experimental study of mass transfer limitations in Fe- and Cu-zeolite-based NH3-SCR monolithic catalysts," *Chem. Eng. Sci.*, vol. 66, no. 21, pp. 5192–5203, 2011.

[63] E. M. Flanigen, J. M. Bennett, R. W. Grose, J. P. Cohen, R. L. Patton, R. M. Kirchner, and J. V. Smith, "Silicalite, A New Hydrophobic Crystalline Silica Molecular-Sieve," *Nature*, vol. 271, no. 5645, pp. 512–516, 1978.

[64] M. Rubinstein and R. H. Colby, Polymer Physics, p. 53. Oxford: Oxford University Press, 2003.

[65] V. G. Mavrantzas, T. D. Boone, E. Zervopoulou, and D. N. Theodorou, "End-Bridging Monte Carlo: A Fast Algorithm for Atomistic Simulation of Condensed Phases of Long Polymer Chains," *Macromolecules*, vol. 32, no. 15, pp. 5072–5096, 1999.

[66] Z. Chen and F. A. Escobedo, "A configurational-bias approach for the simulation of inner sections of linear and cyclic molecules," *J. Chem. Phys.*, vol. 113, no. 24, pp. 11 382–11 392, 2000.

[67] M. Doxastakis, V. G. Mavrantzas, and D. N. Theodorou, “Atomistic Monte Carlo simulation of cis-1,4 polyisoprene melts. I. Single temperature end-bridging Monte Carlo simulations,” *J. Chem. Phys.*, vol. 115, no. 24, pp. 11 339–11 351, 2001.

[68] P. Gestoso, E. Nicol, M. Doxastakis, and D. N. Theodorou, “Atomistic Monte Carlo Simulation of Polybutadiene Isomers: cis-1,4-Polybutadiene and 1,2-Polybutadiene,” *Macromolecules*, vol. 36, no. 18, pp. 6925–6938, 2003.

[69] B. J. Banaszak and J. J. de Pablo, “A new double-rebridging technique for linear polyethylene,” *J. Chem. Phys.*, vol. 119, no. 4, pp. 2456–2462, 2003.

[70] J. Baschnagel, H. Meyer, F. Varnik, S. Metzger, M. Aichele, M. Müller, and K. Binder, “Computer Simulations of Polymers Close to Solid Interfaces: Some Selected Topics,” *Interface Sci.*, vol. 11, no. 2, pp. 159–173, 2003.

[71] D. Reith, H. Meyer, and F. Müller-Plathe, “Mapping Atomistic to Coarse-Grained Polymer Models Using Automatic Simplex Optimization To Fit Structural Properties,” *Macromolecules*, vol. 34, no. 7, pp. 2335–2345, 2001.

[72] V. A. Harmandaris, N. P. Adhikari, N. F. A. van der Vegt, and K. Kremer, “Hierarchical Modeling of Polystyrene: From Atomistic to Coarse-Grained Simulations,” *Macromolecules*, vol. 39, no. 19, pp. 6708–6719, 2006.

[73] G. Milano and F. Müller-Plathe, “Mapping Atomistic Simulations to Mesoscopic Models: A Systematic Coarse-Graining Procedure for Vinyl Polymer Chains,” *J. Phys. Chem. B*, vol. 109, no. 39, pp. 18 609–18 619, 2005.

[74] H. Fukunaga, J. ichi Takimoto, and M. Doi, “A coarse-graining procedure for flexible polymer chains with bonded and nonbonded interactions,” *J. Chem. Phys.*, vol. 116, no. 18, pp. 8183–8190, 2002.

[75] W. Tschöp, K. Kremer, J. Batoulis, T. Bürger, and O. Hahn, “Simulation of polymer melts. I. Coarse-graining procedure for polycarbonates,” *Acta Polym.*, vol. 49, no. 2-3, pp. 61–74, 1998.

[76] K. Johnston, R. M. Nieminen, and K. Kremer, “A hierarchical dualscale study of bisphenol-A-polycarbonate on a silicon surface: structure, dynamics and impurity diffusion,” *Soft Matter*, vol. 7, pp. 6457–6466, 2011.

[77] A. L. Frischknecht and A. Yethiraj, “Two- and three-body interactions among nanoparticles in a polymer melt,” *J. Chem. Phys.*, vol. 134, no. 17, p. 174901, 2011.

[78] L. Khounlavong, V. Pryamitsyn, and V. Ganesan, “Many-body interactions and coarse-grained simulations of structure of nanoparticle-polymer melt mixtures,” *J. Chem. Phys.*, vol. 133, no. 14, p. 144904, 2010.

[79] M. Doxastakis, Y.-L. Chen, and J. J. de Pablo, “Potential of mean force between two nanometer-scale particles in a polymer solution,” *J. Chem. Phys.*, vol. 123, no. 3, p. 034901, 2005.

[80] M. Rechtsman, F. Stillinger, and S. Torquato, “Designed interaction potentials via inverse methods for self-assembly,” *Phys. Rev. E*, vol. 73, p. 011406, 2006.

[81] A. Ramírez-Hernández, F. A. Detcheverry, and J. J. de Pablo, “Numerical simulation of Gaussian chains near hard surfaces,” *J. Chem. Phys.*, vol. 133, no. 6, p. 064905, 2010.

[82] M. Müller, B. Steinmuller, K. C. Daoulas, A. Ramirez-Hernandez, and J. J. de Pablo, “Polymer-solid contacts described by soft, coarse-grained models,” *Phys. Chem. Chem. Phys.*, vol. 13, pp. 10 491–10 502, 2011.

[83] G. G. Vogiatzis, E. Voyiatzis, and D. N. Theodorou, “Monte Carlo simulations of a coarse grained model for an athermal all-polystyrene nanocomposite system,” *Eur. Polym. J.*, vol. 47, no. 4, pp. 699–712, 2011.

[84] A. Ghanbari, T. V. M. Ndoro, F. Leroy, M. Rahimi, M. C. Böhm, and F. Müller-Plathe, “Interphase Structure in Silica-Polystyrene Nanocomposites: A Coarse-Grained Molecular Dynamics Study,” *Macromolecules*, vol. 45, no. 1, pp. 572–584, 2012.

[85] J. M. D. Lane, A. E. Ismail, M. Chandross, C. D. Lorenz, and G. S. Grest, “Forces between functionalized silica nanoparticles in solution,” *Phys. Rev. E*, vol. 79, p. 050501, 2009.

[86] K. F. Mansfield and D. N. Theodorou, “Molecular dynamics simulation of a glassy polymer surface,” *Macromolecules*, vol. 24, no. 23, pp. 6283–6294, 1991.

[87] D. Barbier, D. Brown, A.-C. Grillet, and S. Neyertz, “Interface between End-Functionalized PEO Oligomers and a Silica Nanoparticle Studied by Molecular Dynamics Simulations,” *Macromolecules*, vol. 37, no. 12, pp. 4695–4710, 2004.

[88] T. V. M. Ndoro, M. C. Böhm, and F. Müller-Plathe, “Interface and Interphase Dynamics of Polystyrene Chains near Grafted and Ungrafted Silica Nanoparticles,” *Macromolecules*, vol. 45, no. 1, pp. 171–179, 2012.

[89] G. J. Fleer, M. A. Cohen Stuart, J. M. H. M. Scheutjens, T. Cosgrove, and B. Vincent, Polymers at Interfaces, pp. 233–270. London: Chapman & Hall, 1993.

[90] G. J. Papakonstantopoulos, M. Doxastakis, P. F. Nealey, J.-L. Barrat, and J. J. de Pablo, “Calculation of local mechanical properties of filled polymers,” *Phys. Rev. E*, vol. 75, p. 031803, 2007.

[91] T. Desai, P. Keblinski, and S. K. Kumar, “Molecular dynamics simulations of polymer transport in nanocomposites,” *J. Chem. Phys.*, vol. 122, no. 13, p. 134910, 2005.

[92] B. Hong, A. Chremos, and A. Z. Panagiotopoulos, “Dynamics in coarse-grained models for oligomer-grafted silica nanoparticles,” *J. Chem. Phys.*, vol. 136, no. 20, p. 204904, 2012.

[93] P. M. Dodd and A. Jayaraman, “Monte carlo simulations of polydisperse polymers grafted on spherical surfaces,” *J. Polym. Sci., Part B: Polym. Phys.*, vol. 50, no. 10, pp. 694–705, 2012.

[94] R. Everaers, S. K. Sukumaran, G. S. Grest, C. Svaneborg, A. Sivasubramanian, and K. Kremer, “Rheology and Microscopic Topology of Entangled Polymeric Liquids,” *Science*, vol. 303, no. 5659, pp. 823–826, 2004.

[95] M. Vacatello, “Monte Carlo Simulations of Polymer Melts Filled with Solid Nanoparticles,” *Macromolecules*, vol. 34, no. 6, pp. 1946–1952, 2001.

[96] M. Vacatello, “Molecular Arrangements in Polymer-Based Nanocomposites,” *Macromol. Theory Simul.*, vol. 11, no. 7, pp. 757–765, 2002.

[97] M. Vacatello, “Predicting the Molecular Arrangements in Polymer-Based Nanocomposites,” *Macromol. Theory Simul.*, vol. 12, no. 1, pp. 86–91, 2003.

[98] D. Bedrov, G. D. Smith, and J. S. Smith, “Matrix-induced nanoparticle interactions in a polymer melt: A molecular dynamics simulation study,” *J. Chem. Phys.*, vol. 119, no. 19, pp. 10 438–10 447, 2003.

[99] G. Srinivas, D. E. Discher, and M. L. Klein, “Self-assembly and properties of diblock copolymers by coarse-grain molecular dynamics.” *Nat. Mater.*, vol. 3, no. 9, pp. 638–644, 2004.

[100] F. W. Starr, J. F. Douglas, and S. C. Glotzer, “Origin of particle clustering in a simulated polymer nanocomposite and its impact on rheology,” *J. Chem. Phys.*, vol. 119, no. 3, pp. 1777–1788, 2003.

[101] R. M. Cordeiro, F. Zschunke, and F. Müller-Plathe, “Mesoscale Molecular Dynamics Simulations of the Force between Surfaces with Grafted Poly(ethylene oxide) Chains Derived from Atomistic Simulations,” *Macromolecules*, vol. 43, no. 3, pp. 1583–1591, 2010.

[102] R. A. Riggleman, G. Toepperwein, G. J. Papakonstantopoulos, J.-L. Barrat, and J. J. de Pablo, “Entanglement network in nanoparticle reinforced polymers,” *J. Chem. Phys.*, vol. 130, no. 24, p. 244903, 2009.

[103] P. Akcora, H. Liu, S. K. Kumar, J. Moll, L. Yu, B. C. Benicewicz, L. S. Schadler, D. Acehan, A. Z. Panagiotopoulos, V. Pryamitsyn, V. Ganesan, J. Ilavsky, P. Thiyagarajan, R. H. Colby, and J. F. Douglas, “Anisotropic self-assembly of spherical polymer-grafted nanoparticles.” *Nat. Mater.*, vol. 8, no. 4, pp. 354–359, 2009.

[104] P. Akcora, S. K. Kumar, J. Moll, S. Lewis, L. S. Schadler, Y. Li, B. C. Benicewicz, A. Sandy, S. Narayanan, J. Ilavsky, P. Thiyagarajan, R. H. Colby, and J. F. Douglas, ““Gel-like” Mechanical Reinforcement in Polymer Nanocomposite Melts,” *Macromolecules*, vol. 43, no. 2, pp. 1003–1010, 2010.

[105] T. B. Martin, A. Seifpour, and A. Jayaraman, “Assembly of copolymer functionalized nanoparticles: a Monte Carlo simulation study,” *Soft Matter*, vol. 7, pp. 5952–5964, 2011.

[106] D. Meng, S. K. Kumar, J. M. D. Lane, and G. S. Grest, “Effective interactions between grafted nanoparticles in a polymer matrix,” *Soft Matter*, vol. 8, pp. 5002–5010, 2012.

[107] J. J. de Pablo, “Coarse-Grained Simulations of Macromolecules: From DNA to Nanocomposites,” *Annu. Rev. Phys. Chem.*, vol. 62, no. 1, pp. 555–574, 2011.

[108] C. Tzoumanekas and D. N. Theodorou, “Topological Analysis of Linear Polymer Melts: A Statistical Approach,” *Macromolecules*, vol. 39, no. 13, pp. 4592–4604, 2006.

[109] C. A. Mack, “Thirty years of lithography simulation,” *Proc. SPIE*, vol. 5754, pp. 1–12, 2005.

[110] F. Dill, W. Hornberger, P. S. Hauge, and J. M. Shaw, “Characterization of positive photoresist,” *IEEE T. Electron Dev.*, vol. 22, no. 7, pp. 445–452, Jul.

[111] A. Neureuther, “If it moves, simulate it!” in Optical Microlithography XXI, Parts 1-3, ser. Proceedings of the Society of Photo-Optical Instrumentation Engineers (SPIE), vol. 6924, no. Part 1-3, p. 92402, 2008.

[112] H. Ito, “Chemical amplification resists: Inception, implementation in device manufacture, and new developments,” *J. Polym. Sci. Pol. Chem.*, vol. 41, no. 24, pp. 3863–3870, 2003.

[113] S. V. Postnikov, M. D. Stewart, H. V. Tran, M. A. Nierode, D. R. Medeiros, T. Cao, J. Byers, S. E. Webber, and C. G. Wilson, “Study of resolution limits due to intrinsic bias in chemically amplified photoresists,” *J. Vac. Sci. Technol. B*, vol. 17, no. 6, pp. 3335–3338, 1999.

[114] E. K. Lin, C. L. Soles, D. L. Goldfarb, B. C. Trinque, S. D. Burns, R. L. Jones, J. L. Lenhart, M. Angelopoulos, C. G. Willson, S. K. Satija, and W. L. Wu, “Direct measurement of the reaction front in chemically amplified photoresists,” *Science*, vol. 297, no. 5580, pp. 372–375, 2002.

[115] M. Zuniga, G. Wallraff, E. Tomacruz, B. Smith, C. Larson, W. D. Hinsburg, and A. R. Neureuther, “Simulation of locally enhanced three-dimensional diffusion in chemically amplified resists,” *J. Vac. Sci. Technol. B*, vol. 11, no. 6, pp. 2862–2866, 1993.

[116] G. Wallraff, J. Hutchinson, W. Hinsberg, F. Houle, P. Seidel, R. Johnson, and W. Oldham, “Thermal and acid-catalyzed deprotection kinetics in candidate deep ultraviolet resist materials,” *J. Vac. Sci. Technol. B*, vol. 12, no. 6, pp. 3857–3862, 1994.

[117] M. Zuniga and A. R. Neureuther, “Reaction-diffusion modeling and simulations in positive deep ultraviolet resists,” *J. Vac. Sci. Technol. B*, vol. 13, no. 6, pp. 2957–2962, 1995.

[118] C. A. Mack, “Lithographic Effects of Acid Diffusion in Chemically Amplified Resists,” in Microelectronics Technology, ser. ACS Symposium Series, vol. 614, ch. 5, pp. 56–68. American Chemical Society, 1995.

[119] E. Croffie, M. Cheng, and A. Neureuther, “Moving boundary transport model for acid diffusion in chemically amplified resists,” *J. Vac. Sci. Technol. B*, vol. 17, no. 6, pp. 3339–3344, 1999.

[120] E. Croffie, L. Yuan, M. S. Cheng, A. Neureuther, F. Houlihan, R. Cirelli, P. Watson, O. Nalamasu, and A. Gabor, “Modeling influence of structural changes in photoacid generators an 193 nm single layer resist imaging,” *J. Vac. Sci. Technol. B*, vol. 18, no. 6, pp. 3340–3344, 2000.

[121] W. Hinsberg, F. Houle, M. Sanchez, and G. Wallraff, “Chemical and physical aspects of the post-exposure baking process used for positive-tone chemically amplified resists,” *IBM J. Res. Dev.*, vol. 45, no. 5, pp. 667–682, 2001.

[122] D. L. Goldfarb, M. Angelopoulos, E. K. Lin, R. L. Jones, C. L. Soles, J. L. Lenhart, and W. li Wu, “Confinement effects on the spatial extent of the reaction front in ultrathin chemically amplified photoresists,” *J. Vac. Sci. Technol. B*, vol. 19, no. 6, pp. 2699–2704, 2001.

[123] F. A. Houle, W. D. Hinsberg, M. I. Sanchez, and J. A. Hoffnagle, “Influence of resist components on image blur in a patterned positive-tone chemically amplified photoresist,” *J. Vac. Sci. Technol. B*, vol. 20, no. 3, pp. 924–931, 2002.

[124] M. D. Stewart, H. V. Tran, G. M. Schmid, T. B. Stachowiak, D. J. Becker, and C. G. Willson, “Acid catalyst mobility in resist resins,” *J. Vac. Sci. Technol. B*, vol. 20, no. 6, pp. 2946–2952, 2002.

[125] M. Yoshizawa and S. Moriya, “Study of the acid-diffusion effect on line edge roughness using the edge roughness evaluation method,” *J. Vac. Sci. Technol. B*, vol. 20, no. 4, pp. 1342–1347, 2002.

[126] C. M. Leewis, A. M. de Jong, L. J. van IJzendoorn, and D. J. Broer, “Simulations with a dynamic reaction-diffusion model of the polymer grating preparation by patterned ultraviolet illumination,” *J. Appl. Phys.*, vol. 95, no. 12, pp. 8352–8356, 2004.

[127] B. Tollkuhn, A. Erdmann, A. Semmler, and C. Nolscher, “Simplified resist models for efficient simulation of contact holes and line ends,” *Microelectron. Eng.*, vol. 78-79, pp. 509–514, 2005.

[128] B. Tollkuhn, M. Uhle, J. Fuhrmann, K. Gartner, A. Heubner, and A. Erdmann, “Benchmark of a lithography simulation tool for next generation applications,” *Microelectron. Eng.*, vol. 83, no. 4-9, pp. 1142–1147, 2006.

[129] S. K. Kim, J. E. Lee, S. W. Park, and H. K. Oh, “Optical lithography simulation for the whole resist process,” *Curr. Appl. Phys.*, vol. 6, no. 1, pp. 48–53, 2006.

[130] T. Kozawa and S. Tagawa, “Resolution blur of latent acid image and acid generation efficiency of chemically amplified resists for electron beam lithography,” *J. Appl. Phys.*, vol. 99, no. 5, 2006.

[131] C. T. Lee, R. A. Lawson, and C. L. Henderson, “Understanding the effects of photoacid distribution homogeneity and diffusivity on critical dimension control and line edge roughness in chemically amplified resists,” *J. Vac. Sci. Technol. B*, vol. 26, no. 6, pp. 2276–2280, 2008.

[132] C. A. Mack, “Stochastic modeling in lithography: autocorrelation behavior of catalytic reaction-diffusion systems,” *J. Micro-Nanolithogr. MEMS MOEMS*, vol. 8, no. 2, p. 029701, 2009.

[133] Y. Fan, M. G. Jeong, J. Ser, S. W. Lee, C. Suh, K. I. Koo, S. Lee, I. Su, L. Zavyalova, B. Falch, J. Huang, and T. Schmoeller, “A Simplified Reaction-diffusion System of Chemically-Amplified Resist Process Modeling for OPC,” in Optical Microlithography XXIII, ser. Proceedings of SPIE-The International Society for Optical Engineering, vol. 7640, p. 764039, 2010.

[134] R. A. Lawson and C. L. Henderson, “Three-dimensional mesoscale model for the simulation of LER in photoresists,” *Proc. SPIE*, pp. 76 392G–76 392G–10, 2010.

[135] H. Morita and M. Doi, “Mesoscale simulation of line-edge structures based on polymer chains in development and rinse processes,” *J. Micro. Nanolithogr. MEMS MOEMS*, vol. 9, no. 4, pp. 041 213–041 213–7, 2010.

[136] T. Kozawa, H. Yamamoto, and S. Tagawa, “Effect of Inhomogeneous Acid Distribution on Line Edge Roughness-Relationship to Line Edge Roughness Originating from Chemical Gradient,” *J. Photopolym Sci. Technol.*, vol. 23, no. 5, pp. 625–630, 2010.

[137] J. Sha, J.-K. Lee, S. Kang, V. M. Prabhu, C. L. Soles, P. V. Bonnesen, and C. K. Ober, “Architectural Effects on Acid Reaction-Diffusion Kinetics in Molecular Glass Photoresists,” *Chem. Mater.*, vol. 22, no. 10, pp. 3093–3098, 2010.

[138] V. M. Prabhu, S. Kang, J. Sha, P. V. Bonnesen, S. Satija, W. L. Wu, and C. K. Ober, “Neutron Reflectivity Characterization of the Photoacid Reaction-Diffusion Latent and Developed Images of Molecular Resists for Extreme Ultraviolet Lithography,” *Langmuir*, vol. 28, no. 20, pp. 7665–7678, 2012.

[139] A. Chatterjee and D. Vlachos, “An overview of spatial microscopic and accelerated kinetic Monte Carlo methods,” *J. Comput. Aided Mater. Des.*, vol. 14, pp. 253–308, 2007.

[140] B. Frank, A. P. Gast, T. P. Russell, H. R. Brown, and C. J. Hawker, “Polymer mobility in thin films,” *Macromolecules*, vol. 29, no. 20, pp. 6531–6534, 1996.

[141] D. B. Hall, D. D. Deppe, K. E. Hamilton, A. Dhinojwala, and J. M. Torkelson, “Probe translational and rotational diffusion in polymers near Tg: roles of

probe size, shape, and secondary bonding in deviations from Debye-Stokes-Einstein scaling," *J. Non-Cryst. Solids*, vol. 235-237, no. 0, pp. 48–56, 1998.

[142] Z. Li, M. Tolan, T. Hohr, D. Kharas, S. Qu, J. Sokolov, M. H. Rafailovich, H. Lorenz, J. P. Kotthaus, J. Wang, S. K. Sinha, and A. Gibaud, "Polymer thin films on patterned Si surfaces," *Macromolecules*, vol. 31, no. 6, pp. 1915–1920, 1998.

[143] J. A. Torres, P. F. Nealey, and J. J. de Pablo, "Molecular simulation of ultrathin polymeric films near the glass transition," *Phys. Rev. Lett.*, vol. 85, no. 15, pp. 3221–3224, 2000.

[144] Y. Pu, H. White, M. H. Rafailovich, J. Sokolov, A. Patel, C. White, W. L. Wu, V. Zaitsev, and S. A. Schwarz, "Probe diffusion in thin PS free-standing films," *Macromolecules*, vol. 34, no. 24, pp. 8518–8522, 2001.

[145] V. A. Harmandaris, K. C. Daoulas, and V. G. Mavrantzas, "Molecular Dynamics Simulation of a Polymer Melt/Solid Interface: Local Dynamics and Chain Mobility in a Thin Film of Polyethylene Melt Adsorbed on Graphite," *Macromolecules*, vol. 38, no. 13, pp. 5796–5809, 2005.

[146] J. B. Nicholas, F. R. Trouw, J. E. Mertz, L. E. Iton, and A. J. Hopfinger, "Molecular dynamics simulation of propane and methane in silicalite," *J. Phys. Chem.*, vol. 97, no. 16, pp. 4149–4163, 1993.

[147] K. S. Smirnov, "Computer simulation study of methane in silicalite," *Chem. Phys. Lett.*, vol. 229, no. 3, pp. 250–256, 1994.

[148] K. S. Smirnov and B. van de Graaf, "Study of methane adsorption in MFI and MEL zeolites by combination of the electronegativity equalization method and molecular dynamics," *J. Chem. Soc., Faraday Trans.*, vol. 92, pp. 2475–2480, 1996.

[149] F. Leroy, B. Rousseau, and A. H. Fuchs, “Self-diffusion of n-alkanes in silicalite using molecular dynamics simulation: A comparison between rigid and flexible frameworks,” *Phys. Chem. Chem. Phys.*, vol. 6, pp. 775–783, 2004.

[150] J. Kuhn, J. M. Castillo-Sanchez, J. Gascon, S. Calero, D. Dubbeldam, T. J. H. Vlugt, F. Kapteijn, and J. Gross, “Adsorption and Diffusion of Water, Methanol, and Ethanol in All-Silica DD3R: Experiments and Simulation,” *J. Phys. Chem. C*, vol. 113, no. 32, pp. 14 290–14 301, 2009.

[151] I. Inzoli, J.-M. Simon, and S. Kjelstrup, “Surface Adsorption Isotherms and Surface Excess Densities of n-Butane in Silicalite-1,” *Langmuir*, vol. 25, no. 3, pp. 1518–1525, 2009.

[152] E. Beerdsen, B. Smit, and S. Calero, “The Influence of Non-framework Sodium Cations on the Adsorption of Alkanes in MFI- and MOR-Type Zeolites,” *J. Phys. Chem. B*, vol. 106, no. 41, pp. 10 659–10 667, 2002.

[153] M. G. Ahunbay, “Monte Carlo Simulation of Water Adsorption in Hydrophobic MFI Zeolites with Hydrophilic Sites,” *Langmuir*, vol. 27, no. 8, pp. 4986–4993, 2011.

[154] Y. He and N. A. Seaton, “Experimental and Computer Simulation Studies of the Adsorption of Ethane, Carbon Dioxide, and Their Binary Mixtures in MCM-41,” *Langmuir*, vol. 19, no. 24, pp. 10 132–10 138, 2003.

[155] E. Jaramillo and M. Chandross, “Adsorption of Small Molecules in LTA Zeolites. 1. NH3, CO2, and H2O in Zeolite 4A,” *J. Phys. Chem. B*, vol. 108, no. 52, pp. 20 155–20 159, 2004.

[156] D. Dubbeldam, S. Calero, T. J. H. Vlugt, R. Krishna, T. L. M. Maesen, and B. Smit, “United Atom Force Field for Alkanes in Nanoporous Materials,” *J. Phys. Chem. B*, vol. 108, no. 33, pp. 12 301–12 313, 2004.

[157] P. Boulet, L. Narasimhan, D. Berg'e-Lefranc, B. Kuchta, O. Schäf, and R. Denoyel, "Adsorption into the MFI zeolite of aromatic molecule of biological relevance. Investigations by Monte Carlo simulations," *J. Mol. Modeling*, vol. 15, no. 6, pp. 573–579, 2009.

[158] C. E. Ramachandran, S. Chempath, L. J. Broadbelt, and R. Q. Snurr, "Water adsorption in hydrophobic nanopores: Monte Carlo simulations of water in silicalite," *Microporous Mesoporous Mater.*, vol. 90, no. 1-3, pp. 293–298, 2006.

[159] P. Bai, M. Tsapatsis, and J. I. Siepmann, "Multicomponent Adsorption of Alcohols onto Silicalite-1 from Aqueous Solution: Isotherms, Structural Analysis, and Assessment of Ideal Adsorbed Solution Theory," *Langmuir*, vol. 28, no. 44, pp. 15 566–15 576, 2012.

[160] B. Slater, J. Titiloye, F. Higgins, and S. Parker, "Atomistic simulation of zeolite surfaces," *Curr. Opin. Solid State Mater. Sci.*, vol. 5, no. 5, pp. 417–424, 2001.

[161] B. Slater, C. R. A. Catlow, Z. Liu, T. Ohsuna, O. Terasaki, and M. A. Camblor, "Surface Structure and Crystal Growth of Zeolite Beta C," *Angew. Chem. Int. Ed.*, vol. 41, no. 7, pp. 1235–1237, 2002.

[162] D. M. Abril, B. Slater, and C. Blanco, "Modeling dynamics of the external surface of zeolite LTA," *Microporous Mesoporous Mater.*, vol. 123, no. 1-3, pp. 268–273, 2009.

[163] W. Greń, S. C. Parker, B. Slater, and D. W. Lewis, "Structure of Zeolite A (LTA) Surfaces and the Zeolite A/Water Interface," *J. Phys. Chem. C*, vol. 114, no. 21, pp. 9739–9747, 2010.

[164] A. F. Combariza and G. Sastre, “Influence of Zeolite Surface in the Sorption of Methane from Molecular Dynamics,” *J. Phys. Chem. C*, vol. 115, no. 28, pp. 13 751–13 758, 2011.

[165] J. Zhu, H. Jin, L. Zang, Y. Li, Y. Zhang, K. Ding, X. Huang, L. Ning, and W. Chen, “Deposition of Nonstoichiometric Tritungsten Oxides on the TiO2(110) Surface: A Possible Way to Stabilize the Unstable Clusters in the Gas Phase,” *J. Phys. Chem. C*, vol. 115, no. 31, pp. 15 335–15 344, 2011.

[166] N. E. R. Zimmermann, S. Jakobtorweihen, E. Beerdsen, B. Smit, and F. J. Keil, “In-Depth Study of the Influence of Host-Framework Flexibility on the Diffusion of Small Gas Molecules in One-Dimensional Zeolitic Pore Systems,” *J. Phys. Chem. C*, vol. 111, no. 46, pp. 17 370–17 381, 2007.

[167] García-Pérez, J. B. Parra, C. O. Ania, D. Dubbeldam, T. J. H. Vlugt, J. M. Castillo, P. J. Merkling, and S. Calero, “Unraveling the Argon Adsorption Processes in MFI-Type Zeolite,” *J. Phys. Chem. C*, vol. 112, no. 27, pp. 9976–9979, 2008.

[168] Z. E. Hughes, L. A. Carrington, P. Raiteri, and J. D. Gale, “A Computational Investigation into the Suitability of Purely Siliceous Zeolites as Reverse Osmosis Membranes,” *J. Phys. Chem. C*, vol. 115, no. 10, pp. 4063–4075, 2011.

[169] I. Díaz, E. Kokkoli, O. Terasaki, and M. Tsapatsis, “Surface Structure of Zeolite (MFI) Crystals,” *Chem. Mater.*, vol. 16, no. 25, pp. 5226–5232, 2004.

[170] M. Salvalaglio, T. Vetter, F. Giberti, M. Mazzotti, and M. Parrinello, “Uncovering Molecular Details of Urea Crystal Growth in the Presence of Additives,” *J. Am. Chem. Soc.*, vol. 134, no. 41, pp. 17 221–17 233, 2012.

[171] A. Barducci, G. Bussi, and M. Parrinello, “Well-Tempered Metadynamics: A Smoothly Converging and Tunable Free-Energy Method,” *Phys. Rev. Lett.*, vol. 100, p. 020603, 2008.

[172] K. A. Smith, M. Vladkov, and J.-L. Barrat, “Polymer Melt near a Solid Surface: A Molecular Dynamics Study of Chain Conformations and Desorption Dynamics,” *Macromolecules*, vol. 38, no. 2, pp. 571–580, 2005.

[173] D. Frenkel and B. Smit, Understanding Molecular Simulation From Algorithms to Applications, pp. 23–62. California: Academic Press, 2002.

[174] M. L. Mansfield, “Monte Carlo studies of polymer chain dimensions in the melt,” *J. Chem. Phys.*, vol. 77, no. 3, pp. 1554–1559, 1982.

[175] P. V. K. Pant and D. N. Theodorou, “Variable Connectivity Method for the Atomistic Monte Carlo Simulation of Polydisperse Polymer Melts,” *Macromolecules*, vol. 28, no. 21, pp. 7224–7234, 1995.

[176] A. Uhlherr, V. G. Mavrantzas, M. Doxastakis, and D. N. Theodorou, “Directed Bridging Methods for Fast Atomistic Monte Carlo Simulations of Bulk Polymers,” *Macromolecules*, vol. 34, no. 24, pp. 8554–8568, 2001.

[177] M. Doxastakis, V. G. Mavrantzas, and D. N. Theodorou, “Atomistic Monte Carlo simulation of cis-1,4 polyisoprene melts. II. Parallel tempering end-bridging Monte Carlo simulations,” *J. Chem. Phys.*, vol. 115, no. 24, pp. 11 352–11 361, 2001.

[178] R. Faller, F. Müller-Plathe, M. Doxastakis, and D. Theodorou, “Local Structure and Dynamics of trans-Polyisoprene Oligomers,” *Macromolecules*, vol. 34, no. 5, pp. 1436–1448, 2001.

[179] C. D. Wick and D. N. Theodorou, “Connectivity-Altering Monte Carlo Simulations of the End Group Effects on Volumetric Properties for Poly(ethylene oxide),” *Macromolecules*, vol. 37, no. 18, pp. 7026–7033, 2004.

[180] L. D. Peristeras, I. G. Economou, and D. N. Theodorou, “Structure and Volumetric Properties of Linear and Triarm Star Polyethylenes from Atomistic Monte Carlo Simulation Using New Internal Rearrangement Moves,” *Macromolecules*, vol. 38, no. 2, pp. 386–397, 2005.

[181] C. Baig, O. Alexiadis, and V. G. Mavrantzas, “Advanced Monte Carlo Algorithm for the Atomistic Simulation of Short- and Long-Chain Branched Polymers: Implementation for Model H-Shaped, A3AA3 Multiarm (Pom-Pom), and Short-Chain Branched Polyethylene Melts,” *Macromolecules*, vol. 43, no. 2, pp. 986–1002, 2010.

[182] K. C. Daoulas, A. F. Terzis, and V. G. Mavrantzas, “Variable Connectivity Methods for the Atomistic Monte Carlo Simulation of Inhomogeneous and/or Anisotropic Polymer Systems of Precisely Defined Chain Length Distribution: Tuning the Spectrum of Chain Relative Chemical Potentials,” *Macromolecules*, vol. 36, no. 17, pp. 6674–6682, 2003.

[183] J. Owicki and H. Scheraga, “Preferential sampling near solutes in monte carlo calculations on dilute solutions,” *Chem. Phys. Lett.*, vol. 47, no. 3, pp. 600–602, 1977.

[184] L. Janosi and M. Doxastakis, “Accelerating flat-histogram methods for potential of mean force calculations,” *J. Chem. Phys.*, vol. 131, no. 5, p. 054105, 2009.

[185] L. Janosi, A. Prakash, and M. Doxastakis, “Lipid-Modulated Sequence-Specific Association of Glycophorin A in Membranes,” *Biophys. J.*, vol. 99, no. 1, pp. 284–292, 2010.

[186] M. Garvey, T. Tadros, and B. Vincent, “A comparison of the volume occupied by macromolecules in the adsorbed state and in bulk solution: Adsorption of narrow molecular weight fractions of poly(vinyl alcohol) at the polystyrene/water interface,” *J. Colloid Interface Sci.*, vol. 49, no. 1, pp. 57–68, 1974.

[187] M. Garvey, T. Tadros, and B. Vincent, “A comparison of the adsorbed layer thickness obtained by several techniques of various molecular weight fractions of poly(vinyl alcohol) on aqueous polystyrene latex particles,” *J. Colloid Interface Sci.*, vol. 55, no. 2, pp. 440–453, 1976.

[188] J. A. Baker, R. A. Pearson, and J. C. Berg, “Influence of particle curvature on polymer adsorption layer thickness,” *Langmuir*, vol. 5, no. 2, pp. 339–342, 1989.

[189] R. Greenwood, P. Luckham, and T. Gregory, “The effect of particle size on the layer thickness of a stabilising polymer adsorbed onto two different classes of polymer latex, as determined from rheological experiments,” *Colloids Surf., A*, vol. 98, no. 1-2, pp. 117–125, 1995.

[190] K. C. Daoulas, D. N. Theodorou, V. A. Harmandaris, N. C. Karayiannis, and V. G. Mavrantzas, “Self-Consistent-Field Study of Compressible Semiflexible Melts Adsorbed on a Solid Substrate and Comparison with Atomistic Simulations,” *Macromolecules*, vol. 38, no. 16, pp. 7134–7149, 2005.

[191] V. Ganesan, L. Khounlavong, and V. Pryamitsyn, “Equilibrium characteristics of semiflexible polymer solutions near probe particles,” *Phys. Rev. E*, vol. 78, p. 051804, 2008.

[192] P. Linse and N. Källrot, “Polymer Adsorption from Bulk Solution onto Planar Surfaces: Effect of Polymer Flexibility and Surface Attraction in Good Solvent,” *Macromolecules*, vol. 43, no. 4, pp. 2054–2068, 2010.

[193] M. G. Martin and J. I. Siepmann, “Transferable Potentials for Phase Equilibria. 1. United-Atom Description of n-Alkanes,” *J. Phys. Chem. B*, vol. 102, no. 14, pp. 2569–2577, 1998.

[194] S. K. Nath, F. A. Escobedo, and J. J. de Pablo, “On the simulation of vapor–liquid equilibria for alkanes,” *J. Chem. Phys.*, vol. 108, no. 23, pp. 9905–9911, 1998.

[195] N. C. Karayiannis, A. E. Giannousaki, V. G. Mavrantzas, and D. N. Theodorou, “Atomistic Monte Carlo simulation of strictly monodisperse long polyethylene melts through a generalized chain bridging algorithm,” *J. Chem. Phys.*, vol. 117, no. 11, pp. 5465–5479, 2002.

[196] Y. Muraoka, K. Kamide, and H. Suzuki, “Direct determinations of the unperturbed dimensions of linear polyethylene molecules,” *Brit. Polym. J.*, vol. 15, no. 2, pp. 107–109, 1983.

[197] N. E. Moe and M. D. Ediger, “Calculation of the coherent dynamic structure factor of polyisoprene from molecular dynamics simulations,” *Phys. Rev. E*, vol. 59, pp. 623–630, 1999.

[198] M. Destrée, A. Lyulin, and J.-P. Ryckaert, “Monte Carlo Prediction of the Structure Factor of Polyethylene in Good and θ-Solvents,” *Macromolecules*, vol. 29, no. 5, pp. 1721–1727, 1996.

[199] L. A. Girifalco, “Interaction potential for carbon (C_{60}) molecules,” *J. Phys. Chem.*, vol. 95, no. 14, pp. 5370–5371, 1991.

[200] Y. J. Guo, N. Karasawa, and W. A. Goddard, “Prediction of Fullerene Packing in C_{60} and C_{70} Crystals,” *Nature*, vol. 351, no. 6326, pp. 464–467, 1991.

[201] J. H. Walther, R. Jaffe, T. Halicioglu, and P. Koumoutsakos, “Carbon Nanotubes in Water: Structural Characteristics and Energetics,” *J. Phys. Chem. B*, vol. 105, no. 41, pp. 9980–9987, 2001.

[202] K. Vollmayr, W. Kob, and K. Binder, “Cooling-rate effects in amorphous silica: A computer-simulation study,” *Phys. Rev. B*, vol. 54, pp. 15 808–15 827, 1996.

[203] A. Bródka and T. W. Zerda, “Properties of liquid acetone in silica pores: Molecular dynamics simulation,” *J. Chem. Phys.*, vol. 104, no. 16, pp. 6319–6326, 1996.

[204] B. Hess, C. Kutzner, D. van der Spoel, and E. Lindahl, “GROMACS 4: Algorithms for Highly Efficient, Load-Balanced, and Scalable Molecular Simulation,” *J. Chem. Theory Comput.*, vol. 4, no. 3, pp. 435–447, 2008.

[205] F. Eisenhaber, P. Lijnzaad, P. Argos, C. Sander, and M. Scharf, “The double cubic lattice method: Efficient approaches to numerical integration of surface area and volume and to dot surface contouring of molecular assemblies,” *J. Comput. Chem.*, vol. 16, no. 3, pp. 273–284, 1995.

[206] M. P. Allen and D. J. Tildesley, Computer simulation of liquids, pp. 220–223. Oxford University Press, New York, 1987.

[207] C. D. Wick and J. I. Siepmann, “Self-Adapting Fixed-End-Point Configurational-Bias Monte Carlo Method for the Regrowth of Interior

Segments of Chain Molecules with Strong Intramolecular Interactions," *Macromolecules*, vol. 33, no. 19, pp. 7207–7218, 2000.

[208] V. A. Harmandaris, M. Doxastakis, V. G. Mavrantzas, and D. N. Theodorou, "Detailed molecular dynamics simulation of the self-diffusion of n-alkane and cis-1,4 polyisoprene oligomer melts," *J. Chem. Phys.*, vol. 116, no. 1, pp. 436–446, 2002.

[209] C. Chen, P. Depa, J. K. Maranas, and V. G. Sakai, "Comparison of explicit atom, united atom, and coarse-grained simulations of poly(methyl methacrylate)," *J. Chem. Phys.*, vol. 128, no. 12, p. 124906, 2008.

[210] D. Fritz, V. A. Harmandaris, K. Kremer, and N. F. A. van der Vegt, "Coarse-Grained Polymer Melts Based on Isolated Atomistic Chains: Simulation of Polystyrene of Different Tacticities," *Macromolecules*, vol. 42, no. 19, pp. 7579–7588, 2009.

[211] C.-L. Huang, Y.-C. Chen, T.-J. Hsiao, J.-C. Tsai, and C. Wang, "Effect of Tacticity on Viscoelastic Properties of Polystyrene," *Macromolecules*, vol. 44, no. 15, pp. 6155–6161, 2011.

[212] G. S. Grest and K. Kremer, "Molecular dynamics simulation for polymers in the presence of a heat bath," *Phys. Rev. A*, vol. 33, pp. 3628–3631, 1986.

[213] K. Kremer, G. S. Grest, and I. Carmesin, "Crossover from Rouse to Reptation Dynamics: A Molecular-Dynamics Simulation," *Phys. Rev. Lett.*, vol. 61, pp. 566–569, 1988.

[214] C. Chen, P. Depa, V. G. Sakai, J. K. Maranas, J. W. Lynn, I. Peral, and J. R. D. Copley, "A comparison of united atom, explicit atom, and coarse-grained simulation models for poly(ethylene oxide)," *J. Chem. Phys.*, vol. 124, no. 23, p. 234901, 2006.

[215] V. A. Harmandaris, D. Reith, N. F. A. van der Vegt, and K. Kremer, “Comparison Between Coarse-Graining Models for Polymer Systems: Two Mapping Schemes for Polystyrene,” *Macromol. Chem. Phys.*, vol. 208, no. 19-20, pp. 2109–2120, 2007.

[216] J. T. Padding and W. J. Briels, “Systematic coarse-graining of the dynamics of entangled polymer melts: the road from chemistry to rheology,” *J. Phys.: Condens. Matter*, vol. 23, no. 23, p. 233101, 2011.

[217] T. Spyriouni, C. Tzoumanekas, D. Theodorou, F. Müller-Plathe, and G. Milano, “Coarse-Grained and Reverse-Mapped United-Atom Simulations of Long-Chain Atactic Polystyrene Melts: Structure, Thermodynamic Properties, Chain Conformation, and Entanglements,” *Macromolecules*, vol. 40, no. 10, pp. 3876–3885, 2007.

[218] H. A. Karimi-Varzaneh, H.-J. Qian, X. Chen, P. Carbone, and F. Müller-Plathe, “IBIsCO: A molecular dynamics simulation package for coarse-grained simulation,” *J. Comput. Chem.*, vol. 32, no. 7, pp. 1475–1487, 2011.

[219] S. Izvekov, A. Violi, and G. A. Voth, “Systematic Coarse-Graining of Nanoparticle Interactions in Molecular Dynamics Simulation,” *J. Phys. Chem. B*, vol. 109, no. 36, pp. 17 019–17 024, 2005.

[220] S. Izvekov and A. Violi, “A Coarse-Grained Molecular Dynamics Study of Carbon Nanoparticle Aggregation,” *J. Chem. Theory Comput.*, vol. 2, no. 3, pp. 504–512, 2006.

[221] C. K. Lee and C. C. Hua, “Nanoparticle interaction potentials constructed by multiscale computation,” *J. Chem. Phys.*, vol. 132, no. 22, p. 224904, 2010.

[222] Q. Sun and R. Faller, “Systematic Coarse-Graining of a Polymer Blend: Polyisoprene and Polystyrene,” *J. Chem. Theory Comput.*, vol. 2, no. 3, pp. 607–615, 2006.

[223] G. Bussi, D. Donadio, and M. Parrinello, “Canonical sampling through velocity rescaling,” *J. Chem. Phys.*, vol. 126, no. 1, p. 014101, 2007.

[224] H. J. C. Berendsen, J. P. M. Postma, W. F. van Gunsteren, A. DiNola, and J. R. Haak, “Molecular dynamics with coupling to an external bath,” *J. Chem. Phys.*, vol. 81, no. 8, pp. 3684–3690, 1984.

[225] Y. Li, S. Tang, B. C. Abberton, M. Kröger, C. Burkhart, B. Jiang, G. J. Papakonstantopoulos, M. Poldneff, and W. K. Liu, “A predictive multiscale computational framework for viscoelastic properties of linear polymers,” *Polymer*, vol. 53, no. 25, pp. 5935–5952, 2012.

[226] H. Wang, C. Junghans, and K. Kremer, “Comparative atomistic and coarse-grained study of water: What do we lose by coarse-graining?” *Eur. Phys. J. E*, vol. 28, no. 2, pp. 221–229, 2009.

[227] S. O. Nielsen, G. Srinivas, and M. L. Klein, “Incorporating a hydrophobic solid into a coarse grain liquid framework: Graphite in an aqueous amphiphilic environment,” *J. Chem. Phys.*, vol. 123, no. 12, p. 124907, 2005.

[228] “The International Technology Roadmap for Semiconductors,” Tech. Rep., 2011.

[229] H. Ito, “Chemical Amplification Resists for Microlithography,” in Microlithography - Molecular Imprinting, ser. Advances in Polymer Science, vol. 172, pp. 37–245. Springer Berlin Heidelberg, 2005.

[230] H. Ito, “Rise of chemical amplification resists from laboratory curiosity to paradigm enabling Moore’s law,” *Proc. SPIE*, pp. 692 302–692 302–15, 2008.

[231] D. P. Sanders, “Advances in Patterning Materials for 193 nm Immersion Lithography,” *Chem. Rev.*, vol. 110, no. 1, pp. 321–360, 2010.

[232] R. L. Brainard, P. Trefonas, J. H. Lammers, C. A. Cutler, J. F. Mackevich, A. Trefonas, and S. A. Robertson, “Shot noise, LER, and quantum efficiency of EUV photoresists,” *Proc. SPIE*, pp. 74–85, 2004.

[233] M. Glodde, D. L. Goldfarb, D. R. Medeiros, G. M. Wallraff, and G. P. Denbeaux, “Measurements of acid generation by extreme ultraviolet irradiation in lithographic films,” *J. Vac. Sci. Technol. B*, vol. 25, no. 6, pp. 2496–2503, 2007.

[234] G. M. Gallatin, “Resist blur and line edge roughness (Invited Paper),” *Proc. SPIE*, pp. 38–52, 2005.

[235] T. Kozawa and S. Tagawa, “Radiation Chemistry in Chemically Amplified Resists,” *Jpn. J. Appl. Phys.*, vol. 49, no. 3, p. 030001, 2010.

[236] S. H. Kang, V. M. Prabhu, B. D. Vogt, E. K. Lin, W. li Wu, and K. Turnquest, “Effect of copolymer composition on acid-catalyzed deprotection reaction kinetics in model photoresists,” *Polymer*, vol. 47, no. 18, pp. 6293–6302, 2006.

[237] J. S. Petersen, C. A. Mack, J. L. Sturtevant, J. D. Byers, and D. A. Miller, “Nonconstant diffusion coefficients: short description of modeling and comparison to experimental results,” *Proc. SPIE*, pp. 167–180, 1995.

[238] P. J. Rodriguez-Canto, U. Nickel, and R. Abargues, “Understanding Acid Reaction and Diffusion in Chemically Amplified Photoresists: An Approach at

the Molecular Level," *J. Phys. Chem. C*, vol. 115, no. 42, pp. 20 367–20 374, 2011.

[239] G. Schmid, M. Stewart, S. Burns, and C. Willson, "Mesoscale Monte Carlo simulation of photoresist processing," *J. Electrochem. Soc.*, vol. 151, no. 2, pp. G155–G161, 2004.

[240] I. M. Sokolov, "Models of anomalous diffusion in crowded environments," *Soft Matter*, vol. 8, pp. 9043–9052, 2012.

[241] S. B. Yuste, L. Acedo, and K. Lindenberg, "Reaction front in an A + B $\rightarrow$ C reaction-subdiffusion process," *Phys. Rev. E*, vol. 69, p. 036126, Mar 2004.

[242] D. T. Gillespie, "A general method for numerically simulating the stochastic time evolution of coupled chemical reactions," *J. Comput. Phys.*, vol. 22, no. 4, pp. 403–434, 1976.

[243] D. T. Gillespie, "Exact stochastic simulation of coupled chemical reactions," *J. Phys. Chem.*, vol. 81, no. 25, pp. 2340–2361, 1977.

[244] J. Nagle, "Long tail kinetics in biophysics?" *Biophys. J.*, vol. 63, no. 2, pp. 366–370, 1992.

[245] H. Scher and E. W. Montroll, "Anomalous transit-time dispersion in amorphous solids," *Phys. Rev. B*, vol. 12, pp. 2455–2477, 1975.

[246] H. Scher, M. F. Shlesinger, and J. T. Bendler, "Time-Scale Invariance in Transport and Relaxation," *Phys. Today*, vol. 44, no. 1, pp. 26–34, 1991.

[247] J. Klafter, G. Zumofen, and A. Blumen, "Non-Brownian transport in complex systems," *Chem. Phys.*, vol. 177, no. 3, pp. 821–829, 1993.

[248] B. Wang, J. Kuo, S. C. Bae, and S. Granick, "When Brownian diffusion is not Gaussian," *Nat. Mater.*, vol. 11, no. 6, pp. 481–485, 2012.

[249] I. Eliazar and J. Klafter, “Anomalous is ubiquitous,” *Ann. Phys.*, vol. 326, no. 9, pp. 2517–2531, 2011.

[250] I. M. Sokolov, J. Klafter, and A. Blumen, “Fractional Kinetics,” *Phys. Today*, vol. 55, no. 11, pp. 48–54, 2002.

[251] B. I. Henry, T. A. M. Langlands, and S. L. Wearne, “Anomalous diffusion with linear reaction dynamics: From continuous time random walks to fractional reaction-diffusion equations,” *Phys. Rev. E*, vol. 74, p. 031116, 2006.

[252] T. A. M. Langlands, B. I. Henry, and S. L. Wearne, “Anomalous subdiffusion with multispecies linear reaction dynamics,” *Phys. Rev. E*, vol. 77, p. 021111, Feb 2008.

[253] C.-Y. Wang and M. D. Ediger, “Anomalous Translational Diffusion: A New Constraint for Models of Molecular Motion Near the Glass Transition Temperature,” *J. Phys. Chem. B*, vol. 104, no. 8, pp. 1724–1728, 2000.

[254] P. Chaudhuri, L. Berthier, and W. Kob, “Universal Nature of Particle Displacements close to Glass and Jamming Transitions,” *Phys. Rev. Lett.*, vol. 99, p. 060604, 2007.

[255] P. Chaudhuri, S. Sastry, and W. Kob, “Tracking Heterogeneous Dynamics During the α Relaxation of a Simple Glass Former,” *Phys. Rev. Lett.*, vol. 101, p. 190601, 2008.

[256] S. F. Swallen, K. Traynor, R. J. McMahon, M. D. Ediger, and T. E. Mates, “Self-Diffusion of Supercooled Tris-naphthylbenzene,” *J. Phys. Chem. B*, vol. 113, no. 14, pp. 4600–4608, 2009.

[257] B. Wang, S. M. Anthony, S. C. Bae, and S. Granick, “Anomalous yet Brownian,” *Proc. Natl. Acad. Sci. USA*, vol. 106, no. 36, pp. 15 160–15 164, 2009.

[258] S. Kirkpatrick, C. D. Gelatt, and M. P. Vecchi, “Optimization by Simulated Annealing,” *Science*, vol. 220, no. 4598, pp. 671–680, 1983.

[259] R. A. Ferguson, C. A. Spence, E. Reichmanis, L. F. Thompson, and A. R. Neureuther, “Investigation of the exposure and bake of a positive acting resist with chemical amplification,” *Proc. SPIE*, pp. 412–424, 1990.

[260] S. Kang, K. Lavery, K.-W. Choi, V. M. Prabhu, W.-L. Wu, E. K. Lin, A. De Silva, N. Felix, and C. Ober, “A comparison of the reaction-diffusion kinetics between model-EUV polymer and molecular-glass photoresists,” *Proc. SPIE*, pp. 692 317–692 317–12, 2008.

[261] G. M. Wallraff, W. D. Hinsberg, F. A. Houle, J. Opitz, D. Hopper, and J. M. Hutchinson, “Kinetics of chemically amplified resists,” *Proc. SPIE*, pp. 182–190, 1995.

[262] B. Jung, M. Chandhok, T. R. Younkin, C. K. Ober, and M. O. Thompson, “Time Dependent Behavior of Chemically Amplified Resist Characterized under Sub-millisecond Post Exposure Bake,” *J. Photopolym. Sci. Technol.*, vol. 24, no. 5, pp. 487–490, 2011.

[263] B. Jung, C. K. Ober, and M. O. Thompson, “Deprotection reaction kinetics in chemically amplified photoresists determined by sub-millisecond post exposure bake,” *Proc. SPIE*, vol. 8325, 2012.

[264] B. Jung, J. Sha, F. Paredes, M. Chandhok, T. R. Younkin, U. Wiesner, C. K. Ober, and M. O. Thompson, “Kinetic Rates of Thermal Transformations and Diffusion in Polymer Systems Measured during Sub-millisecond Laser-Induced Heating,” *ACS Nano*, vol. 6, no. 7, pp. 5830–5836, 2012.

[265] W. D. Hinsberg, F. A. Houle, G. M. Poliskie, D. Pearson, M. I. Sanchez, and H. Ito, “Product Volatilization as a Probe of the Physics and Chemistry of

Latent Image Formation in Chemically Amplified Resists," *J. Phys. Chem. A*, vol. 106, no. 42, pp. 9776–9787, 2002.

[266] M. T. Cicerone, P. A. Wagner, and M. D. Ediger, "Translational Diffusion on Heterogeneous Lattices: A Model for Dynamics in Glass Forming Materials," *J. Phys. Chem. B*, vol. 101, no. 43, pp. 8727–8734, 1997.

[267] J. S. Langer and S. Mukhopadhyay, "Anomalous diffusion and stretched exponentials in heterogeneous glass-forming liquids: Low-temperature behavior," *Phys. Rev. E*, vol. 77, p. 061505, Jun 2008.

[268] E. J. Saltzman and K. S. Schweizer, "Large-amplitude jumps and non-Gaussian dynamics in highly concentrated hard sphere fluids," *Phys. Rev. E*, vol. 77, p. 051504, 2008.

[269] R. Metzler and J. Klafter, "The random walk's guide to anomalous diffusion: a fractional dynamics approach," *Phys. Rep.*, vol. 339, no. 1, pp. 1–77, 2000.

[270] A. Lubelski, I. M. Sokolov, and J. Klafter, "Nonergodicity Mimics Inhomogeneity in Single Particle Tracking," *Phys. Rev. Lett.*, vol. 100, p. 250602, Jun 2008.

[271] B. I. Henry, P. Straka, and T. A. M. Langlands, An Introduction to Fractional Diffusion, ch. 2, pp. 37–89. World Scientific Publishing Company, 2010.

[272] C. J. Ellison, R. L. Ruszkowski, N. J. Fredin, and J. M. Torkelson, "Dramatic Reduction of the Effect of Nanoconfinement on the Glass Transition of Polymer Films via Addition of Small-Molecule Diluent," *Phys. Rev. Lett.*, vol. 92, p. 095702, Mar 2004.

[273] W. D. Hinsberg, F. A. Houle, M. I. Sanchez, M. E. Morrison, G. M. Wallraff, C. E. Larson, J. A. Hoffnagle, P. J. Brock, and G. Breyta, "Effect of resist

components on image spreading during postexposure bake of chemically amplified resists," *Proc. SPIE*, pp. 148–160, 2000.

[274] J. Garcia-Martinez, K. Li, and G. Krishnaiah, "A mesostructured Y zeolite as a superior FCC catalyst - from lab to refinery," *Chem. Commun.*, vol. 48, pp. 11 841–11 843, 2012.

[275] H. van Koningsveld, H. van Bekkum, and J. C. Jansen, "On the location and disorder of the tetrapropylammonium (TPA) ion in zeolite ZSM-5 with improved framework accuracy," *Acta Crystallogr., Sect. B*, vol. 43, no. 2, pp. 127–132, 1987.

[276] R. M. C. Dawson, D. C. Elliott, W. H. Elliott, and K. M. Jonesw, Data for Biochemical Research, p. 337, vol. 485. Clarendon Press Oxford, 1969.

[277] J. B. Nicholas, A. J. Hopfinger, F. R. Trouw, and L. E. Iton, "Molecular modeling of zeolite structure. 2. Structure and dynamics of silica sodalite and silicate force field," *J. Am. Chem. Soc.*, vol. 113, no. 13, pp. 4792–4800, 1991.

[278] C. Oostenbrink, A. Villa, A. E. Mark, and W. F. Van Gunsteren, "A biomolecular force field based on the free enthalpy of hydration and solvation: The GROMOS force-field parameter sets 53A5 and 53A6," *J. Comput. Chem.*, vol. 25, no. 13, pp. 1656–1676, 2004.

[279] H. J. C. Berendsen, J. P. M. Postma, W. F. van Gunsteren, and J. Hermans, "Interaction models for water in relation to protein hydration," in Intermolecular Forces, pp. 331–342, 1981.

[280] N. R. Tummala, L. Shi, and A. Striolo, "Molecular dynamics simulations of surfactants at the silica-water interface: Anionic vs nonionic headgroups," *J. Colloid Interface Sci.*, vol. 362, no. 1, pp. 135–143, 2011.

[281] T. Darden, D. York, and L. Pedersen, “Particle mesh Ewald: An N [center-dot] log(N) method for Ewald sums in large systems,” *J. Chem. Phys.*, vol. 98, no. 12, pp. 10 089–10 092, 1993.

[282] I.-C. Yeh and M. L. Berkowitz, “Ewald summation for systems with slab geometry,” *J. Chem. Phys.*, vol. 111, no. 7, pp. 3155–3162, 1999.

[283] B. Hess, H. Bekker, H. J. C. Berendsen, and J. G. E. M. Fraaije, “LINCS: A linear constraint solver for molecular simulations,” *J. Comput. Chem.*, vol. 18, no. 12, pp. 1463–1472, 1997.

[284] A. Laio and M. Parrinello, “Escaping free-energy minima,” *Proc. Natl. Acad. Sci. U. S. A.*, vol. 99, no. 20, pp. 12 562–12 566, 2002.

[285] M. Bonomi, A. Barducci, and M. Parrinello, “Reconstructing the equilibrium Boltzmann distribution from well-tempered metadynamics,” *J. Comput. Chem.*, vol. 30, no. 11, pp. 1615–1621, 2009.

[286] M. Bonomi, D. Branduardi, G. Bussi, C. Camilloni, D. Provasi, P. Raiteri, D. Donadio, F. Marinelli, F. Pietrucci, R. A. Broglia, and M. Parrinello, “PLUMED: A portable plugin for free-energy calculations with molecular dynamics,” *Comput. Phys. Commun.*, vol. 180, no. 10, pp. 1961–1972, 2009.

[287] A. V. Dobrynin, A. Deshkovski, and M. Rubinstein, “Adsorption of Polyelectrolytes at an Oppositely Charged Surface,” *Phys. Rev. Lett.*, vol. 84, pp. 3101–3104, 2000.

[288] C. F. Narambuena, D. M. Beltramo, and E. P. M. Leiva, “Polyelectrolyte Adsorption on a Charged Surface. A Study by Monte Carlo Simulations,” *Macromolecules*, vol. 40, no. 20, pp. 7336–7342, 2007.

[289] R. A. Vaia and J. F. Maguire, “Polymer Nanocomposites with Prescribed Morphology: Going beyond Nanoparticle-Filled Polymers,” *Chem. Mater.*, vol. 19, no. 11, pp. 2736–2751, 2007.

[290] S. Ban, K. Malek, C. Huang, and Z. Liu, “A molecular model for carbon black primary particles with internal nanoporosity,” *Carbon*, vol. 49, no. 10, pp. 3362–3370, 2011.

[291] H. A. Karimi-Varzaneh, P. Carbone, and F. Müller-Plathe, “Fast dynamics in coarse-grained polymer models: The effect of the hydrogen bonds,” *J. Chem. Phys.*, vol. 129, no. 15, p. 154904, 2008.

[292] G. Santangelo, A. Di Matteo, F. Müller-Plathe, and G. Milano, “From Mesoscale Back to Atomistic Models: A Fast Reverse-Mapping Procedure for Vinyl Polymer Chains,” *J. Phys. Chem. B*, vol. 111, no. 11, pp. 2765–2773, 2007.

[293] P. Carbone, H. A. K. Varzaneh, X. Chen, and F. Müller-Plathe, “Transferability of coarse-grained force fields: The polymer case,” *J. Chem. Phys.*, vol. 128, no. 6, p. 064904, 2008.

[294] R. Chakrabarti and K. S. Schweizer, “Polymer-mediated spatial organization of nanoparticles in dense melts: Transferability and an effective one-component approach,” *J. Chem. Phys.*, vol. 133, no. 14, p. 144905, 2010.

[295] D. Maillard, S. K. Kumar, B. Fragneaud, J. W. Kysar, A. Rungta, B. C. Benicewicz, H. Deng, L. C. Brinson, and J. F. Douglas, “Mechanical Properties of Thin Glassy Polymer Films Filled with Spherical Polymer-Grafted Nanoparticles,” *Nano Lett.*, vol. 12, no. 8, pp. 3909–3914, 2012.

Appendix A Interactions for Particles of Arbitrary Curvature

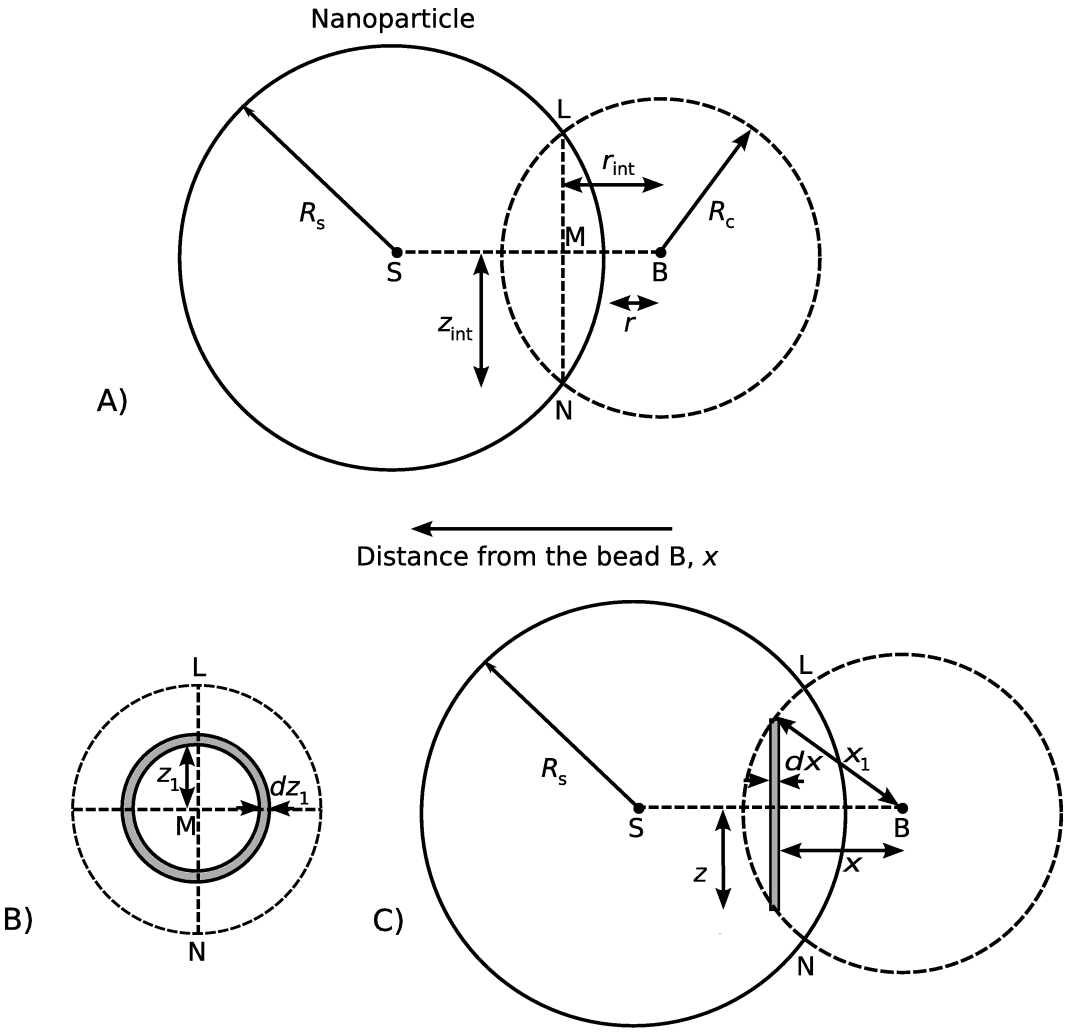

Figure A.1: A) Schematics for calculating effective interaction potential from volume integral. Integration is performed by considering B) dz_1 elements in radial direction, which have a thickness C) dx along the line joining the centers of polymer bead and nanoparticle.

Let, S and B depict the center of the nanoparticle and polymer bead respectively (Figure A.1). Radius of the nanoparticle is R_{s} and nonbonded interactions are truncated at the cut-off distance R_{c}. B is located at a distance r from the particle surface. LN represents the common chord for the 2D projections of the

nanoparticle and cut-off sphere. Let, intersection of the center-to-center line SB and common chord LN be given by M, which is at a distance r_{int} from the polymer bead, whereas SB = $d = R_{\text{s}} + r$. Also, it is assumed that the half length of the common chord MN = z_{int}. From geometry,

$$\text{SM} = \frac{d^2 - {R^2}_{\text{c}} + {R^2}_{\text{s}}}{2d}. \tag{A.1}$$

Substituting $d = R_{\text{s}} + r$ in Eq. A.1,

$$\text{SM} = \frac{2{R^2}_{\text{s}} + 2RR_{\text{s}} - {R^2}_{\text{c}} + r^2}{2(R_{\text{s}} + r)}, \tag{A.2}$$

which leads to,

$$r_{\text{int}} = \frac{2{R^2}_{\text{c}} + r^2 + 2RR_{\text{s}}}{2(R_{\text{s}} + r)}. \tag{A.3}$$

In order to calculate the interaction potential between polymer bead and nanoparticle (U_{NP}), single site potential $u(x)$ should be integrated over the volume of nanoparticle from distance $x = r$ to $x = r_{\text{int}}$, and over the volume of cut-off sphere from the distance $x = r_{\text{int}}$ to $x = R_{\text{c}}$. It should be noted that for the smaller nanoparticles satisfying the condition $r + 2R_{\text{s}} \leq R_{\text{c}}$, integration over the nanoparticle volume will suffice. The integration is performed over an element of thickness dx at a distance x from the polymer bead B (Figure A.1C). Interaction sites are assumed to be distributed uniformly over the nanoparticle volume (number density ρ). The total interaction between the polymer bead and the nanoparticle arise from interaction sites contained within a disc of thickness dx and radius z. Ring elements dz_1 are considered at radial distance z_1 from the center of the disc (Figure A.1B). Each interaction site on this ring element is at a distance $x_1 = \sqrt{x^2 + {z^2}_1}$ from the

polymer bead B, and total interaction potential due to the ring element is given by,

$$u_{\text{ring}}(z_1, x) = 2\pi z_1 \rho u(x_1) dx dz_1, \tag{A.4}$$

which can be integrated to evaluate the effective interaction potential between the polymer bead and the nanoparticle at a distance x as,

$$U_{\text{NP}}(x) = \int_0^z u_{\text{ring}}(z_1, x) dz_1. \tag{A.5}$$